

**Elucidating the Function of Myosin XI in Polarized Cell Growth
and Investigating the Chitin-induced Calcium-mediated Immune
Response in *P. patens***

A Dissertation

Submitted to the Faculty of
WORCESTER POLYTECHNIC INSTITUTE
in Partial Fulfillment of the Requirement for the Degree of
Doctor of Philosophy
in
Biology and Biotechnology
10/02/2020
By

Giulia Galotto

Approved by:

Dr. Luis Vidali
Associate Professor
Dept. Biology &
Biotechnology
Worcester Polytechnic
Institute

Dr. Reeta Rao
Associate Professor
Dept. Biology &
Biotechnology
Worcester Polytechnic
Institute

Dr. Mary Munson
Professor
Dept. Biochemistry and
Molecular
Pharmacology
University of Massachusetts
Medical School

Dr. Amity L. Manning
Assistant Professor
Dept. Biology &
Biotechnology
Worcester Polytechnic
Institute

Dr. Min Wu
Assistant Professor
Dept. Mathematical
Sciences
Worcester Polytechnic
Institute

List of figures	5
Acknowledgments.....	6
Abstract.....	8
Chapter 1 Polarized growth in plants and loss of function via conditional mutagenesis	10
1.1 Introduction	10
1.2 Tip growth in plants	11
1.2.1 <i>Physcomitrella patens</i> and the protenematal tissue	11
1.2.2 Seed plants pollen tubes and root hairs	12
1.2.3 Protonemal cells, pollen tubes and root hairs common morphological features	14
1.3 The vacuole in tip growing cells	15
1.3.1 Regulation of the tip growing cell's vacuole in vascular plants and mosses.....	15
1.4 Ion gradients in tip growing cells.....	16
1.5 Modeling of tip growth	18
1.6 Plants immune response to biotic and abiotic stresses.....	19
1.6.1 The role of Ca ²⁺ in plant's immune response	21
1.7 Regulation of cell polarity via small GTPases	22
1.7.1 Rho of plants and cell polarity.....	23
1.7.2 Rabs and polarized exocytosis.....	24
1.8 The cytoskeleton	26
1.8.1 F-actin architecture in tip growing cells	26
1.8.2 F-actin cytoskeleton in tip growth	27
1.8.3 F-actin binding proteins	29
1.8.4 The microtubules: architecture and role in tip growth.....	30
1.9 Myosin XI, a motor essential for plant growth and development.....	32
1.9.1 Myosin XI in tip growth	34
1.9.2 Regulation of myosin XI by Ca ²⁺ and calmodulin.....	35
2. Loss-of-function techniques to study gene function	36
2.1 TS alleles, from random mutagenesis to residue prediction	39
2.2 The use of temperature-sensitive alleles in plants	40
Chapter 2 Myosin XI drives polarized growth by vesicle clustering and local enrichment of F-actin in <i>Physcomitrium (Physcomitrella) patens</i>	42
2.1 Abstract	42
2.2 Introduction	43

2.3 Results	45
2.3.1 Development of a myosin XI temperature-sensitive allele	45
2.3.2. Myosin XI loss-of-function causes cell death while simultaneous F-actin depletion restores viability	48
2.3.3. In cells with decreased myosin XI activity, but not after F-actin depletion, the vacuole dilates and invades the cell tip	50
2.3.4 Tip growing cells deprived of functional myosin XI exhibit lateral swelling and drastically reduced growth rate	52
2.3.5 Myosin XIa TS cells exposed at 32°C display higher cell tip curvature and diameter than F-actin depleted cells	54
2.3.6 Lack of functional myosin XI dissipates tip-localized VAMP-labeled vesicles and F-actin within minutes	59
2.3.7. Myosin XI is essential for the formation of latrunculin B-induced vesicle clusters	61
2.4 Discussion	63
2.5 Material and Methods	67
2.5.1. Generation of a <i>P. patens</i> myosin XI temperature-sensitive allele and a myosin XIb KO line	67
2.5.2 Plant morphometric assay	71
2.5.3. Time-course fluorescent image acquisition	71
2.5.4. Detection and analysis of cell tip curvature	72
2.5.5. Bright-field time-lapse imaging of cells transferred to high temperature	75
2.5.6. Confocal imaging	75
2.5.7. Vacuolar staining	76
2.5.8. Cell death assay	77
2.5.9. Statistical methods	77
Chapter 3 Chitin Triggers Calcium-mediated Immune Response in the Plant Model	
<i>Physcomitrella patens</i>	78
3.1 Abstract	78
3.2 Introduction	79
3.3 Results	82
3.3.1 Chitin oligosaccharides affect plant growth and morphology in a dose-dependent manner	82
3.3.2 Ca ²⁺ oscillations originate following elicitation with chitin oligosaccharides	84
3.3.3 Chitin oligosaccharides dissipate F-actin at the tip of the cell	90

3.3.4 Chitin oligosaccharides and the calcium-ionophore ionomycin induce expression of defense-related genes.....	92
3.4 Discussion	93
3.5 Material and Methods.....	97
3.5.1. Biological material and growth conditions	97
3.5.2. Morphometric analysis.....	97
3.5.3 Generation of a moss line expressing the Ca ²⁺ sensor GCaMP6f and Lifeact-Ruby2	97
3.5.4 Ca ²⁺ imaging	98
3.5.5 Ca ²⁺ time-series image analysis	99
3.5.6 Ca ²⁺ peak detection analysis	100
3.5.7 Confocal imaging of actin and Ca ²⁺	100
3.5.8 Ca ²⁺ confocal image analysis.....	101
3.5.9 RNA extraction and RT-qPCR	101
Chapter 4 Future directions and conclusions	103
4.1 Further testing of myosin XI as a driver of vesicle clustering for tip accumulations	103
4.2 Myosin XI role in the regulation of cytoplasmic organization, vacuole structure, and cell viability.....	104
4.3 Characterizing the morphology of myosin XI TS cells via modeling and fluorescent markers	105
4.4 Further investigation of <i>P. patens</i> chitin perception	106
4.5 Conclusions	108
Chapter 5 References	109
Chapter 6 Appendix	124
Gene ontology (GO) enrichment analysis of RNASeq data uncover biological processes affected by myosin XI TS allele.....	124
RNA Seq and Gene Ontology methods	125

List of figures

Figure 1.1 Model systems for tip growth in mosses and vascular plants	14
Figure 1.2 Schematic representation of immune response in plants.....	20
Figure 1.3 Comparative architecture of the cytoskeletal elements and ion gradients in the tip growth models.....	27
Figure 2.1 Two point mutations (V584A, L616A) renders myosin XI protein temperature sensitive.....	48
Figure 2.2 Myosin XI TS cells dye after 24 hrs exposure at 32°C, plants, depolymerization of F-actin via Latrunculin B reverts the phenotype.	50
Figure 2.3 Myosin XIa TS cells present an enlarged aberrant vacuole, depolymerization of F-actin via Latrunculin B reverts the phenotype.	51
Figure 2.4 Time lapse of control and myosin XI TS cells at 32°C show growth and morphology defects of myosin deficient cells.....	53
Figure 2.5 Lack of functional myosin or F-actin affects caulonemata tip morphology differently	57
Figure 2.6 Lack of functional myosin or F-actin affects chloronemata tip morphology differently	59
Figure 2.7 F-actin spot and tip oriented vesicle cluster dissipate upon 20 minutes exposure at 30°C	61
Figure 2.8 Latrunculin B induced motile secretory vesicles clusters followed by F-actin cables are myosin XI dependent.	63
Figure 2.9 Illustration of the curvature calculation along the cell periphery.....	73
Figure 2.10 Illustration of the maximum width determination.....	74
Figure 2.11 Determination of optimal bond spacing for curvature calculations.	74
Figure 3.1 Exposure to chitin affects plant size and morphology in a dose-dependent manner...	84
Figure 3.2 Plants at concentrations 0, 1, 0.1, and 10 and 100 μM chitohexaose.	88
Figure 3.3 Chitin oligosaccharides affects cytosolic Ca ²⁺ concentrations.	90
Figure 3.4 Chitin oligosaccharides treatment dissipates the apical F-actin focus and alters Ca ²⁺ oscillations in tip cells.....	92
Figure 3.5 Expression of pathogenesis related genes in response to chitin oligosaccharides and ionomycin treatment	93

Acknowledgments

I would like to start by thanking the whole Biology and Biotechnology department for its contribution to my personal and professional development. I am grateful to the professors I interacted with for Teaching Assistant assignments, journal clubs, and classes, since they had a great impact on my growth. When I joined Worcester Polytechnic Institute for the Ph.D. program I was not very self confident, and the transition from a different country and school system has been hard. All the faculty members of the department have been welcoming, very supportive, and always available to help. Next, I would like to thank the members of the Vidali Lab, especially Robert Orr and Jeff Bibeau, with whom I shared most of my time in the lab. I want to especially thank them for all the laughs we shared, the lunches on the main campus, the hangout Mondays. We had a lot of fun together, they have been an anchor for me and I will cherish the memories of these years together. Other than the fun times, I also want to thank Rob and Jeff for the scientific discussions, assistance during my qualifying exam, and during experiments. During my first year, Jeff was a second mentor for me. Jeff introduced me to various techniques and was an invaluable help with data analysis. I would like to thank my committee members, Prof. Rao, Prof. Wu, Prof. Munson, and Prof. Manning for their precious comments and input on my thesis over the years. A particular thank you goes to Prof. Mary Munson, who is always very supportive and kind; Mary is a special person and treats students (even the ones who are not in her lab) with great care. Mary is always available to help and in multiple occasions she dedicated time from her lab meeting to listen to my research presentations. I would like to acknowledge Prof. Tüzel, who was a part of my committee for a few years and who collaborated with our lab for one of my publications. I would like to thank my friends for being there for me, especially Lorena, Sabine, Elisa, Victoria, Sofia, Anna, Emanuele and Simone, for being part of my life and making it better. A special

acknowledgment goes to my family for their love and their support. A special thank you goes to my parents, who taught me the value of education and enabled it over the years.

Finally, I would like to thank my advisor, Prof. Luis Vidali. Luis has had an immense contribution to my development, both professionally and personally. Luis taught me how to be a scientist and to develop the right mindset to approach complex problems. Luis is very passionate about his research, and has a strong ability to transmit it to his students. He participates actively in the research, with a great contagious enthusiasm. Luis is always present and available for his students. He makes them feel appreciated, spends time with us, and has lunch with us almost every day. In the lab, we don't do research for him, we do it with him. He motivates us by stimulating our curiosity. In fact, we don't do experiments because we need data or the seminar is approaching, but because the potential result is fascinating and "wouldn't it be fun if we did this?". Luis is a great person and mentor because he is sensitive, empathic, and he understands people's character. When I joined the lab, I was scared and I had a long way to go to become an independent thinker, and Luis has been always patient and supportive with me in a very kind way. I know I would not be here writing this if it wasn't for him. Luis cares greatly for his students, and not just that they fulfill the requirements of the program, but also about their well-being in the lab. Luis' attitude towards life and work is positive and constructive and he taught me that if we are not having fun doing our job something needs to change. I will treasure his teachings and his mentoring style, and I will hopefully keep them as my own and pass them along. For all the reasons I mentioned, I feel very fortunate to have spent these five years working alongside him. Worcester Polytechnic Institute and the Vidali Lab will always occupy a very special place in my heart.

Abstract

To protect and exploit existing plant species, it is advantageous to understand the molecular mechanisms behind plant growth and defense response to threats. A subgroup of essential specialized plant cells grows via a highly anisotropic fashion referred to as “tip growth”. The elongated shape of these cells emerges from polarized expansion; this process is mainly driven by myosin XI and the F-actin cytoskeleton mediated vesicle trafficking to the cell tip. Loss of function of myosin XI and F-actin cease tip growth, but the mechanism by which they self-organize to maintain growth has not been characterized. Furthermore, the role of myosin XI in vesicle trafficking in plants has been an underlying assumption in the field, but direct evidence is lacking. Cross correlation studies show myosin XI anticipate the F-actin signal at the cell tip, suggesting myosin XI could be involved in enriching the local F-actin concentration. To shed light on myosin XI involvement in F-actin concentration and vesicle transport, we generated a myosin XI temperature sensitive allele in the moss model system *Physcomitrium (Physcomitrella) patens*. *P. patens* amenability to genetic manipulation, and reduced myosin family size compared to vascular plants facilitate study of protein function. By using this tool, we demonstrated myosin XI clusters secretory vesicles, and drives a mechanism that result in F-actin polymerization. In addition, we proved myosin XI is important in maintaining cell morphology, vacuole homeostasis and cell viability.

Understanding mechanisms behind plant immune response provide a great advantage to increase plant resistance to threats. In vascular plants, various aspects of the immune response against biotic and abiotic stresses have been characterized. These include cytoplasmic Ca^{2+} concentration increase and MAPK phosphorylation cascade that triggers synthesis of defense hormones, activation of defense related genes and lignification of the cell wall. In land plants, only the plant

immune response to an abiotic stress has been object of studies, but mechanisms related to biotic stress response are still lacking. To fill this gap, we studied the response of *P. patens* to a fungal infection simulated by chitin. Since cytoplasmic Ca^{2+} concentration is the first effect observed in vascular plants, we generated a *P. patens* line expressing the Ca^{2+} reporter GCaMP6, to investigate if a similar Ca^{2+} signature is present in land plants. The Ca^{2+} reporter line also expresses Lifeact-Ruby2, to simultaneously visualize F-actin and Ca^{2+} . Our results show, upon chitin treatment, Ca^{2+} oscillation propagates across the plant in a dose-dependent manner. Furthermore, we showed chitin affects growth at the cell and plant level, via affecting the F-actin cytoskeleton at the cell tip, essential for growth. Finally, we show chitin induced Ca^{2+} increase triggers transcription of defense related genes.

Chapter 1 Polarized growth in plants and loss of function via conditional mutagenesis

1.1 Introduction

Plants and the development of agriculture have been essential for the advancement of human civilization (Bhargava and Srivastava, 2019). Current and future climate conditions, such as global warming and increased extreme weather events, pose threats to the fitness of plant species. In addition, biotic stresses, such as fungal, bacterial, and viral infection, are a major constraint to plant survival and production (Boyd et al., 2013). Given that the world population is increasing, and it is predicted to increase to 9 billion by 2050, maintaining and improving food production is essential (Diouf and Sheeran, 2010). To this end, understanding the molecular mechanisms behind plant growth and pathogen resistance would provide a huge advantage to increase the production and fitness of plants. The goal of this thesis is to understand the role of the molecular motor myosin XI in polarized growth in plants and to study the plant defense mechanism to fungal infection. To achieve this goal, we used the moss *Physcomitrium (Physcomitrella) patens*, which is highly amenable at the genetic level and offers advantages to study protein function compared to vascular plants. In the following sections, I introduce the model system and discuss its main features. Since most of the *P. patens* tissue is polarized at the juvenile stage, I focus on aspects of this model related to polarized growth. Furthermore, I review the literature on the immune system of plants, specifically as it pertains to biotic stressors. In our work, to study protein function, we reduced protein levels via the exploitation of a temperature-sensitive allele. Hence, I finally review the main loss of function techniques available to researchers, and I emphasize temperature-sensitive alleles in yeasts and plants.

1.2 Tip growth in plants

A subpopulation of specialized plant cells exhibits an extremely anisotropic growth, called “tip growth.” This is the case for mosses protonemal cells and rhizoids, and seed plants root hairs and pollen tubes (Figure 1.1). With their specialized function, tip growing cells accomplish a crucial role for the plant. Protonemal cells establish the body of the organism and root hairs are essential to anchor the plant to the soil and for water and nutrient absorption (Rounds and Bezanilla, 2013). Pollen tubes are short lived cells (about one day life span) that act as the male gametophyte and are responsible for sexual reproduction of seed plants (Rounds and Bezanilla, 2013). We briefly discuss the characteristics of each of the aforementioned tip growing cells, with a focus on the moss *Physcomitrella patens* and its protonemal tissue, the model organism used in our work.

1.2.1 *Physcomitrella patens* and the protonematal tissue

Physcomitrella patens, now *Physcomitrium patens*, commonly defined as the earth spreading moss, belongs to the division of the Bryophytes. *P. patens* became a model system in the 1960’s, mostly due to its tractable genetics and amenability to culturing (Burgess and Linstead, 1981; Cove et al., 1991). In fact, this plant has a haplodiplontic life cycle, with a dominant haploid phase, and it can be propagated vegetatively via tissue homogenization. In 1997, Schaefer *et al.* reported that gene targeting via homologous recombination was applicable to *P. patens*, a discovery that made this model suitable for gene and protein functional studies (Schaefer and Zryd, 1997; Rensing et al., 2020). In the following decade, several genome manipulation techniques have been developed, facilitating the use of this model for plant cell biology and functional genomic discoveries (Rensing et al., 2020). Examples include a 1-week long RNAi protocol (Bezanilla et al., 2003;

Bezanilla et al., 2005; Vidali et al., 2007), the development of temperature-sensitive alleles (Vidali et al., 2009b), and stable transformations (Cho et al., 1999; Liu and Vidali, 2011a). The genome of *P. patens* became available since 2008 (Rensing et al., 2008), and recently, genome editing via CRISPR/Cas9 has been applied to this model, enabling functional studies of larger gene families (Collonnier et al., 2017). The juvenile stage of *P. patens* is characterized by a protonemal tissue in which every apical cell growth by tip growth, providing an easy to access a collection of tip growing cells. The protonemal tissue is single cell thick, and it is made of two cell types called chloronema and caulonema (Cove, 2005; Vidali and Bezanilla, 2012). Chloronemata cells, the first to originate from the haploid spore, are slow-growing (0.1 $\mu\text{m}/\text{min}$) (Rounds and Bezanilla, 2013), rich in chloroplasts and have walls perpendicular to the main axes of the cell. Caulonemata cells develop from the chloronemata after about one week, in response to light and the hormone auxin (Cove and Knight, 1993). They are faster growing (0.33 $\mu\text{m}/\text{min}$) , and have fewer chloroplasts and oblique cell walls (Cove and Knight, 1993; Cove, 2005; Vidali and Bezanilla, 2012). Due to their slower growth and abundance in chloroplasts, chloronemata are believed to provide metabolic support, while caulonemata, due to their fast growth, mainly contribute to land colonization. At the juvenile stage, cells have a large size, making *P. patens* particularly suitable for microscopy studies. For all these reasons, today, *P. patens* is one of the main models used to study tip growth in plants (Orr et al., 2020a; Rensing et al., 2020).

1.2.2 Seed plants pollen tubes and root hairs

The pollen tube is a type of tip growing cell required for fertilization and essential for species propagation (Johnson et al., 2019). Pollen tubes are the most studied tip growing cells in plants, mainly due to their amenability. In fact, the pollen from some species can be easily cultured and

germinated *in vitro*. Differently than other plant cells, they maintain polarity *in vitro*, and they germinate synchronously and uniformly (Qin and Yang, 2011). Furthermore, they exhibit the fastest known growth rate, 12-18 $\mu\text{m}/\text{min}$ in *L. longiflorum* (Rounds and Bezanilla, 2013), and long size (1 foot long in pollen tube from maize (Barnabas and Fridvalszy, 1984). Research has been mostly focused on pollen tubes from *Arabidopsis thaliana*, *Lilium longiflorum*, *Lilium formosanum* and *Nicotiana tabacum* (Rounds and Bezanilla, 2013).

Another well studied seed plant tip growing cell is the root hair. The evolution of roots was paramount to plants adaptation to terrestrial environments. Root hairs extrude from root epidermal cells (trichoblasts), expanding the overall surface area of the root and increasing resources uptake (Cui et al., 2018). Root hairs are essential to anchor the plant to the substrate and to absorb nutrients from the ground (Jungk, 2001). These cells are not essential for the viability of the plant; hence they provide a good target for loss-of-function mutations (Cui et al., 2018). Furthermore, because of their external location in the root, they can be easily exposed to different culturing conditions (Cárdenas, 2009). Differently than protonemal cells, the growth in

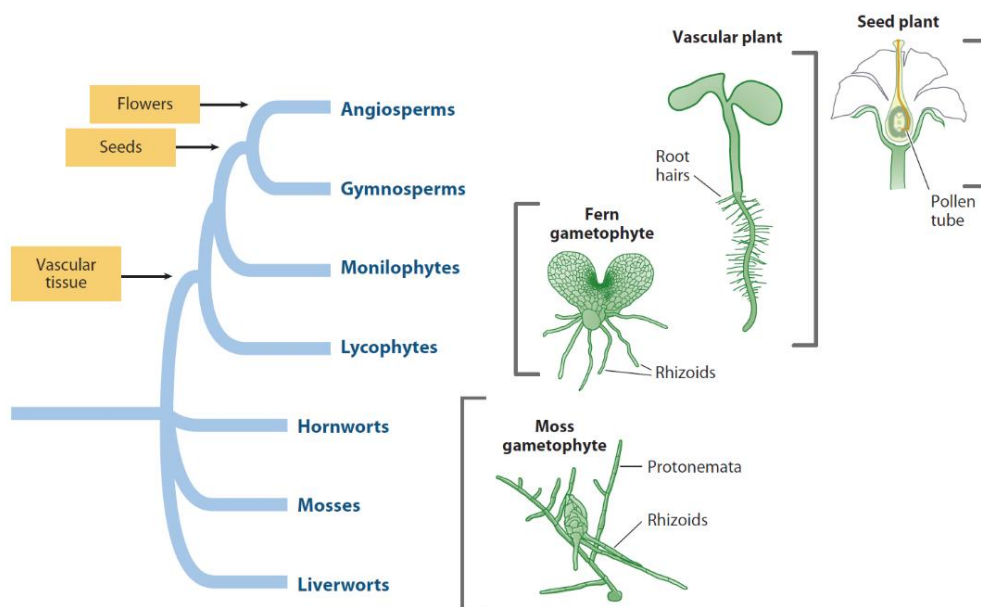


Figure 1.1 Model systems for tip growth in mosses and vascular plants The left side shows a cladogram that depicts relations between different plant species. In yellow are highlighted major plant development that were paramount for their evolution. On the right side are indicated the tip growing structures in mosses, ferns and vascular plants. Modified from (Rounds and Bezanilla, 2013)

pollen tubes and root hair is oscillatory, with growth peaks every 23 seconds for pollen tubes (Pierson et al., 1996; Monshausen et al., 2007; Cárdenas, 2009).

1.2.3 Protonemal cells, pollen tubes and root hairs common morphological features

Differently than isotropically growing cells, tip growing cells display a characteristic cytoplasmatic zonation (Hepler et al., 2001; Furt et al., 2012; Rounds and Bezanilla, 2013). The zonation is the result of the highly anisotropic growth fashion of these cells. Since the apex is deprived of major organelles, it is referred to as “clear zone”. The apex is the region of the cell dedicated to active growth, and it is mainly filled with secretory vesicles rich in cell wall material (Rounds and Bezanilla, 2013), and of endoplasmic reticulum (ER). At the extreme apex, exocytosis of vesicles occurs (about $189 \text{ vesicles s}^{-1}$ in *P. patens* caulonema (Bibeau et al., 2018)), to support growth. However, this is also an area characterized by endocytosis, mainly to recycle excess of membrane deposited at the tip. The area behind the tip is rich in mitochondria, ER, and Golgi bodies, which provide energy, protein synthesis, and vesicle production, respectively. Vacuoles and plastids are located in the medial and rear area of the cell, and mainly contribute to the turgor and osmotic pressure and for storage and lysis (Oda et al., 2009; Furt et al., 2012). Root hairs and pollen tubes, but not protonemata, exhibit a unique feature: a reverse-fountain cytoplasmic streaming. In this cytoplasmic flow, vesicles and small organelles are transported toward the tip in the peripheral area of the cell, and material is recycled towards the rear in the central area of the cell (Hepler et al., 2001; Rounds and Bezanilla, 2013). Cytoplasmic streaming

depends on myosin XI motors transporting organelles, and it results in increase mobilization of molecules and of the ER, Golgi, peroxisome and mitochondria (Verchot-Lubicz and Goldstein, 2010).

1.3 The vacuole in tip growing cells

The vacuole is the largest compartment existing in plant cells, and it serves both physical and metabolic essential functions (Marty, 1999). The acts as a reservoir for ions and metabolites (Marty, 1999). Protonemal cells, pollen tubes, and root hairs have a common vacuolar architecture, characterized by a large vacuole in the rear and a multitude of “finger-like” tubular vacuoles in the medial-subapical region of the cell (Ovecka et al., 2005; Oda et al., 2009; Rounds and Bezanilla, 2013). The tubular vacuoles are very dynamic and continuously rearrange their shape by fusion and separation of individual tubules (Ovecka et al.; Oda et al., 2009). The similar vacuolar organization across tip growing cells is noteworthy, since bryophytes and vascular plants diverged in evolution and share a common ancestor 400 million years ago (Rensing et al., 2008). The parallel evolution of a similar structure of the vacuole suggests it plays a crucial role for the cell's homeostasis.

1.3.1 Regulation of the tip growing cell's vacuole in vascular plants and mosses

Differently than the structure, vacuolar regulation appears to be different between tip growing cells of vascular plants and mosses. In *A. thaliana* root hairs, latrunculin B treatment results in the transition of dynamic tubular vacuoles into a static unique round vacuole, suggesting F-actin is responsible for vacuolar regulation (Ovecka et al., 2005). Similarly, in *Lilium longiflorum* pollen tubes, latrunculin B treatment (even as low as 1 pM), but not oryzalin, affects the morphology and motion of the vacuole (Lovy-Wheeler et al., 2007). Interestingly, actin microfilaments regulate the

vacuole in the non-tip growing BY-2 cells of the vascular plant *Nicotiana tabacum* (Kutsuna et al., 2003; Higaki et al., 2006). Hikagi *et al.* observed that F-actin microfilaments colocalize with the tonoplast, which is highly dynamic (Higaki et al., 2006). Furthermore, when treated with the myosin ATPase inhibitor BDM and the F-actin polymerization inhibitor bistheonellide, the vacuolar membrane appears to be no longer dynamic, proving the actin-myosin system is involved in its vacuolar rearrangements (Kutsuna et al., 2003; Higaki et al., 2006). Differently, in *P. patens* chloronemata cells, Oda *et al.* reported oryzalin, but not bistheonellide or latrunculin B, altered the vacuole structure, suggesting microtubules, not F-actin, regulates the vacuole (Oda et al., 2009). In addition, dual observation of the tonoplast and microtubules and electron microscopy show microtubules are closely associated with the vacuoles (Oda et al., 2009). Interestingly, the vacuolar system of filamentous fungi is microtubules-mediated (Ashford, 1998; Cole et al., 1998), making the vacuole regulation of *P. patens* chloronemata closer to fungi than higher plants.

1.4 Ion gradients in tip growing cells

Tip growing cells have cytoplasmic ion gradients that are important for several mechanisms, including growth regulation, turgor pressure generation, and cell wall maturation (Michard et al., 2016). Ion gradients at the cell's apex might have a role in the movement of exocytic vesicles, which have a negative surface charge (Heslop-Harrison and Heslop-Harrison, 1982), towards the tip by electrostatic or osmotic force (Michard et al., 2016). Furthermore, they could participate in water transport for the generation of the turgor pressure necessary for growth (Alves et al., 2009). Ion gradients have been mostly characterized in pollen tubes and root hairs, in which, among others, cytoplasmic tip oriented Ca^{2+} , H^+ , Cl^- and K^+ gradients have been described (Peter K. Hepler et al., 2001; Alves et al., 2009; Rounds and Bezanilla, 2013; Michard et al., 2016). As previously mentioned, both pollen tubes and root hairs have an oscillatory growth, and it is

believed this growth fashion is driven by the ions oscillations (Michard et al., 2016). The two most studied ions, especially in relation to growth regulation, are H^+ and Ca^{2+} . A directionality for influx-efflux of H^+ and Ca^{2+} has been described, with extracellular influx at the tip area and efflux at the shank (Alves et al., 2009). H^+ and Ca^{2+} are stored in intracellular reservoirs, mainly the vacuole, mitochondria, and vesicles for H^+ and the ER and vacuole for Ca^{2+} (Alves et al., 2009). Transporters and ion pumps located in the plasma membrane, tonoplast, and ER membrane allow for ion efflux-influx. The H^+ oscillations cause an increase and decrease in pH, alternating the presence of low pH at the very apex and of an alkaline band in the subapical region. The Ca^{2+} gradient increases toward the apex reaching 10,000 nM in pollen tubes (Messerli et al., 2000) and 1,500 nM in root hairs (Wymer et al., 1997), and it decreases to basal levels (100-300 nM (Hepler, 2016)), 20 μ m from the plasma membrane (Wymer et al., 1997). The oscillatory behavior of both H^+ and Ca^{2+} has been correlated with growth. In fact, a decrease in pH is observed a few seconds after a growth peak in pollen tubes (Michard et al., 2008) and a maximum in Ca^{2+} concentration appear a few seconds after the growth peak, in both pollen tubes (4 seconds delay) (Messerli and Robinson, 1997) and root hairs (Monshausen et al., 2008). When growth is stopped by caffeine or low temperature, the Ca^{2+} gradients dissipates, and the Ca^{2+} influx is reduced (Pierson et al., 1996). Similarly, when Ca^{2+} concentration is artificially increased (Bibikova et al., 1997) or reduced with Ca^{2+} channel blockers Lanthanum (La^{3+}) or Gadolinium (Gd^{3+}), growth is arrested (Wang et al., 2004). Only recently, cytoplasmic gradients in relation to *P. patens* protonemal growth have been explored, with particular focus on Ca^{2+} (Bascom et al., 2018b). By using the FRET-based calcium probe Yellow-Cameleon 65, Bascom *et al.* observed a fluctuating tip oriented calcium gradient (Bascom et al., 2018b). To test the relationship between Ca^{2+} oscillations and cell growth, Bascom *et al.* recorded the Ca^{2+} oscillations while artificially reducing growth pharmacologically

(latrunculin B), genetically (loss of function of the actin interacting protein AIP1), and mechanically (physical barrier). In all these cases, growth reduction results in Ca^{2+} oscillations of longer periods, showing growth and Ca^{2+} are related (Bascom et al., 2018b). In addition, these results relate the reduction of F-actin to tip Ca^{2+} oscillations. Finally, via a cross-correlation analysis, Bascom *et al.* report the tip F-actin enrichment characteristic of tip growing cells and the apical Ca^{2+} signal are anticorrelated. High levels of F-actin are only present when the Ca^{2+} concentration is low (Bascom et al., 2018b).

1.5 Modeling of tip growth

To elucidate the generation of cell polarity and unravel the mechanisms behind persistent polarized growth, it is necessary to undertake a multidisciplinary approach that integrates biology, mathematics, and physics. At the molecular level, a variety of players participate in polarized growth, such as, among others, the F-actin cytoskeleton, myosin XI motors, regulated secretion, ion fluxes, and cell wall loosening enzymes. However, at the mesoscopic level, the morphology of the cell is dictated by the law of physics (Campàs and Mahadevan, 2009). Specifically, a collection of mesoscopic parameters determines the properties of the wall, such as the turgor pressure, the cell wall rheology (which depends on the local wall viscosity), the secretions rate, and the cell wall lateral tension (Campàs and Mahadevan, 2009). These parameters, affected by the molecular mechanisms, confine the possible shapes the cell can assume. In the past two decades, several mathematical modeling efforts attempted to deepen our understanding of the tip growth mechanism. Modeling has been performed in pollen tubes, in which the cell wall is assumed to be viscous (Campàs and Mahadevan, 2009; Campas et al., 2012), or not viscous (Rojas et al., 2011), and root hairs (Shaw et al., 2000; Dumais et al., 2004).

1.6 Plants immune response to biotic and abiotic stresses

Plants are often exposed to a variety of harmful biotic (such as bacteria, fungi, viruses, insects) and abiotic (such as drought, salinity, temperature, mechanical injury) stresses. Due to their sessile nature, the development of the plant immune response system was paramount for plant evolution (Chisholm et al., 2006). The first line of plant defense lies on the plasma membrane, in which pattern recognition receptors (PRRs) recognize microbe-associated molecular pattern (MAMP) or pathogen-associated molecular pattern (PAMP), triggering the response (Altenbach and Robatzek, 2007; Zipfel, 2014) (Figure 1.2). In *A. thaliana*, the bacterial proteins flagellin and the factor EF-Tu are recognized by the PRR FLS2 and EFR1, respectively (Gomez-Gomez and Boller, 2000; Zipfel et al., 2006). Chitin, a major component of fungal cell wall, is recognized by the PRR LysM-RLP CEBiP in rice (Kaku et al., 2006) and by the receptor complex LYK5-CERK1 in *A. thaliana* (Cao et al., 2014). Recent work showed *P. patens* expresses the PRR CERK, but homologs of *A. thaliana* FLS2 and EFR1 have been found (Bressendorff et al., 2016). Most of the PRR include receptor-like kinases, which have a receptor and a signal transduction domain, receptor-like proteins, which have an extracellular and membrane domain but lack a signal transduction domain, and extracellular binding proteins (Chisholm et al., 2006). Interaction of the PRR with MAMP/PAMP triggers a signal transduction cascade that results in the so-called PAMP-triggered immunity (PTI), which aims to block the infection before pathogens enter the plant (Chisholm et al., 2006). This first line of response includes an increase of Ca^{2+} concentration and production of reactive oxygen species (ROS), activation of mitogen-activated protein kinases, and transcriptional activation of immune-related genes (Macho and Zipfel, 2014). However, microbes evolved methods to circumvent the initial plant response, usually via secretion of effector proteins that interfere with the defense signaling cascade. To avoid succumbing, plants co-evolved a secondary

response that targets the effector proteins, defined effector-triggered immunity. In this second line of defense, intracellular nucleotide-binding/leucine-rich-repeat (NLR) receptors recognize the effectors, triggering a robust response to eliminate the pathogen (Cui et al., 2015). This response involves a variety of events, such as activation Ca^{2+} and mitogen-activated protein kinase (MAPK) cascades, production of ROS and nitric oxide (NO), accumulation of salicylic acid and jasmonic acid, transcriptional defense gene reprogramming, deposition of callose in the site of infection, and lignification of the cell wall. (Chisholm et al., 2006; Cui et al.). Overall, this dramatic response is called “hypersensitive response” and culminate in programmed cell death. Cell death at the point of pathogen entry protects the rest of the tissue from infection (Balint-Kurti, 2019).

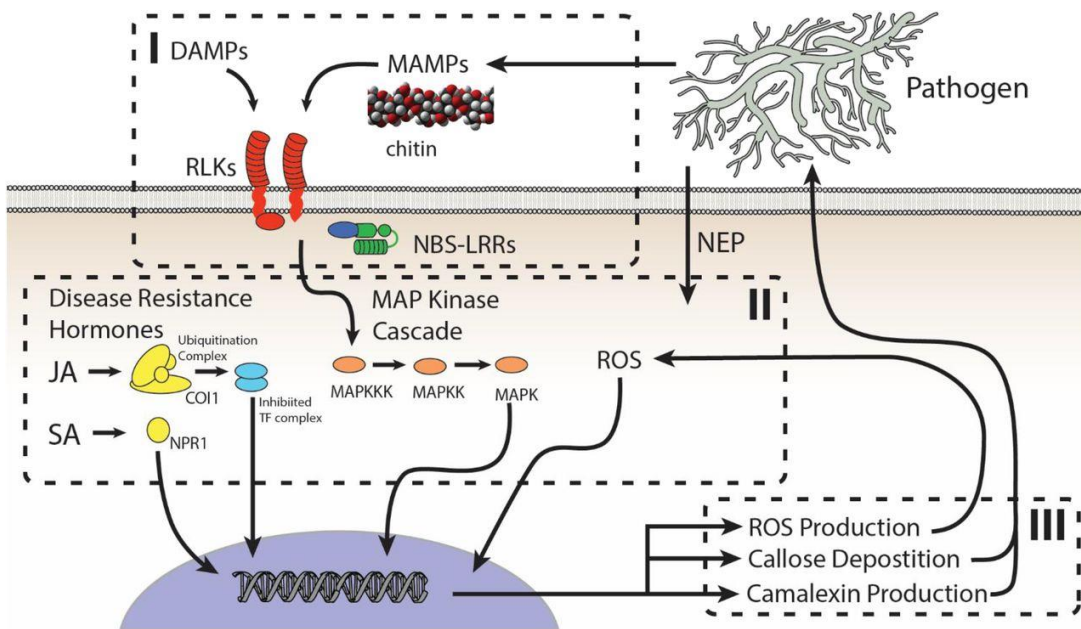


Figure 1.2 Schematic representation of immune response in plants. The response depicted in the figure can be divided in three parts. First (I), MAMPs of the pathogen, in this case a fungus, are detected by the RLK receptor. Second (II), downstream signal transduction is mediated by MAPK signaling, and result in, among others, transcription activation of defense related genes, reactive oxygen species (ROS) production, callose deposition (III). ROS and disease resistance hormones can participate in shaping of the response. Modified from (Corwin and Kliebenstein, 2017).

1.6.1 The role of Ca²⁺ in plant's immune response

Ca²⁺ plays an important role in the plant's development and homeostasis, affecting, among others, cell growth, membrane structure, cell wall rigidity, secretion, and signal transduction (Hepler, 2005). Furthermore, Ca²⁺ is a key secondary messenger in animals and plants. The so-called “Ca²⁺ signature” plays a crucial role in the cellular response to environmental stimuli by signaling downstream effectors and amplifying the response (Edel et al., 2017). In the last decade, research efforts investigated the involvement of Ca²⁺ in plant immune response since the cytoplasmic increase of Ca²⁺ is one of the earliest events observed upon biotic and abiotic stresses (Seybold et al., 2014). In an unstimulated plant cell, the [Ca²⁺]_{cyt} is about 10⁻⁷, while upon stimulation, it reaches concentrations in the μM range (Edel et al., 2017). In the past two decades, the generation of intensity-based genetically encoded Ca²⁺ sensors have facilitated the detection of the local ion concentration and pushed forward the investigation of the Ca²⁺ response (Miyawaki et al., 1997; Nakai et al., 2001; Horikawa et al., 2010; Akerboom et al., 2013). Among others, Nakai *et al.* developed a high-affinity probe made of a single GFP (G-CaMP) linked to a calmodulin and an M13 fragment (Nakai et al., 2001) and Miyawaki *et al.* generated the fluorescent indicator “cameleon”, a FRET sensor that includes a GFP, a calmodulin, the M13 peptide, and a YFP (Miyawaki et al., 1997).

In *A. thaliana*, osmotic stress results in an increase in Ca²⁺ that is detected in leaves, roots, and guard cells (Yuan et al., 2014; Cao et al., 2017). Similarly, *A. thaliana* response to biotic stress, such as herbivore attack, is Ca²⁺-mediated in a glutamate-dependent mechanism that triggers a Ca²⁺ response (Toyota et al., 2018). Interestingly, the response originates at the site of herbivore attack, but quickly propagates to the whole plant (Toyota et al., 2018). Recently, Thor *et al.* reported in *A. thaliana* the Ca²⁺ channel OSCA 1.3 is activated during stomatal immunity (closure

of stomatal pores to limit infection) (Thor et al., 2020). Detection of flg22 by FLS2 activates the kinase BIK1, which in turn activated OSCA 1.3 causing an influx of Ca^{2+} (Thor et al., 2020). In *P. patens*, the abiotic stressors drought and salinity cause a burst of Ca^{2+} waves that originate at the base of the gametophore and extends to the whole plant, resulting in a systemic response (Storti et al., 2018). The cytoplasmic increase in Ca^{2+} concentration upon stress is detected by a set of Ca^{2+} -binding proteins (sensors) that translate and relay the signal. The majority of Ca^{2+} sensors, upon interaction with the ion, undergo a conformational change, resulting in regulation of their catalytic activity or activating an interactor protein (Aldon et al., 2018). Ca^{2+} sensors are classified into four groups: calmodulin, calmodulin-like proteins, Ca^{2+} -dependent protein kinases, and calcineurin B-like proteins. Activation of these sensors results in downstream signaling that mainly results in the transcription of defense-related genes (Seybold et al., 2014).

1.7 Regulation of cell polarity via small GTPases

G-proteins are guanine nucleotide-dependent molecular switches essential for signal transduction in eukaryotic cells. They recover, among others, an essential role in cell polarity, cell growth, morphogenesis, and hormone response (Zheng and Yang, 2000). They hydrolyze GTP, and they exist in a GTP-bound membrane-associated active state, and in a GDP-bound cytosolic inactive state (Syrovatkina et al., 2016). The two main classes of G-proteins are heterotrimeric G proteins and the Ras superfamily of small GTPases (Zheng and Yang, 2000). The Ras small GTPases include five subfamilies, Ras, Rho, Arf, Rab, and Ran (Molendijk et al., 2004). Small GTPases recover an essential role in the regulation of cell polarity; here, we will focus on Rho of plants and Rabs because of their involvement in cell polarity in plants.

1.7.1 Rho of plants and cell polarity

Among the regulators of cell polarity in plants, a central place is recovered by the Rho family of small GTPases (Yang, 2002; Nagawa et al., 2010; Scheible and McCubbin, 2019). While in other organisms, the Rho subfamily has evolved in different subfamilies, RHO, CDC42, and RAC in animals and CDC42 and RHO in yeasts, plants express a unique family of Rho GTPases, called “Rho-like GTPases of plants” (ROPs) (Nagawa et al., 2010). Active ROP interact with downstream effector proteins, such as the ROP interacting CRIB domain proteins (RICs) (Bourne et al., 1991; Wu et al., 2001). This protein family is mainly involved in the regulation of cytoskeleton reorganization and dynamics, vesicle trafficking, and determination of cell polarity (Molendijk et al., 2004; Nagawa et al., 2010). In *A. thaliana* pollen tubes and ROP1 and RAC homologs respectively are localized at the tip of pollen tubes, suggesting a role in polarized elongation (Lin et al., 1996; Kost et al., 1999). Expression of dominant-negative mutant of *Rop1* in *A. thaliana* pollen tubes proved *Rop1* regulates F-actin proper orientation and dynamics, which are essential for pollen tube growth (Fu et al., 2001). Further studies demonstrated *Rop1* regulation of F-actin dynamics is mediated by two effectors, RIC3 and RIC4; RIC4 promotes F-actin assembly, while RIC3 promotes the increase in Ca^{2+} signaling that result in F-actin depolymerization (Gu et al., 2005). Importantly, the ROP mediated regulation of F-actin via RIC3 and RIC4 has an effect in polarized vesicle accumulation and secretion (Lee et al., 2008). Hwang et al demonstrated ROP1 signal oscillates at the tip of tip growing cells with a similar frequency of growth oscillations, and leads growth (Hwang et al., 2005). While *A. thaliana* genome has 11 ROPs and 11 RICs, *P. patens* expresses only 4 ROPs and 1 RIC, making this land plant a suitable model to study ROP signaling in tip growth (Eklund et al., 2010). ROP4 signal at the cell’s apex peaks in a narrow area (about 5 μm wide) and GEF signal is also localized in a narrow area at the

tip (Ito et al., 2014; Le Bail et al., 2019). Burkart et al showed that, in *P. patens*, the four ROPs genes are functionally redundant and they are essential for tip growth (Burkart et al., 2015). In fact, moss cells in which ROPs have been silenced appear unpolarized and spherical (Burkart et al., 2015). On the other hand, overexpression of *Rop2* result in polarized cells that exhibit a swollen tip (Ito et al., 2014). Furthermore, ROPs loss of function results in increase in F-actin dynamics, and affects secretion of cell wall components (Burkart et al., 2015). Interestingly, while silencing of RIC does not have an effect on polarized growth, loss of function of ROPs regulators result in reduction of cell polarity in *P. patens* (Bascom et al., 2019). Hence, evidences show ROPs mainly regulate the reorganization and dynamics of the cytoskeleton and are responsible for cell polarization.

1.7.2 Rabs and polarized exocytosis

The compartmentalized nature of eukaryotic cells results in a high volume of vesicular trafficking across compartments and to the membrane. Rab GTPases are essential regulators of membrane trafficking and are involved in all the steps of the secretion process: vesicles formation, transport, docking, and fusion to the membrane (Grosshans et al., 2006; Pfeffer, 2017). The ability of Rabs to interact with a wide variety of effectors and switch between an active/inactive state provides spatial and temporal specificity to vesicle delivery (Zerial and McBride, 2001). Regulation of vesicle trafficking by Rabs, especially in relation to cell polarity, has been extensively characterized in *S. cerevisiae*, which expresses 11 Rabs (Grosshans et al., 2006; Park and Bi, 2007; Novick, 2016). In *S. cerevisiae*, secretion of Golgi derived secretory vesicles to the nascent bud is paramount for cell division and budding (Chiou et al., 2017). In this organism, trafficking of vesicles filled with wall material is driven by Myo2, the homologous to the animal myosin V, in concert with the Rab GTPases Ypt31 and Ypt32 (Schott et al., 1999; Lipatova et al., 2008).

Lipatova *et al.* demonstrated myo2 is an effector of Ypt31/32, that GTP-bound Ypt31/32 interact with myo2p and that this interaction is essential for polarized secretion (Lipatova et al., 2008). Furthermore, Jin *et al.* showed the interaction between myo2p and the GTPase Sec4 is essential for vesicle fusion to the membrane (Jin et al., 2011). Vesicle fusion is mediated by myo2 interaction with subunits of the exocyst complex (Sec15) (Jin et al., 2011; Donovan and Bretscher, 2012). Mechanistic details of myosin XI and Rab driven membrane trafficking in plants have not yet been elucidated, but evidence show a similar mechanism driven by myosin XI, Rabs, and the exocyst mediate polarized secretion (Elliott et al., 2020). In *A. thaliana*, there are 57 Rab GTPases (grouped in clades RabA-H), and members of RabA, RabE, and RabH have been related to post-Golgi vesicle trafficking (Rutherford and Moore, 2002). The plant RabE GTPase family is homologous to the *S. cerevisiae* Sec4 (Rutherford and Moore, 2002). Evidence in *A. thaliana* and *N. benthamiana* show RabE GTPase localized to the Golgi and plasma membrane, and it is related to cell size (Speth et al., 2009; Ahn et al., 2013). Interestingly, RabE was found to function together with the SCD complex and the exocyst in regulating post-Golgi vesicle trafficking in *A. thaliana* (Mayers et al., 2017). Recently, Orr *et al.* demonstrated RabE GTPase colocalizes with myosin XI at sites of active exocytosis (cell tip and cell plate) in *P. patens* (Orr et al., 2019). Furthermore, Orr *et al.* showed RabE14 interact with myosin XI tail in a yeast two hybrid assay, and that RabE loss of function results in reduced polarized growth, showing this GTPase is functionally related to plant growth (Orr et al., 2019). The role of Rabs in plants has not been elucidated in detail, but these evidences show Rabs are mainly involved in vesicle trafficking.

1.8 The cytoskeleton

1.8.1 F-actin architecture in tip growing cells

A substantial advancement of our knowledge of F-actin organization in tip growth cells originated from the use of fluorescent actin-binding probes, such as Lifeact-GFP (Riedl et al., 2008; Vidali et al., 2009a) mTalin (Kost et al., 1998) and the actin-binding domain of fimbrin (Sheahan et al., 2004). The use of such probes avoided the need for fixation of the plant tissue, which can result in artifacts in the cytoskeleton structure (Vidali et al., 2009a). Live cell imaging of F-actin enabled the collection of both structural and dynamics information. From a structural perspective, the F-actin cytoskeleton of tip growing cells exists in different conformations. Moss protonemata have two populations of F-actin: a cortical F-actin, that resides on the cortex of the cell, and an apical F-actin enrichment, that is essential for cell growth (Vidali et al., 2009a; Rounds and Bezanilla, 2013). Root hairs and pollen tube exhibit, in addition to the cortical and apical F-actin, long actin bundles in the central region of the cell (Jásik et al., 2016). These bundles are the tracks for cytoplasmic streaming characteristic of these cells (Rounds and Bezanilla, 2013). The organization and the size of the apical F-actin vary among plant species and cell types (Figure 1.3). In *P. patens* in caulonemata cells, the apical F-actin is dense and compacted in a defined small area, while in chloronemata it is broader and less focused (Vidali et al., 2009a). In *L. longiflorum* pollen tubes the apical F-actin it is limited to the cortex, and it is referred to as “fringe” (Lovy-Wheeler et al., 2005; Vidali et al., 2009a; Rounds et al., 2014), while in *N. tabacum* root hairs and pollen tubes the apical F-actin is also localized in the cytoplasmic tip area, not only at the cortex, and it is called “mesh” (Chen et al., 2002; Vidali et al., 2009a). As we will discuss in future paragraphs, the main role of the apical F-actin is to drive secretion of secretory vesicles to the growing apex of the cell. However, it has been proposed an additional role of the apical F-actin is to “trap” secretory vesicles

close to the apex (Smith and Oppenheimer, 2005), and to prevent organelles from invading the tip region (Ketelaar, 2013). The F-actin cytoskeleton in all tip growing cells is very dynamic, constantly polymerizing and depolymerizing and rapidly remodeling (Vidali et al., 2009a; Vidali et al., 2010). The F-actin cytoskeleton and its dynamics are essential for the maintenance of persistent growth, so we will carefully review literature that supports F-actin's role in tip growth.

1.8.2 F-actin cytoskeleton in tip growth

The F-actin cytoskeleton recovers an essential role in polarized growth, and most of the evidence supporting this notion was collected via pharmacological inhibitors. In *L. longiflorum* pollen tubes, treatment with Latrunculin B at nanomolar concentrations inhibits pollen grain germination and

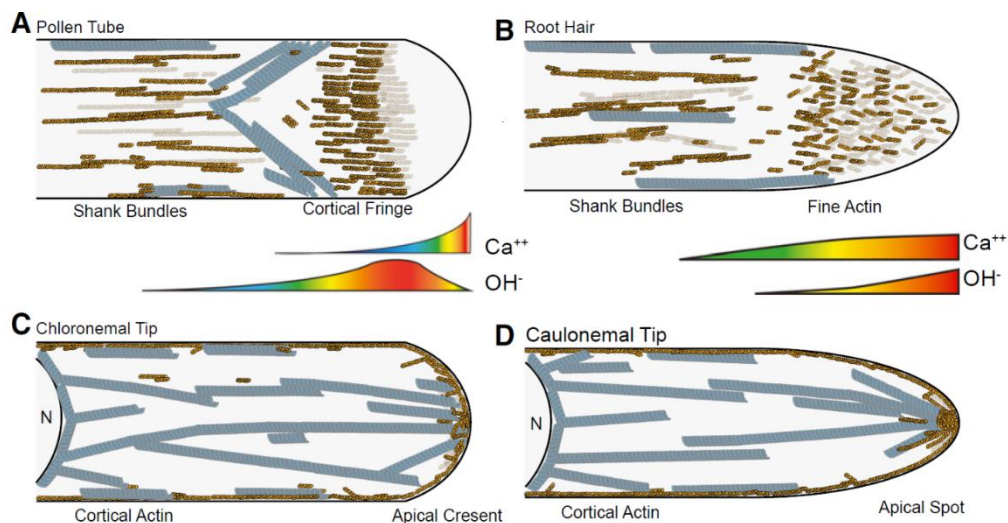


Figure 1.3 Comparative architecture of the cytoskeletal elements and ion gradients in the tip growth models. F-actin in yellow and microtubules in light gray. A. Pollen tube (modeled after *L. longiflorum*). F-actin is localized cortically at the apex (fringe) and in bundles at the shank. The microtubules are shaped as an inverted cone just behind the F-actin fringe, and cortically at the shank. B. Root hair (modeled after *A. thaliana*). Short F-actin filaments fill the apex, while microtubules are mostly cortical in the shank area. C. Moss chloronema (modeled after *P. patens*). F-actin occupies a broad area at the cell tip, and is localized at the cortex at the shank. Microtubules are both cortical and cytoplasmic and converge at the tip. D. Moss caulonema (modeled after *P. patens*). F-actin is densely packed in a narrow spot at the cell's apex. Microtubules are both cortical and cytoplasmic and converge at the tip, in a narrower area compared to chloronema's microtubules. Modified from (Bascom et al., 2018a).

tube growth (Gibbon et al., 1999). Furthermore, inhibition of F-actin polymerization via the increase of profilin concentration, DNAase I, latrunculin B and cytochalasin B, showed F-actin is directly involved in pollen tube growth (Vidali et al., 2001). Furthermore, in the same study it was proved that F-actin polymerization, not cytoplasmic streaming, is the limiting factor for pollen tube elongation (Vidali et al., 2001). Similarly to pollen tubes, the inhibition of F-actin in *P. patens* protonemata stops the growth in a dose-dependent manner and show F-actin is essential for proper protonemal expansion (Harries et al., 2005; Finka et al., 2007; Vidali et al., 2009a).

The aforementioned studies strongly demonstrated F-actin is essential for polarized cell growth, but what is the F-actin mediated mechanism that supports growth? Even if strong direct evidence is still lacking, the assumption in the field is that F-actin, together with myosin motors, direct membrane trafficking at the cell apex. In pollen tube and root hairs, but not in moss protonemata, a myosin-driven cytoplasmic streaming along F-actin bundles transport vesicle to the tip area (Peter K. Hepler et al., 2001). When root hairs expressing myosin XIK-YFP are treated with latrunculin B, myosin XI localization at the root tip is disrupted (Park and Nebenfuhr, 2013). Furthermore, when root hairs are treated with a low concentration of latrunculin B (10 nM), growth is not completely inhibited, but the cell tip becomes round, showing F-actin is involved in restricting growth at the apex (Ketelaar et al., 2003). In addition, modeling efforts in *P. patens* show an active transport that relies on F-actin is essential for tip growth: a mechanism based solely on vesicle diffusion cannot support growth (Bibeau et al., 2018). Recently, Bibeau *et al.* demonstrated the linear trajectory of myosin XI and secretory vesicles at the tip of caulonema cells is F-actin dependent (Bibeau et al., 2020).

1.8.3 F-actin binding proteins

Fluorescent labeling of F-actin in tip-growing cells, and in plant cells, generally show that the actin filaments are a highly dynamic network (Staiger et al., 2009; Vidali et al., 2009c; Smertenko et al., 2010). For instance, Staiger *et al.* observed in *A. thaliana* hypocotyl epidermal cells, most individual cortical actin filaments have a 30 seconds half-life; filaments grow at 1.7 $\mu\text{m}/\text{sec}$ and are rapidly severed (Staiger et al., 2009). The mechanism they observed is not compatible with a treadmilling mechanism, and it is referred to as “stochastic dynamic” (Staiger et al., 2009). F-actin is constantly remodeling through polymerization, depolymerization, severing, and nucleation events; this plasticity is mediated by actin-binding proteins (Dos Remedios et al., 2003; Pollard, 2016). Eukaryotic cells have a cytoplasmic pool of monomers of G-actin, most of which are bound to the actin-monomer-binding protein profilin (Dos Remedios et al., 2003; Pollard, 2016). Actin filament elongation starts from a so-called “seed” formed by a small oligomer of G-actin subunits. Small oligomers, especially dimers and trimers, are very unstable and gain stability when a fourth monomer is added (Pollard, 2016). Hence, since F-actin polymerization is an unfavorable event, polymerization is dependent on regulatory proteins, mainly formins and arp2/3 complex, to initiate the process (Pollard, 2016). Once the filament is formed, turnover occurs via ADF/cofilin, villin, gelsolin and actin interacting protein 1 (Dos Remedios et al., 2003; Pollard, 2016). Multiple pieces of evidence show actin-binding proteins, effect on F-actin dynamics, is essential for tip growth. In *P. patens*, loss-of-function of profilin (a family of three genes) result in stunted unpolarized plants and reduced cell proliferation (Vidali et al., 2007). Similarly, RNAi of formin II (a class of two genes) inhibits polarized growth (Vidali et al., 2009c). It is not surprising that profilin and formin II have a comparable negative effect on cell growth, in fact, one of the two formin homology domains (FH1) interacts with profilin (Chang et al., 1997), to promote F-actin elongation. RNAi

of the subunit *arpc4* of the *arp2/3* complex resulted in reduced polarized growth (Perroud and Quatrano, 2006). In addition, also ADF/cofilin and actin interactin protein 1 (both coded by a single gene in *P. patens*) are essential for cell polarization (Augustine et al., 2008; Augustine et al., 2011).

Importantly, Ca^{2+} plays an important role in regulating a subset of the actin-binding protein, hence Ca^{2+} indirectly regulate the F-actin cytoskeleton (Pollard, 2016; Bascom, 2018 #2217). Villin severing activity is Ca^{2+} -mediated (Huang et al., 2004). In addition, profilin binding affinity to G-actin is Ca^{2+} mediated (higher affinity for G-actin in higher $[\text{Ca}^{2+}]$) (Kovar et al., 2000). Since profilin-G-actin is the substrate of formins, also formins are indirectly affected by Ca^{2+} concentration (Bascom et al., 2018a). As previously discussed, tip growing cells have an oscillatory Ca^{2+} gradient at the tip, which results in oscillations in the stability of the actin cytoskeleton. This plasticity is probably important for the dynamic organization of the growing machinery at the cell tip.

1.8.4 The microtubules: architecture and role in tip growth

In tip growing cells, microtubules have an architecture similar to the one of F-actin (Figure 1.3) (Rounds and Bezanilla, 2013, Orr, 2020 #3075). In fact, in pollen tubes, root hairs and protonemata microtubules are longitudinally located at the cell cortex and in the cytoplasm (Sieberer et al., 2005; Cheung and Wu, 2008). While in pollen tubes and root hairs, microtubules are excluded from the apical area of the cell (Rounds and Bezanilla, 2013), in protonemal they are not, reaching the very apex of the cell (Doonan et al., 1985; Ding et al., 2018; Wu and Bezanilla, 2018). In *P. patens*, microtubules accumulate in a spot at the cell tip and are oriented with the plus growing end toward the cell's apex (Hiwatashi et al., 2014).

Even if F-actin is mainly involved in tip growth, growing evidence shows that microtubules plays an important role in this process. *A. thaliana* root hairs treated with oryzalin and taxol are polarized, but the directionality of growth is altered, and cells grow in a “wavy” fashion (Bibikova et al., 1999; Ketelaar et al., 2003). Furthermore, in the same study Bibikova *et al.* observed, when treating with a higher concentration of these drugs, the root hairs bifurcate and form multiple tips (Bibikova et al., 1999). In root hairs from *N. tabacum*, both secretion and endocytosis are affected by microtubules disruption via Nocodazole (Idilli et al., 2013). In the conifer *Picea abies* (Norway spruce), depolymerization of microtubules inhibits pollen tube elongation (Anderhag et al., 2000). In *P. patens*, treatment with the microtubule depolymerizing drug cremart produces a swollen tip (Doonan et al., 1988). How the microtubules specifically affect polarized growth has not completely been elucidated. Some evidence shows that microtubule-based motor kinesins have a regulatory effect on tip growth (Yang et al., 2007; Cai and Cresti, 2010). For instance, KINID1, a plus end-directed motor, accumulates at the apex of *P. patens* caulonemata cell (Hiwatashi et al., 2014). Deletion of KINID1 causes aberrant formation of multiple microtubules foci at the apex, and loss of directionality of growth (Hiwatashi et al., 2014). Evidence in both *P. patens* protonemata and *A. thaliana* pollen tubes show microtubule might affect tip growth by organizing and stabilizing the tip F-actin cytoskeleton (Zhu et al., 2013; Wu and Bezanilla, 2018). Wu and Bezanilla showed at the apex of protonemal cells, the F-actin spot overlaps with the microtubule focus, showing that interaction via the two cytoskeletons might contribute to growth (Wu and Bezanilla, 2018). Furthermore, when microtubules are depolymerized, the F-actin apical spot appears in multiple aberrant locations at the cell tip, showing microtubules might restrict the site of F-actin accumulation (Wu and Bezanilla, 2018).

1.9 Myosin XI, a motor essential for plant growth and development

Myosin XI, together with myosin VIII, are the two families of myosin motors existing in plant cells and are both evolutionarily related to animal and fungal myosin V (Mooseker and Cheney, 1995; Peremyslov et al., 2011). The actin-dependent motor myosin XI plays crucial roles in plant growth and development. The protein is a dimer, and each monomer is composed of a C-terminal globular tail domain (cargo binding), a coiled-coil domain (dimerization), a neck domain (lever arm), and an N-terminal motor domain (ATP hydrolysis and F-actin interaction) (Trybus, 2008). Myosin XI pairs the hydrolysis of ATP with a conformational change that results in its movement along an actin filament (in 35 nm steps in the fastest known myosin XI in *N. tabacum*) (Tominaga et al., 2003). Interestingly, the motor domain determines the velocity of the movement, and the rapidity of the motor is proportionally related to plant size (Tominaga et al., 2013). In *A. thaliana*, the myosin XI family encodes for 13 genes (myosin XI A-H and MYA1-2) (Peremyslov et al., 2011), while in *P. patens* there are only two myosin XI genes, myosin XIa and XIb (Vidali et al., 2010). Imaging efforts elucidated the subcellular localization of myosin XI in plants. First, immunofluorescence studies on fixed cells show a subgroup of myosin XI colocalized with the ER in *N. tabacum* cells (Yokota et al., 2009), with peroxisomes in *A. thaliana* (Hashimoto et al., 2005), and at the tip of pollen tube in *L. longiflorum* (Yokota et al., 1995). *In vivo* studies of fluorescent full-length myosin XI allowed for more accurate detection of its localization, as well as for dynamic information. Vidali *et al.* were the first to study the localization of a full-length myosin XI in plants, taking advantage of the reduced copies of this gene in *P. patens* compared to *A. thaliana* (Vidali et al., 2010). Vidali *et al.* observed myosin XI-GFP localizes at the tip of protonemal cells, importantly, spatially overlapping with both the F-actin spot and the VAMP-labelled vesicle cluster (Vidali et al., 2010; Furt et al., 2013). In *A. thaliana*, myosin XIK-YFP also

colocalizes with F-actin and with the post-Golgi secretory vesicle marker SCAMP2, and with a portion of the ER (Peremyslov et al., 2012). Furthermore, myosin XIK-YFP localizes at the tip of growing root hairs, and along F-actin bundles at the shank of the root hair (Peremyslov et al., 2012).

At the cellular level, the role of myosin XI has been linked to cytoplasmic streaming, cell expansion, and F-actin organization (Geitmann and Nebenfuhr, 2015; Ryan and Nebenfuhr, 2018). Knock out via t-DNA insertion of myosin XI-K and MYA2 resulted in reduced trafficking of Golgi, peroxisomes, and mitochondria in root hairs and epidermal cells in *A. thaliana* (Peremyslov et al., 2008). Comparable results were obtained by Prokhnevski *et al.* (Prokhnevsky et al., 2008). Similarly, triple and quadruple knockouts of myosin XI mutants exhibited reduced growth, delayed flowering time, decreased leaf expansion, and reduced Golgi and peroxisome motility (Peremyslov et al., 2010). In addition, Ueda *et al.* demonstrated that, among all myosin XI in *A. thaliana*, myosin XI-K is mostly involved in ER streaming along F-actin (Ueda et al., 2010). Interestingly, evidence shows myosin XI is engaged in the organization of the F-actin cytoskeleton; such is the case for epidermal *A. thaliana* cells (Peremyslov et al., 2010), cotyledon epidermal cells (Ueda et al., 2010), and pollen tubes (Madison et al., 2015). In all these examples, myosin XI knock-out mutants exhibit an aberrant distorted organization of F-actin bundles compared to the wild type (Peremyslov et al., 2010; Ueda et al., 2010; Madison et al., 2015). In addition, Park et al. showed that loss of myosin XI-K results in a considerable reduction of F-actin dynamics in root hairs (Park and Nebenfuhr, 2013).

1.9.1 Myosin XI in tip growth

Due to the dependence of polarized growth on F-actin and endomembrane secretion, and due to fluorescent and functional myosin XI data, the underlying assumption in the field is that myosin XI delivers secretory vesicles containing cell wall polymers at the cell tip. Even if this has not been directly proved, a variety of indirect evidence supports this model. Knock-out mutants of myosin XI isoforms in *A. thaliana* result in a defect in root hairs elongation (Peremyslov et al., 2008; Prokhnevsky et al., 2008; Peremyslov et al., 2010), and reduction of pollen tube growth speed (Madison et al., 2015). Furthermore, knock-out of myosin XI-K in *A. thaliana* results in impairment of root hairs and trichomes (Ojangu et al., 2007). In *P. patens*, evidence of myosin XI involvement in tip growth emerges from loss-of-function and fluorescent studies (Vidali et al., 2010). Vidali *et al.* showed simultaneous RNAi of myosin XIa and myosin XIb results in unpolarized plants, showing myosin XI is essential for cell polarization (Vidali et al., 2010). Furthermore, fluorescent labeling of myosin XI shows it localizes at the apex of protonemal cells and emerging branches (Vidali et al., 2010). Interestingly, myosin XI loss of function results in a defect in F-actin organization but not in F-actin dynamics (Vidali et al., 2010). Fluorescent cross-correlation studies of F-actin and myosin XI at the cell's apex show their signal in *P. patens* are not correlated, with myosin XI leading by 18.6 sec (Furt et al., 2013). This result shows, in *P. patens*, myosin XI could be involved in enriching the local concentration of F-actin (Furt et al., 2013). In addition, in the same study, it was reported myosin XI and VAMP-labelled vesicles fluctuate in phase, suggesting VAMP-labelled vesicles are potentially a myosin XI cargo (Furt et al., 2013). Recently, FRAP studies in *P. patens* caulonemal cells show the recovery of myosin XI at the cell's apex is F-actin dependent (Bibeau et al., 2020).

1.9.2 Regulation of myosin XI by Ca²⁺ and calmodulin

Myosin XI is a dimeric protein in which each dimer is characterized by four domains: the N-terminal motor domain, the neck domain, the coiled-coil domain, and the C-terminal tail domain (Trybus, 2008). Among them, the neck domain plays an important role in regulating the mechanical properties of protein activity. In myosin XI, as in myosin V, the neck is characterized by the presence of 6 IQ motifs per heavy chain, which are binding sites for calmodulin (CaM) light chains (Yokota et al., 1999; Tominaga et al., 2003). In the case of myosin V, regulation of the protein is mostly due to autoinhibition, which is affected by Ca²⁺ concentration (Li et al., 2006). In low Ca²⁺, the globular tail domain interacts with a portion of the coiled coil domain, inhibiting the ATPase activity of the motor (Li et al., 2006). Cargo binding or increase of Ca²⁺ (in the micromolar range) cause a conformational change that results in the active conformation (Li et al., 2006). If this autoinhibitory mechanism exists in plants is not known. Avisar *et al.* showed that two amino acids in the myosin XI tail affect its activity, and interestingly, the corresponding amino acids in myosin V are the ones responsible for its autoinhibition (Avisar et al., 2012). This result shows myosin XI could be regulated in a similar way than myosin V, but further studies are needed to confirm this mechanism. Studies in myosin V from chick's brain showed Ca²⁺ causes CaM to detach from the IQ motif, and this results in inhibition of myosin V activity in motility assays (Cheney et al., 1993). Similarly, the *in vitro* motile activity of myosin XI from *Lilium longiflorum* is inhibited by Ca²⁺ (Yokota et al., 1999). Yokota *et al.* demonstrated CaM light chains detach from myosin XI in a Ca²⁺ dependent way (low affinity in high Ca²⁺) (Yokota et al., 1999). A study with myosin XI from tobacco shows CaMs binding affect the length of the neck domain, which functions as a lever arm in the myosin power stroke during motor movement (Tominaga et al., 2012). Ca²⁺-induced CaMs dissociation reduces neck's length (from 24 to 18 nm), reducing

myosin step size (from 35 to 27 nm) (Tominaga et al., 2012). Consistent with this regulation mechanism, it has been reported Ca^{2+} has an inhibitory effect on cytoplasmic streaming in plant cells. This is the case for *Lilium longiflorum* pollen tubes (Kohno and Shimmen, 1988), and leaf cells of *Vallisneria gigantea* (Takagi and Nagai, 1986). Hence, myosin XI activity is negatively regulated by Ca^{2+} , but whether it is also regulated by autoinhibited, as myosin V, remain to be verified.

2. Loss-of-function techniques to study gene function

Loss-of-function (LOF) has been widely used in biology to uncover gene function and led to countless of important discoveries. A variety of LOF techniques are available to experimentalists, and they can be classified according to their way to target expression. In fact, inhibition of expression can be achieved targeting the genome, specific genes, transcription, mRNA, and the protein of interest (Alonso and Ecker, 2006; Housden et al., 2017). Here, I will briefly review the LOF techniques, with a focus on temperature-sensitive alleles. The genome of an organism can be targeted by X-rays or γ -rays, which generally induce double-strand breaks, via chemical mutagenesis, which induces mostly point mutations, and via transposon-mediated gene disruption (Baskin et al., 1992; Anderson, 1995; Meinke et al., 1998). These techniques induce a random mutation and are mostly used for unbiased “hypothesis-generating” forward genetic screens. A drawback of these techniques is that they can generate multiple mutations (EMS treatment in *A. thaliana* seeds can generate 400 mutations per genome (Alonso and Ecker, 2006)), making it difficult to associate the observed phenotype to a single gene. Agrobacterium transferred DNA (T-DNA) insertion has historically been the main technique to generate insertional mutants in *A. thaliana*, but the generation of mutants is lower than chemical mutagenesis (1.5 insertions per transformation), and insertion can exhibit insertional bias (Alonso et al., 2003; Housden et al.,

2017). Differently than unbiased genome targeting, gene editing approaches allow targeting a precise gene of interest. This reverse genetic approach includes Zinc-finger nuclease, TALEN, CRISPR-Cas9 (Nemudryi et al., 2014; Manghwar et al., 2019; Schindele et al., 2020). These methods take advantage of endonuclease induced double-strand break at the targeted site, which will then be repaired via homology-directed repair or non-homologous end-joining. These techniques, especially CRISPR-Cas9, revolutionized functional gene studies, but have some limitations, such as off-target effects, double-strand break-induced genotoxic stress, and narrower generation of mutant alleles compared to random mutagenesis (Zhang et al., 2015; Housden et al., 2017). Even if such generated mutant alleles are paramount to unravel gene function, the drawbacks of these approaches are the lack of reversibility and the limitation posed by targeting essential or pleiotropic genes. In fact, the generation of a null allele of an essential gene often results in lethality. A strategy that offers a strong advantage is offered by temperature-sensitive (TS) alleles (Ben-Aroya et al., 2010). TS alleles are functional at a certain temperature range and become nonfunctional, usually due to protein misfolding, at a higher temperature. Historically, both forward and reverse genetic techniques have been used to generate TS alleles. In forward genetic screens, mutations are introduced upon chemical mutagenesis, UV, and T-DNA insertion, and the mutants are screened for a phenotype of interest. The mutated gene responsible for the phenotype is then cloned and sequenced for identification, usually a time-consuming and laborious procedure (discussed below). This approach supported the discovery of genes involved in central processes in cell biology, such as cytokinesis, protein, DNA, and RNA synthesis (Hartwell, 1967; Hutchison et al., 1969; Li et al., 2011). On the other hand, in the reverse genetic approach, a TS allele of a specific gene of interest is generated usually via site directed mutagenesis or chemical mutagenesis of the cloned gene. Complementation experiments then confirm the direct link

between the mutant phenotype and the mutagenized allele. This strategy has been used mainly in yeasts to study the function of essential genes, such as the role of actin (Shortle et al., 1984) and RPC40, a subunit of RNA polymerase (Mann et al., 1987). The use of TS alleles offers the great advantage of reducing protein activity within minutes (Vidali et al., 2009b; Housden et al., 2017), and it is reversible. At the transcriptional level, gene modulation can be achieved by modified Cas9 endonuclease fused to transcriptional repressors, to block transcription of specific genes (Gilbert et al., 2013). This technique is promising but has had limited use so far (Housden et al., 2017). Strategies that target the mRNA, such as RNAi and morpholinos, have been extensively used to induce LOF (Heasman et al., 2000; Gunsalus and Piano, 2005). Importantly, these techniques provide only a partial reduction to protein levels, and don't result in complete LOF. This leads to weaker phenotypes, which could be hard to interpret, but it is advantageous if the target is an essential gene. Furthermore, specificity issues in morpholinos have been reported (Blum et al., 2015). A solution to this limitation is the use of inducible RNAi, such as Gal4-UAS in *D. melanogaster* (Brand and Perrimon, 1993), doxycycline-inducible systems in mice (Gossen et al., 1995), and 17 β -estradiol (Guo et al., 2003; Nakaoka et al., 2012) or heat-inducible (Masclaux et al., 2004) systems in plants. This can be imparted in a not systemic way and in a specific developmental stage; however, a reduction is only achieved 24-48 hours or more after induction. Finally, LOF can be achieved via targeting the protein via small molecules inhibitors (Arrowsmith et al., 2015) and degradation systems. Small molecules inhibitors are fast-acting and amenable to high throughput screenings, but only partially reduce protein levels, sometimes only targeting protein domains, and can lack specificity (Arrowsmith et al., 2015). Protein degradation systems, such as proteolysis-targeting chimeras (PROTACs) (Sakamoto et al., 2001) and auxin-inducible degron system (Nishimura et al., 2009), induce the ubiquitin-dependent degradation of a protein

of interest. These approaches can ensure inducible and fast degradation (as little as 15 minutes), hence providing a particularly useful approach for protein functional studies (Housden et al., 2017).

2.1 TS alleles, from random mutagenesis to residue prediction

In the reverse genetics approach, to generate a TS allele, the gene of interest is cloned and subjected to random chemical mutagenesis (sodium disulfite), which usually generates a missense mutation (Shortle et al., 1984; Mann et al., 1987). In this technique, originally developed in yeasts (Shortle and Botstein, 1983; Shortle et al., 1984), the generated pool of mutagenized plasmids is then reintegrated in yeast, producing a library of yeasts. Even if this approach yielded important advancement in our knowledge of biological processes, it is limited since it requires the screening of a large progeny (Shortle *et al.* screened 1200 transformants to identify 11 TS alleles) (Shortle et al., 1984; Varadarajan et al., 1996). While screening a high number of individuals can be manageable for prokaryotes or yeasts, it constitutes a technical challenge for more complex organisms, such as flies or plants. As an example, in the fruit fly *Drosophila melanogaster*, Suzuki *et al.* screened about 250,000 flies to find only one TS allele (Suzuki et al., 1967). Furthermore, it was demonstrated that random mutagenesis in yeasts generates TS alleles non transferable to other organisms, limiting their potential (Vidali et al., 2009b). A turning point in the generation of TS alleles was developed by Varadarajan *et al.*, who developed a method to predict which residue(s) in a protein sequence, if mutated, will generate a TS allele (Varadarajan et al., 1996). Significantly, this technique is only based on the amino acid sequence and does not require information on the three-dimensional structure of the protein (Varadarajan et al., 1996). The method is based on the experimental evidence that mutating a residue buried (high hydrophobicity) in the core of the protein will cause a more dramatic loss in protein stability than a surface residue. This technique

was applied by Chakshusmathi *et al.* to successfully generate TS alleles of bacterial gene CcdB and the yeast gene Gal4 (Chakshusmathi *et al.*, 2004). In 2009, Vidali *et al.* applied this method to *P. patens*, generating TS alleles of the ADF/cofilin and profilin genes (Vidali *et al.*, 2009b). Importantly, Vidali *et al.* show analogous TS mutations of *Arabidopsis thaliana* and *Lilium longiflorum* profilin render the protein TS in *P. patens*, showing the method could be transferable to different organisms (Vidali *et al.*, 2009b).

2.2 The use of temperature-sensitive alleles in plants

For almost three decades, the plant community has adopted the use of TS alleles to study gene function. Most of the studies used the forward genetic approach, and only one study, so far, applied reverse genetics in plants (Vidali *et al.*, 2009b). Here, we briefly review the main discoveries from the use of TS alleles in plants. In 1992, a seminal study from Baskin *et al.* isolated, upon ethyl methanesulfonate (EMS) mutagenesis on *A. thaliana* seeds, root morphogenesis mutants called *rsw1*, *rsw2* (*radial swelling mutants*) (Baskin *et al.*, 1992). These mutants, when exposed at the restrictive temperature (31° C), exhibited reduced anisotropic growth in root cells which resulted in root swelling (Baskin *et al.*, 1992). Interestingly, Arioli *et al.* in 1998 showed *rsw1* codes for a catalytic subunit of the cellulose synthase (Arioli *et al.*, 1998) and Lane *et al.* in 2001 show the *rsw2* gene is allelic to the endo-1,4- β -glucanase KORRIGAN (Lane *et al.*, 2001). *Korrigan* mutants exhibits defect in cell elongation and reduced levels of cellulose microfibrils (Lane *et al.*, 2001). The authors suggest KORRIGAN is involved in stress relaxation during cell expansion (Lane *et al.*, 2001). Another genetic screen via EMS chemical mutagenesis on *A. thaliana* seeds resulted in the isolation of two further TS root swelling mutants, *rsw4* and *rsw7* (Wiedemeier *et al.*, 2002). Later characterization demonstrated *rsw4* codes for a separase, essential for chromosome disjunction (Wu *et al.*, 2010), and *rsw7* belongs to a family of kinesin-5, a plus-end

directed motor essential for microtubule crosslink in mitotic spindle (Bannigan et al., 2007). Whittington *et al.* in 2001, via EMS mutagenesis, isolated a TS gene coding for MOR1 (microtubule organization 1) a protein essential for microtubule organization in *A. thaliana* (Whittington et al., 2001). In addition, the use of TS alleles was paramount to unravel genes involved in vesicle trafficking. In a genetic screen for mutants involved in stomatal development, Falbel *et al.* isolated a TS allele of *scd-1*, a gene involved in cytokinesis of stomata and in proper development of seedling, flower, leaf and trichomes. This study shows SCD1 is a soluble protein that contains an N-term DENN domain, which is characteristic of proteins that regulate vesicle trafficking. This evidence, together with TEM micrographs showing secretory vesicles accumulation in proximity to cell wall stubs, proved SCD1 regulates vesicle trafficking (Korasick et al., 2010). Interestingly, the TS allele *scd1-1* was also object of a study that uncover SCD1 role in plant immune response against bacteria (Korasick et al., 2010). Korasick *et al.* show SCD1 is required for flg22-elicited ROS production, seedling growth inhibition and pathogen related transcript accumulation (Korasick et al., 2010). A more recent study showed SCD1 and SCD2 are part of an oligomeric SCD complex essential for regulation of exocytosis in plants (Mayers et al., 2017). In fact, SCD1 colocalizes with members of the RabE1 family in vivo, and it binds to RabE1 in in vitro assays (Mayers et al., 2017). Furthermore, inhibition of EXO70 via Endosidin2 exacerbate the *scd-1* phenotype and overexpression of RabE1 rescues the *scd-1* TS phenotype at the restrictive temperature (Mayers et al., 2017). These results show SCD1 regulate post-Golgi secretory vesicle trafficking via the interaction with RabE1 and the exocyst complex (Mayers et al., 2017). As these examples show, the use of TS alleles in forward genetic screens facilitated important discoveries in a broad range of mechanisms in plants cell biology.

Chapter 2 Myosin XI drives polarized growth by vesicle clustering and local enrichment of F-actin in *Physcomitrium (Physcomitrella) patens*

The work presented in this chapter has been submitted for publication and it is currently under revision. The manuscript has been deposited to bioRxiv.

Galotto, G., Wisanpitayakorn, P., Bibeau, J. P., Liu, Y. C., Simpson, P. J., Tuzel, E., & Vidali, L. (2020). Myosin XI drives polarized growth by vesicle clustering and local enrichment of F-actin in *Physcomitrium (Physcomitrella) patens*. bioRxiv.

The research that led to this publication was a collaborative effort between members of the Vidali lab and the Tüzel lab at Worcester Polytechnic Institute. Luis Vidali, Giulia Galotto, Jeffrey P. Bibeau designed the research. Giulia Galotto, Jeffrey P. Bibeau, Pattipong Wisanpitayakorn, Yen-Chun Liu, Erkan Tüzel conducted experiments and analyzed the data. Parker J. Simpson collaborated in analyzing the data. Giulia Galotto, Jeffrey P. Bibeau, Pattipong Wisanpitayakorn, Erkan Tüzel interpreted the data. Giulia Galotto wrote the initial draft of the manuscript and Luis Vidali, Jeffrey P. Bibeau edited the draft. All authors reviewed and approved the final version of the manuscript.

2.1 Abstract

In tip-growing plant cells, growth results from myosin XI and F-actin mediated deposition of cell wall polysaccharides contained in secretory vesicles. Previous evidence showed that myosin XI anticipates F-actin accumulation at the cell's tip, suggesting a mechanism where vesicle clustering via myosin XI promotes F-actin polymerization. To evaluate this model, we used a conditional loss-of-function strategy by generating *Physcomitrium (Physcomitrella) patens* plants harboring a myosin XI temperature-sensitive allele. We found that loss of myosin XI function alters tip cell

morphology, vacuolar homeostasis, and cell viability, but this does not happen following F-actin depolymerization. Importantly, our conditional loss-of-function analysis shows that myosin XI clusters and directs vesicles at the tip of the cell, which induces F-actin polymerization, increasing F-actin's local concentration. Our findings support the role of myosin XI in vesicle clustering and F-actin organization, necessary for tip growth, and deepen our understanding of additional myosin XI functions.

2.2 Introduction

Myosin XI is an essential plant molecular motor involved in vesicular transport, organelle motility, and plant growth (Tominaga et al., 2003; Peremyslov et al., 2008; Madison et al., 2015; Abu-Abied et al., 2018). In tip growing cells, it is assumed myosin XI mediates growth via the active transport of secretory vesicles dependent on the F-actin cytoskeleton (Ojangu et al., 2007; Peremyslov et al., 2008; Vidali et al., 2010; Park and Nebenfuhr, 2013; Bibeau et al., 2020). This is the case for pollen tubes and root hairs in flowering and vascular plants and protonemal cells in bryophytes, which grow in a highly anisotropic fashion. In these cells, secretory vesicles containing cell wall polymers and wall loosening enzymes are delivered to the apex, where their secretion is locally regulated by Rac-Rop GTPases (Hepler et al., 2001; Kost, 2008; Rounds and Bezanilla, 2013; Le Bail et al., 2019). In the area of vesicle fusion, newly generated cell wall has enhanced extensibility; for the cell to expand without bursting and to reach fast growth rates (5.5 nm/sec in *Physcomitrium (Physcomitrella) patens* protonemata and 200-300 nm/sec in *Lilium longiflorum* pollen tubes), the growth mechanism needs to be tightly regulated. The motor myosin XI and the F-actin cytoskeleton are the main components of the growth machinery. In the past decades, an extensive amount of research has been performed to understand how myosin XI and F-actin interact to generate and maintain such an anisotropic growth fashion. Despite extensive research,

however, this phenomenon is not completely understood. Multiple lines of evidence suggest myosin XI is key to the development of proper cell polarization (Tominaga et al., 2000; Ojangu et al., 2007; Peremyslov et al., 2008; Peremyslov et al., 2010; Vidali et al., 2010; Cai et al., 2014). In land plants, such as *P. patens*, a knockdown approach showed myosin XI is essential for maintaining polarized growth (Vidali et al., 2010). In the vascular plant *Arabidopsis thaliana*, myosins XI (a class with 13 genes) is involved in the development of root hairs and trichome morphogenesis, as well as organelle trafficking (Ojangu et al., 2007; Peremyslov et al., 2008). Some reports show myosin XI is also important for F-actin organization, such is the case in epidermal *A. thaliana* cells (Peremyslov et al., 2010; Cai et al., 2014) and root hairs (Tominaga et al., 2000). The F-actin cytoskeleton, together with myosin XI, plays a crucial role in tip growth. In *L. longiflorum* pollen tubes, depolymerization of F-actin through latrunculin B, Cytochalasin D, and DNaseI, stops growth (Vidali et al., 2001; Finka et al., 2007). In *L. longiflorum* pollen tubes, F-actin polymerization is the limiting factor for pollen tube elongation, in a process independent from transport via cytoplasmic streaming (Vidali et al., 2001). Similarly to pollen tubes, the F-actin pharmacological inhibition in *P. patens* protonemata alters F-actin structures and stops the growth in a dose-dependent manner (Vidali et al., 2009a). Furthermore, in *P. patens*, an active transport that relies on F-actin is essential for tip growth: a mechanism based on vesicle diffusion alone cannot support growth (Bibeau et al., 2018).

Fluorescent cross correlation analyses of F-actin, myosin XI, and VAMP-labeled vesicles in *P. patens* characterized their temporal relation in protonemal cell tips (Furt et al., 2013). Surprisingly, while myosin XI and the VAMP-labeled vesicles are in phase, the myosin XI and the actin signal are not, with the myosin XI-vesicle signal leading the F-actin signal by 18.6 sec (Furt et al., 2013). This is surprising because a transport mechanism based on myosin XI motors walking on

preassembled F-actin would result in the F-actin signal leading or being temporally correlated with the myosin XI signal. Instead, the myosin XI-vesicle cluster leading the F-actin suggests a different cellular mechanism than the one provided by the simple F-actin track hypothesis.

In this work, we hypothesize myosin XI clusters vesicles enabling local F-actin polymerization, and that this mechanism is essential for the maintenance of apical growth. We tested our hypothesis by generating a temperature-sensitive (TS) allele of myosin XI and by combining it with the secretory vesicle marker 3mCherry-VAMP and the F-actin marker Lifeact-mEGFP. The generation of loss of function via TS alleles has been paramount to uncover the role of essential genes in plants, but have been historically limited to forward genetic screens (Lane et al., 2001; Whittington et al., 2001). Here, we generated a conditional myosin XI allele through rational mutagenesis. We used the plant *P. patens*, which is a great model to study polarized growth due to its simple cytology and tractable genetics (Reski, 2018; Rensing et al., 2020). Our results prove that myosin XI clusters secretory vesicles at the cell's apex and that myosin XI is essential for persistent apical growth. In addition, we show that myosin XI is necessary for the preservation of the elongated cell morphology and proper apical wall curvature, characteristic of tip growing cells. Finally, we also observed myosin XI is involved in vacuole homeostasis and cell viability.

2.3 Results

2.3.1 Development of a myosin XI temperature-sensitive allele

Myosin XI function is essential for tip growth (Vidali et al., 2010); hence, to be able to further characterize its function in polarized growth, we generated a moss line harboring a TS allele of myosin XI. To do so, we used a previously described strategy to generate temperature-sensitive alleles in plants (Vidali et al., 2009b). This strategy is based on mutagenizing residues in the core

of the protein of interest, which will render it less stable at higher temperatures, likely resulting in protein unfolding or denaturation (Vidali et al., 2009b). We selected potential buried residues to target by assigning a hydrophobicity score to each amino acid in the myosin XI protein sequence (Kyte and Doolittle, 1982); then, we identified the ones that confer temperature sensitivity to the plants (20°C vs. 32°C) via an RNAi-based complementation assay (Vidali et al., 2007) (see Methods). In the *P. patens* genome there are two myosin XI genes, myosin XIa and myosin XIb, which are 94% identical at the protein level. Here we decided to modify myosin XIa because it is expressed at higher levels (Vidali et al., 2010). We found that we needed to insert two point mutations in the myosin XIa gene: V584A, L616A to render the protein temperature-sensitive (Figure 2.1a,b and Methods). Due to the functional redundancy of the two myosin XI genes (Vidali et al., 2010), we coupled the site-directed mutagenesis with the deletion of myosin XIb (line referred to as myoXIaTS). As a control for the loss of myosin XIb, we generated a *P. patens* line maintaining the WT version of myosin XIa, but harboring the deletion of myosin XIb (line referred to as myoXIaWT). Both lines were generated in a parental line expressing Lifeact-mEGFP (Vidali et al., 2009a), which was also used as a control.

To confirm the effect of the myosin XIaTS protein on plant growth and morphology, we performed a morphometric assay (Galotto et al., 2019). After regeneration of protoplasts for four days, plants were exposed at 20°C and at 32°C for three days, then imaged. When plants are lacking myosin XIb but express the WT copy of myosin XIa, they do not exhibit morphological defects: they appear polarized and the plant area is comparable to the parental line (Figure 1c). On the other hand, plants expressing the TS allele of myosin XIa and lacking the functional copy of myosin XIb, exhibit strong temperature sensitivity at 32°C (Figure 2.1c). Mutant plants at 32°C do not have tip growing cells and are highly stunted (Figure 1c). Plant area and solidity were computed

to quantify the observed differences (Vidali et al., 2010; Galotto et al., 2019) (Figure 2.1d). The plant area is comparable in controls at the permissive temperature and it is significantly reduced in TS plants at the restrictive temperature. Solidity values are low in control plants at 32°C and are

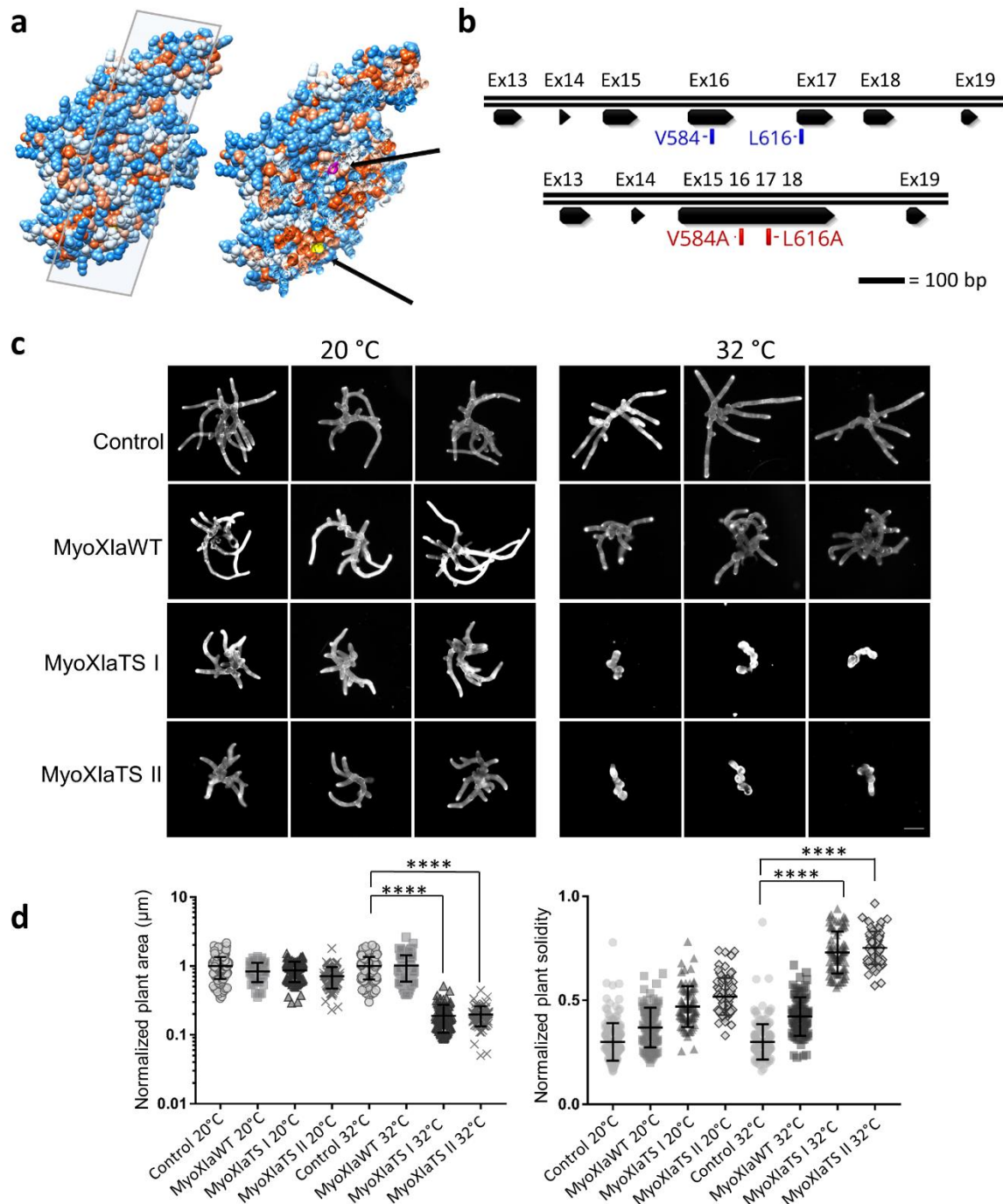


Figure 2.1 Two point mutations (V584A, L616A) renders myosin XI protein temperature sensitive. **a**, Myosin XIa motor domain modeled on the crystal structure of Myosin Vc from *Homo sapiens* with Swissmodel. The amino acid hydrophobicity was color coded on the Kyte-Doolittle scale, low hydrophobicity is depicted in blue, high in orange red. The surface of the domain was sliced to show the two point mutations buried in the hydrophobic core, Valine in yellow and Leucine in magenta (arrows). **b**, Myosin XIa TS and Myosin XIb KO. **c**, Representative images of 1-week old control and mutant plants grown at 20°C and 32°C. The plants labeled as “control” are the parental line control. In the panel, the cellulose is stained with calcofluor-white. Myosin XIa TS I and II represent two independent lines harboring the temperature sensitive allele. Scale bar = 50 µm. **d**, Quantification of normalized plant area and solidity of control and mutant plants at grown at 20°C and 32°C. Number of plants analyzed: control 20°C, 174. Control 32°C, 163. Myosin XIb KO 20°C, 96. Myosin XIb KO 32°C, 92. Myosin XIb KO Myosin XIa TS I 20°C, 76. Myosin XIb KO Myosin XIa TS I 32°C, 78. Myosin XIb KO Myosin XIa TS II 20°C, 80. Myosin XIb KO Myosin XIa TS II 32°C, 73. Error bar represent standard deviation of the mean. Comparison among groups performed via 2 way ANOVA ($P < 0.0001$).

closer to 1 in TS plants at 32°C, characteristic of round and unbranched plants, and consistent with previous RNAi results (Vidali et al., 2010). These data show that plants expressing the mutant (V584A, L616A) allele of myosin XIa and lacking a functional copy of myosin XIb are temperature sensitive at 32°C.

2.3.2. Myosin XI loss-of-function causes cell death while simultaneous F-actin depletion restores viability

During preliminary experiments aimed to characterize the myoXIaTS line, we observed that, when exposed at 32°C for 24 hrs, many cells in the plant appeared dead. To further investigate if prolonged lack of functional myosin XI leads to cell death, we incubated myoXIaWT and myoXIaTS cells at 20°C and 32°C for 24 hrs. Prior to imaging, plants were stained with calcofluor-white and propidium iodide, to mark the plant’s outline and the nucleus of dead cells, respectively. After 24 hrs of incubation at 32°C, a high number of myoXIaTS apical cells die, compared to the myoXIaWT plants at 32°C (Figure 2.2). In contrast, in the myoXIaWT cells exposed at 32°C only a few cells die, probably due to temperature stress.

Since myosin XI is a F-actin dependent motor, we decided to investigate whether, in a similar way to myosin XI loss-of-function, F-actin depolymerization affects cell survival at 32°C. To test this, we treated both cell lines at 20°C and 32°C with 20 μ M latrunculin B, which fully depolymerizes F-actin (Vidali et al., 2009a; Bibeau et al., 2020). Surprisingly, when myoXIaTS plants were exposed to 32°C and simultaneously treated with latrunculin B, cell viability was rescued (Figure 2). Consistent with this, in the latrunculin B treated myoXIaWT plants, only a very small number of cells died, either at 20°C or 32°C (Figure 2.2). These results show that the inactivation of myosin XI in cells in which the F-actin cytoskeleton is still present strongly affects cell survival and are consistent with the hypothesis that myosin XI is essential for F-actin organization in protonemata. To get insights into the molecular mechanism triggering the observed cell death, we performed

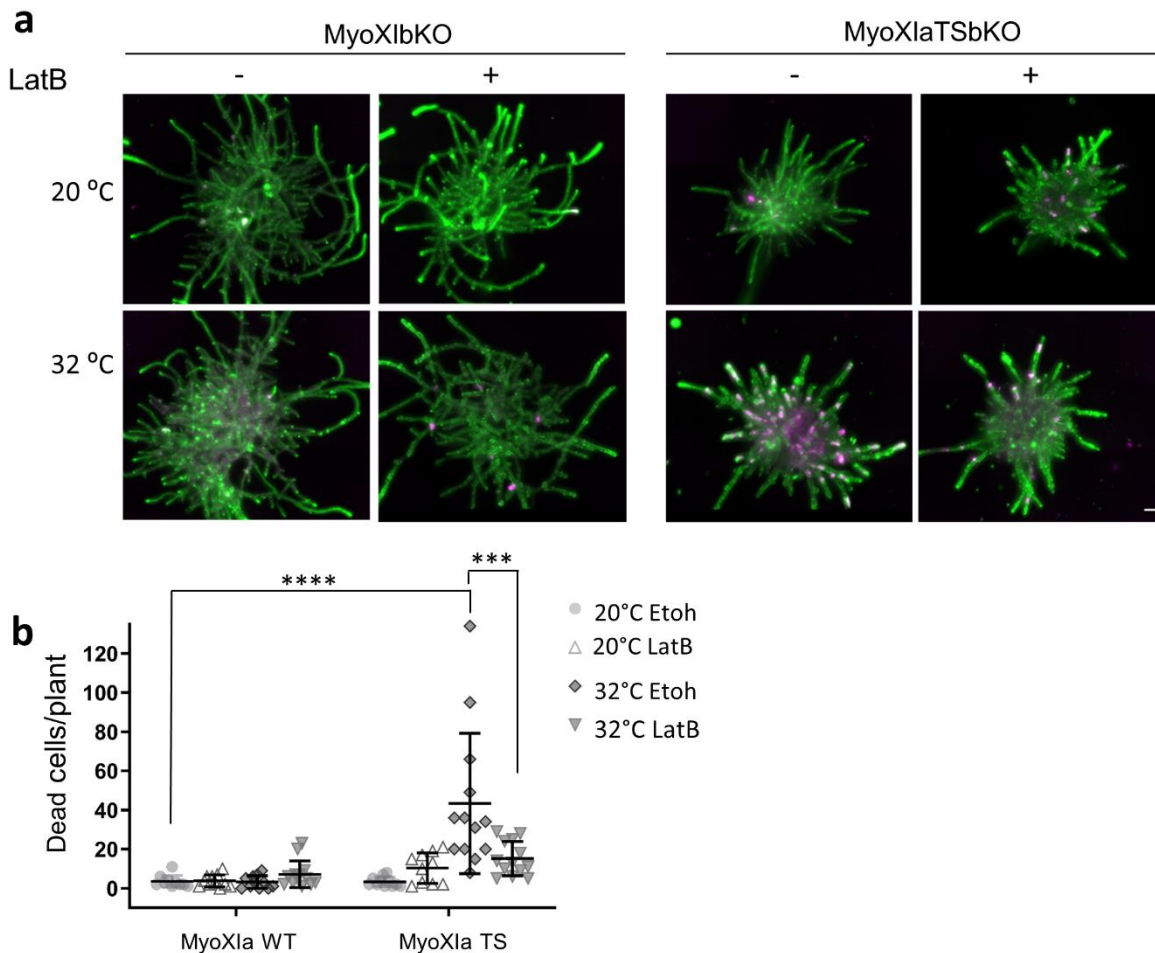


Figure 2.2 Myosin XI TS cells dye after 24 hrs exposure at 32°C, plants, depolymerization of F-actin via Latrunculin B reverts the phenotype. **a**, representative control and myosin XIa TS cells exposed at 32°C for 24 hrs, with Ethanol (vehicle control) or Latrunculin B (20 µM). In the panel, green represents calcofluor staining and magenta the dead cells stained with propidium iodide. **b**, quantification of number of dead cells per plant. Number of plants analyzed: control 20°C Etoh, 11. Control 20°C LatB, 11. Control 32°C Etoh, 11. Control 32°C LatB, 11. Myosin XIa TS 20°C Etoh, 11. Myosin XIa TS 20°C LatB, 11. Myosin XIa TS 32°C Etoh, 11. Myosin XIa TS 32°C LatB, 11. Differences between groups is computed via a 3 way ANOVA (P value < 0.0001). Error bars represents standard deviation from the mean. Scale bar = 100 µm.

preliminary RNASeq on control and myoXIaTS plants exposed at 32°C for 2 hours. Differential expression analysis of these preliminary results suggest that cell death is not due to activation of a program cell death pathway. Further experiments will be needed to verify if a program cell death pathway is activated at time points later than 2 hours.

2.3.3. In cells with decreased myosin XI activity, but not after F-actin depletion, the vacuole dilates and invades the cell tip

While observing myoXIaTS cells growing at 32°C, we noticed the expansion of the vacuole at the tip of the cell. Vacuoles are essential plant organelles involved in the preservation of cell homeostasis and the support of cytoplasmic turgor pressure, essential for cell shape establishment and maintenance (Marty, 1999). The vacuole in *P. patens* protonemal tip cells reflects the characteristic “zonation”, where an expanded section of the vacuole occupies the back of the cell, while a tubular anastomosing section of the vacuole populates the apical region of the cell (Oda et al., 2009; Furt et al., 2012). To investigate the dynamics of the observed vacuolar alterations in the myosin XI loss of function plants, we incubated myoXIaWT cells and myoXIaTS cells at 20°C and 32°C for 2 hours and we stained them with the tonoplast marker MDY-64 (Scheuring et al., 2015) (Figure 3). Control cells exhibit, as expected (both at 20°C and 32°C), a high number of anastomosing sections of the vacuole, especially in the region between the nucleus and the sub-

apex (Figure 2.3). However, in the myoXIaTS cells incubated at 32°C for 2 hours, we observed the disappearance of the anastomosing sections, and instead, the vacuole enlarges and invades the tip (Figure 2.3). As performed in the previous experiment (Figure 2.2), we further investigated whether depolymerization of F-actin by latrunculin B (20 μM) would mimic the myoXIaTS vacuolar phenotype. To our surprise, F-actin depolymerization did not phenocopy the

TS phenotype, but instead, the MyoXIaTS cells at 32°C and treated with latrunculin B present a highly anastomosed vacuole, similar to controls. These results indicate that myosin XI function is

important for vacuolar homeostasis and structure. Interestingly, these results are similar to the results from the cell death assay, in that when F-actin is depleted, the lack of myosin XI has reduced effect on the cells. Together, these results are consistent with the hypothesis that myosin XI participates in F-actin organization during growth.

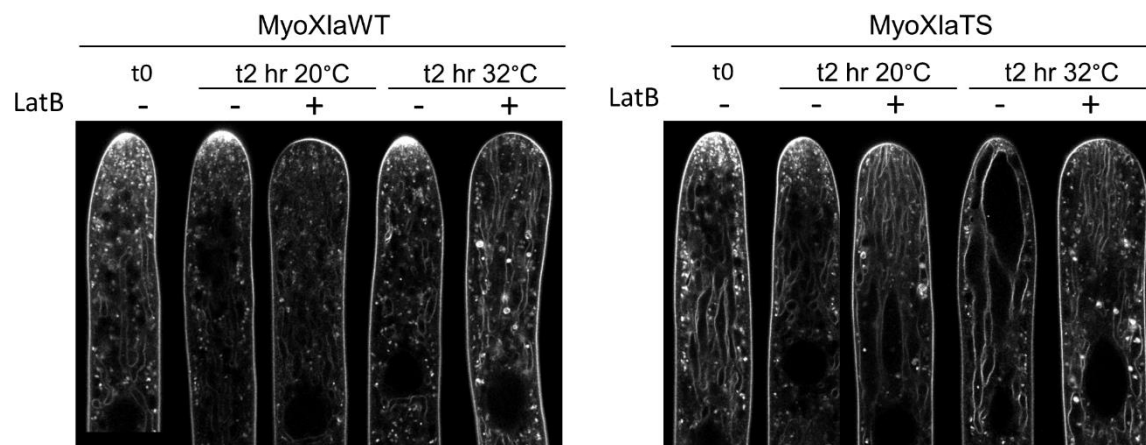


Figure 2.3 Myosin XIa TS cells present an enlarged aberrant vacuole, depolymerization of F-actin via Latrunculin B reverts the phenotype. Representative control and myosin XIa TS cells exposed at 32°C for 2 hrs, with Ethanol (vehicle control) or Latrunculin B (20 μM). The tonoplast is stained with MDY64 (500 nM) Note that the dye also stains the plasma membrane and membranous organelle within the cell. For display purposes the images were γ -adjusted (0.8%). Scale bar = 10 μm.

2.3.4 Tip growing cells deprived of functional myosin XI exhibit lateral swelling and drastically reduced growth rate

Functional myosin XI is required for proper tip growth (Ojangu et al., 2007; Peremyslov et al., 2008; Vidali et al., 2010; Park and Nebenfuhr, 2013; Madison et al., 2015) and fluctuation cross-correlation analysis and *in vivo* imaging showed that VAMP-labeled vesicles are a myosin XI cargo (Furt et al., 2013; Bibeau et al., 2020). Nevertheless, the essential mechanism behind myosin XI's function in polarized cell growth remains to be defined. By exploiting the proper polarized development of myoXIaTS plants at 20°C, we investigated how growth is affected at the single-cell level by the sudden loss of function of myosin XI, upon switching the temperature to 32°C. MyoXIaWT and myoXIaTS grown at 20°C were transferred into an enclosed microscope pre-heated at 32°C and imaged for 5 hours (Movie S1 and MovieS2). The myoXIaTS cells, after exposure to 32°C, exhibit morphological defects as well as growth defects (Figure 2.4a). To quantify changes in the growth rate between the two lines, we performed a kymograph analysis (Figure 2.4b,c). MyoXIaTS cells have a drastically reduced growth rate compared to the control. We measured an average growth rate of 8.86 ± 1.04 nm/sec in the myoXIaWT and an approximate ten-fold reduction in growth, to 0.79 ± 0.19 nm/sec, in the myoXIaTS. Visually, the overall morphology of the myoXIaWT cells exposed to 32°C did not change considerably (Figure 2.4a). The diameter of MyoXIaWT cells only increases modestly, from 17.71 ± 0.54 μ m (SEM) prior to the incubation, to 19.19 ± 0.6 μ m after 5 hours at 32°C, but this change is not significant (Figure 4d). On the other hand, myoXIaTS cells grown at 32°C for 5 hours exhibit considerable lateral swelling in the sub-apex of the cell (Figure 2.4a,d). The average cell diameter in myoXIaTS cells increases from 18.72 ± 0.56 μ m prior to the incubation, to 23.02 ± 1.17 μ m after 5 hr at 32°C, and this change is statistically significant (adjusted $P < 0.01$). These observations confirm that myosin

XI is critical for polarized growth, and the observed lateral swelling suggests depolarized secretion or alterations in cell wall mechanical properties or both.

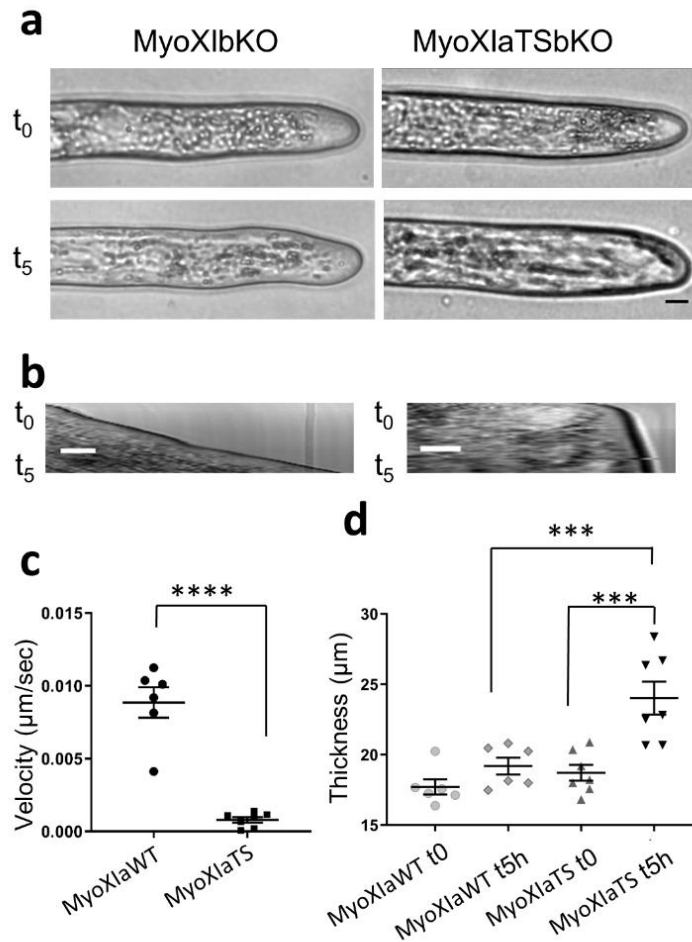


Figure 2.4 Time lapse of control and myosin XI TS cells at 32°C show growth and morphology defects of myosin deficient cells **a**. Representative control and myosin XIaTS cell imaged with epifluorescence microscope enclosed in temperature controlled chamber. Cells are imaged for 5 hrs at 32°C. Scale bar = 20 µm. **b**. Representative kymographs depicting cell growth. Scale bar = 10 µm. **c**. Velocity (µm/sec) of control and myosin XIaTS the cell as quantified from kymographs. Number of cells analyzed: control cells, 6. Myosin XIaTS cells, 7 cells. Difference tested via parametric T test (P value < 0.0001), error bars represent SEM. **d**. Thickness of control and myosin XIa TS cells 50 µm from the cell tip. Number of cells analyzed: control cells, 6. Myosin XIaTS cells, 7 cells. Difference tested via 2 way ANOVA (P value = 0.0001), error bars represent SEM.

2.3.5 Myosin XIa TS cells exposed at 32°C display higher cell tip curvature and diameter than F-actin depleted cells

To get insights into the individual function of myosin XI and F-actin in maintaining proper cell shape, we investigated how their loss-of-function affects cell morphology. To do so, we performed a time-course fluorescent study (1.5 hrs, 3 hrs, 5 hrs, 8 hrs) in which we treated plants with latrunculin B (20 μM) to depolymerize F-actin or exposed them at 32°C to reduce functional myosin XI. To elucidate myosin XI and F-actin interplay, we then compared the individual myosin XI and the F-actin loss of function phenotypes, with the phenotype of cells deprived simultaneously of both, F-actin and myosin XI. Preliminary analysis showed that, while a phenotype could not be detected at 1.5 hrs, morphological changes manifested at 3 hrs and became more pronounced at 5 hrs and 8 hrs. For this reason, we focused our analysis on the 5 hrs and 8 hrs time points. When plants lack F-actin, the cell tip appears rounder compared to the wild type, predominantly after 5 hrs and 8 hrs of treatment (Figure 2.5a). Decreased functional myosin XI results in considerable sub-apical swelling and a more narrow tip (Figure 2.5a), consistent with very slow elongation (Figure 2.4b).

To quantify the observed difference in tip shape, we measured the curvature of the cell at the tip in both caulonemal cells (Figure 2.5c) and chloronemal cells (Supplemental figure 1c). Following 5 hrs of treatment, the myoXIaTS caulonemal cells at 32°C have higher curvature values than the myoXIaTS cells at 20°C and the myoXIaWT at both temperatures (Figure 2.5a). In the myoXIaTS, the average tip curvature is $0.16 \mu\text{m}^{-1} \pm 0.004 \mu\text{m}^{-1}$ (SEM) when caulonemal cells are grown at 20°C, and it increases to $0.19 \mu\text{m}^{-1} \pm 0.006 \mu\text{m}^{-1}$ after 5 hrs of exposure at 32°C (Figure 5c, adjusted $P < 0.01$). This curvature difference was only transitory because, after 8 hrs at 32°C, the tip curvature of myoXIaTS cells decreases to $0.18 \mu\text{m}^{-1} \pm 0.006 \mu\text{m}^{-1}$, likely due to the local

bulging at the very tip of the cell. MyoXIaTS caulonemal cells treated with latrunculin B for 5 hrs have curvature values of $0.12 \mu\text{m}^{-1} \pm 0.003 \mu\text{m}^{-1}$ both at 20°C and 32°C (Figure 2.5c). This value is lower than the same cells with unaltered F-actin levels, and the same effect is observed in myoXIaWT cells treated with latrunculin B (Figure 2.5c). This decrease in curvature is likely the result of a defect in the proper maintenance of anisotropic growth, which causes the rounding of the tip. Similar, but less dramatic effects were observed in chloronemata cells (Supplemental figure 1c).

We also quantified the changes of curvature in the shank, which were visible in the myoXIaTS cells at the restrictive temperature (Figure 2.5d and Figure 2.6). In these cells, the average curvature on the right side of the shank (similar results were observed on the left side) is $0.014 \mu\text{m}^{-1} \pm 0.001 \mu\text{m}^{-1}$ after 5hrs and $0.016 \mu\text{m}^{-1} \pm 0.002 \mu\text{m}^{-1}$ after 8hrs (Figure 2.5d, adjusted $P < 0.01$). On the other hand, in myoXIaTS cells at 20°C and myoXIaWT cells at both temperatures, the shank does maintain a straight morphology (~ zero curvature). Depolymerization of F-actin by latrunculin B treatment in both TS and WT cells does no result in an increase of lateral curvature at any temperature, suggesting that F-actin is necessary for the myosin XI loss-of-function phenotypes observed. Again, similar, but less dramatic effects were observed in chloronemata cells (Figure 2.6d).

This assay also allowed us to confirm the increase in cell thickness following myosin XI loss-of-function (Figure 2.4a,d). In myoXIaTS caulonema cells, cell thickness increases from $19.45 \mu\text{m} \pm 0.34 \mu\text{m}^{-1}$ at 20°C, to $23.66 \mu\text{m} \pm 0.26 \mu\text{m}^{-1}$ at after 5 hrs at 32°C, and to $25.33 \mu\text{m} \pm 0.520 \mu\text{m}^{-1}$ after 8 hrs at 32°C (Figure 2.5e, adjusted $P < 0.01$), while the myoXIaWT cells do not exhibit a significant diameter change from 20°C to 32°C (Figure 2.5e). Only a modest change in thickness was observed after latrunculin B treatment at high temperature, but the magnitude of the changes

was smaller than that produced by reducing myosin XI function in the presence of F-actin. Together, our results show that myosin XI and F-actin play separable and sometimes complementary roles in cell growth and morphogenesis.

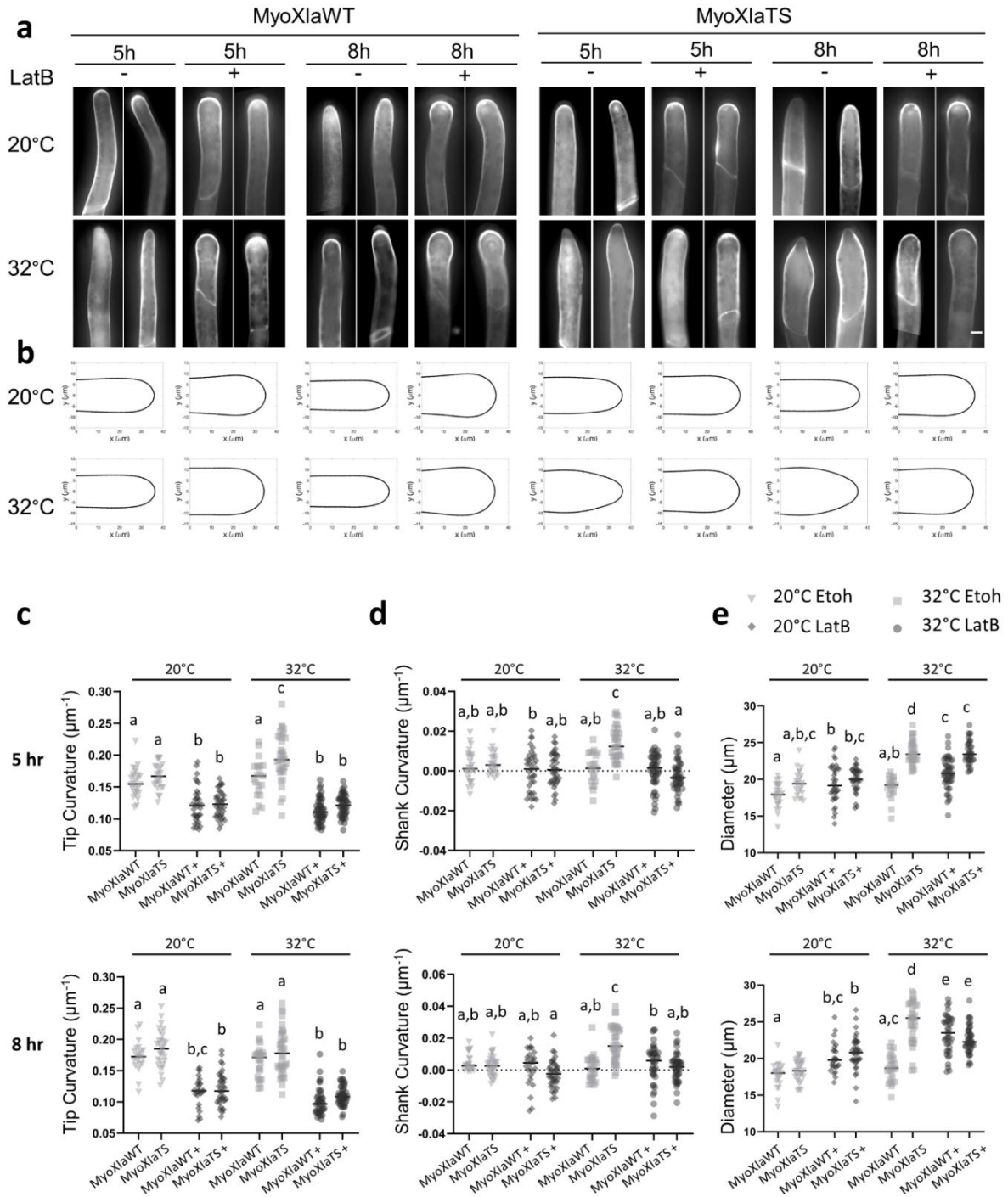


Figure 2.5 Lack of functional myosin or F-actin affects caulonemata tip morphology differently a, 2 representative caulonemata myoXIaWT and myoXIaTS cells grown at 20° C and 32° C with Ethanol (vehicle control) or Latrunculin B (20 μM) before treatment (t0) and for 5 and 8 hours. In the panel, the cellulose is stained with calcofluor-white. Scale bar = 10 μm. b, regeneration of cell contour from computed curvature values. Number of cells used to regenerate each contour: 5 hours, myoXIaWT EtOH 20°C, 26. myoXIaWT EtOH 32°C, 21. myoXIaWT LatB 20°C, 36. myoXIaWT LatB 32°C, 47. myoXIaTS EtOH 20°C, 24. myoXIaTS EtOH 32°C, 35. myoXIaTS LatB 20°C, 38. myoXIaTS LatB 32°C, 45; 8 hours, myoXIaWT EtOH 20°C, 21. myoXIaWT LatB 20°C, 26. myoXIaWT LatB 32°C, 39. myoXIaTS EtOH 20°C, 30. myoXIaTS EtOH 32°C, 38. myoXIaTS LatB 20°C, 39. myoXIaTS LatB 32°C, 43. c, average curvature ($1/\mu$) of the cell tip after 5 hrs (top) 8 hrs (bottom). The tip was set at 0 μm, and the curvature between -3 μm to +3 μm from the tip was averaged. d, average curvature ($1/\mu$) of a region on the right side of the cell shank after 5 hrs (top) 8 hrs (bottom). The curvature between 25 μm to 35 μm from the tip was averaged. e, Diameter of the cell computed at the widest point after 5 hrs (top) 8 hrs (bottom). Number of cells used for c,d,e at 5 hrs: myoXIaWT EtOH 20C, 26. myoXIaWT EtOH 32C, 21. myoXIaWT LatB 20C, 36. myoXIaWT LatB 32C, 47. myoXIaTS EtOH 20C, 24. myoXIaTS EtOH 32C, 35. myoXIaTS LatB 20C, 38. myoXIaTS LatB 32C, 45. Number of cells used for c,d,e at 8 hrs: myoXIaWT EtOH 20C, 21. myoXIaWT EtOH 32C, 26. myoXIaWT LatB 20C, 26. myoXIaWT LatB 32C, 39. myoXIaTS EtOH 20C, 30. myoXIaTS EtOH 32C, 38. myoXIaTS LatB 20C, 39. myoXIaTS LatB 32C, 43. Bars that do not share similar letters denote statistical significance, adjusted $P < 0.05$ three-way ANOVA. All values are means \pm SEM.

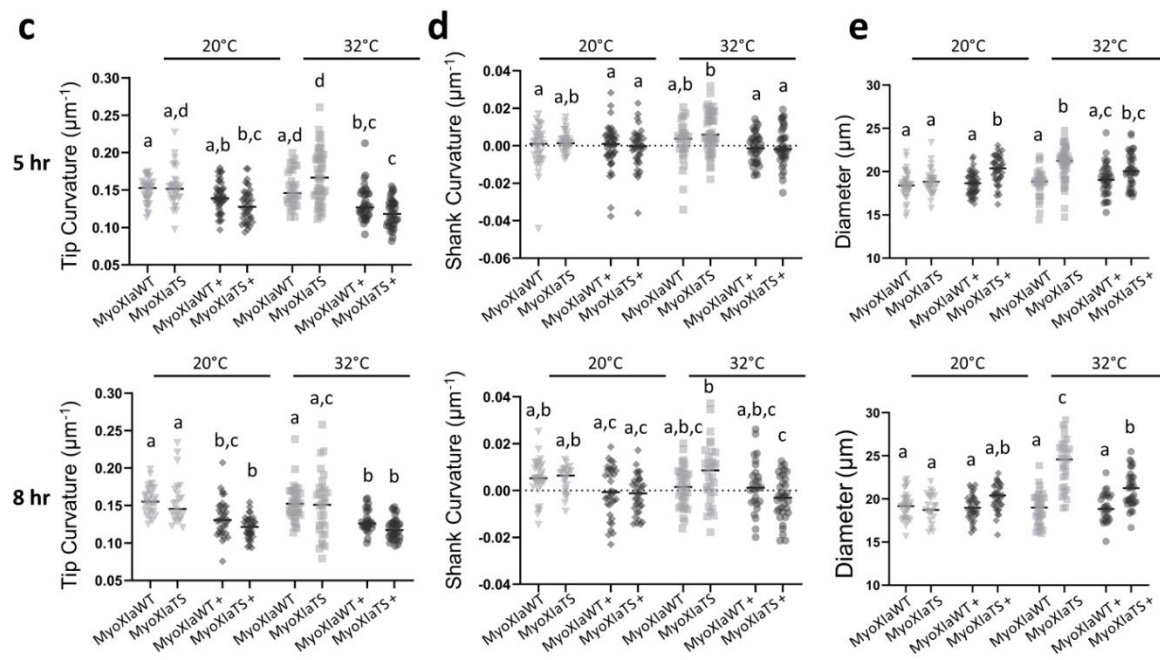
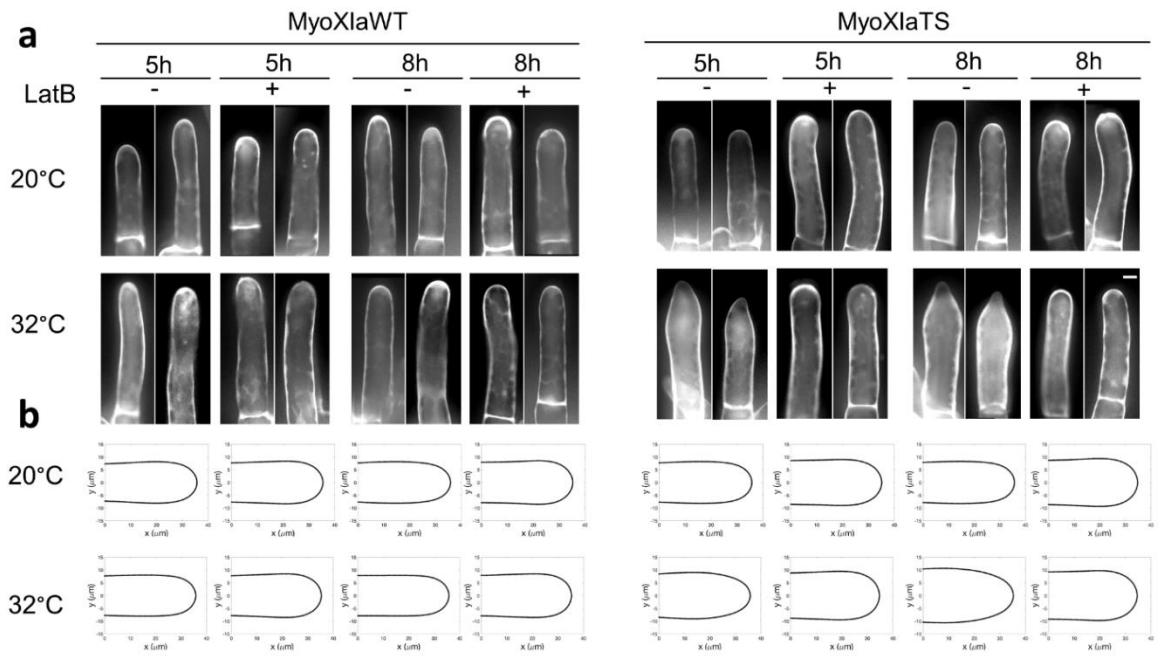


Figure 2.6 Lack of functional myosin or F-actin affects chloronemata tip morphology differently . a. Two representative chloronemata myoXIaWT and myoXIaTS cells grown at 20° C and 32° C with Ethanol (vehicle control) or Latrunculin B (20 μM) before treatment (t0) and for 5 and 8 hours. In the panel, the cellulose is stained with calcofluor-white. Scale bar = 10 μm. b. Regeneration of cell contour from computed curvature values. Number of cells used to regenerate each contour: 5 hours, myoXIaWT EtOH 20C, 36. myoXIaWT EtOH 32C, 30. myoXIaWT LatB 20C, 47. myoXIaWT LatB 32C, 37. myoXIaTS EtOH 20C, 31. myoXIaTS EtOH 32C, 47. myoXIaTS LatB 20C, 41. myoXIaTS LatB 32C; 8 hours, myoXIaWT EtOH 20C, 31. myoXIaWT EtOH 32C, 34. myoXIaWT LatB 20C, 35. myoXIaWT LatB 32C, 27. myoXIaTS EtOH 20C, 23. myoXIaTS EtOH 32C, 31. myoXIaTS LatB 20C, 35. myoXIaTS LatB 32C, 35. c. Average curvature ($1/\mu$) of the cell tip after 5 hrs (top) 8 hrs (bottom). The tip was set at 0μm, and the curvature between -3 μm to +3 μm from the tip was averaged. d. Average curvature ($1/\mu$) of a region on the right side of the cell shank after 5 hrs (top) 8 hrs (bottom). The curvature between 25 μm to 35 μm from the tip was averaged. e. Diameter of the cell computed at the widest point after 5 hrs (top) 8 hrs (bottom). Number of cells used for c,d,e, at 5 hrs: myoXIaWT EtOH 20C, 36. myoXIaWT EtOH 32C, 30. myoXIaWT LatB 20C, 47. myoXIaWT LatB 32C, 37. myoXIaTS EtOH 20C, 31. myoXIaTS EtOH 32C, 47. myoXIaTS LatB 20C, 41. myoXIaTS LatB 32C, 38. Number of cells used for c,d,e, at 8 hrs: myoXIaWT EtOH 20C, 31. myoXIaWT EtOH 32C, 34. myoXIaWT LatB 20C, 35. myoXIaWT LatB 32C, 27. myoXIaTS EtOH 20C, 23. myoXIaTS EtOH 32C, 31. myoXIaTS LatB 20C, 35. myoXIaTS LatB 32C, 35. Bars that do not share similar letters denote statistical significance, adjusted $P < 0.05$ three-way ANOVA. All values are means \pm SEM.

2.3.6 Lack of functional myosin XI dissipates tip-localized VAMP-labeled vesicles and F-actin within minutes

P. patens apical cells exhibit an enrichment of myosin XI and F-actin at the apex, which is both essential for tip growth and only present in cells that are actively growing (Vidali et al., 2009a; Vidali et al., 2010). Similarly, a population of VAMP-labeled vesicles populates the tip (Furt et al., 2013; Bibeau et al., 2018; Bibeau et al., 2020), while myosin XI and VAMP-labeled vesicles accumulation leads the F-actin's accumulation by 18.6 sec at the tip of the cell (Furt et al., 2013). This prompted us to hypothesize that myosin XI functions by clustering vesicles at the cell's tip, and that this clustering is important for F-actin organization and vesicle accumulation, both necessary for growth (Furt et al., 2013; Bibeau et al., 2018). To evaluate this hypothesis and to investigate the cause for the drastic reduction in the observed growth rate of myoXIaTS cells at 32°C, we explored the dependence of the apical localization of VAMP-labeled vesicles and F-actin on functional myosin XI. To do this, we transformed the myoXIaWT and myoXIaTS lines with

the vesicle marker 3xmCherry-VAMP72A1 (referred to as myoXIaWT-VAMP and myoXIaTS-VAMP lines); these lines also express the F-actin probe, Lifeact-mEGFP (Vidali et al., 2009a). As expected, at 20°C and 32°C, myoXIaWT cells exhibit the characteristic VAMP-labeled vesicle and F-actin accumulations at the cell tip (Figure 2.7). However, in the myoXIaTS cells exposed 32°C for only 20 minutes, the vesicle cluster dissipates and concomitantly the F-actin spot disappears. These results are consistent with myosin XI functioning in the clustering of vesicles at the cell tip, and with this clustering being important to maintaining F-actin organization and polarized secretion needed for tip growth.

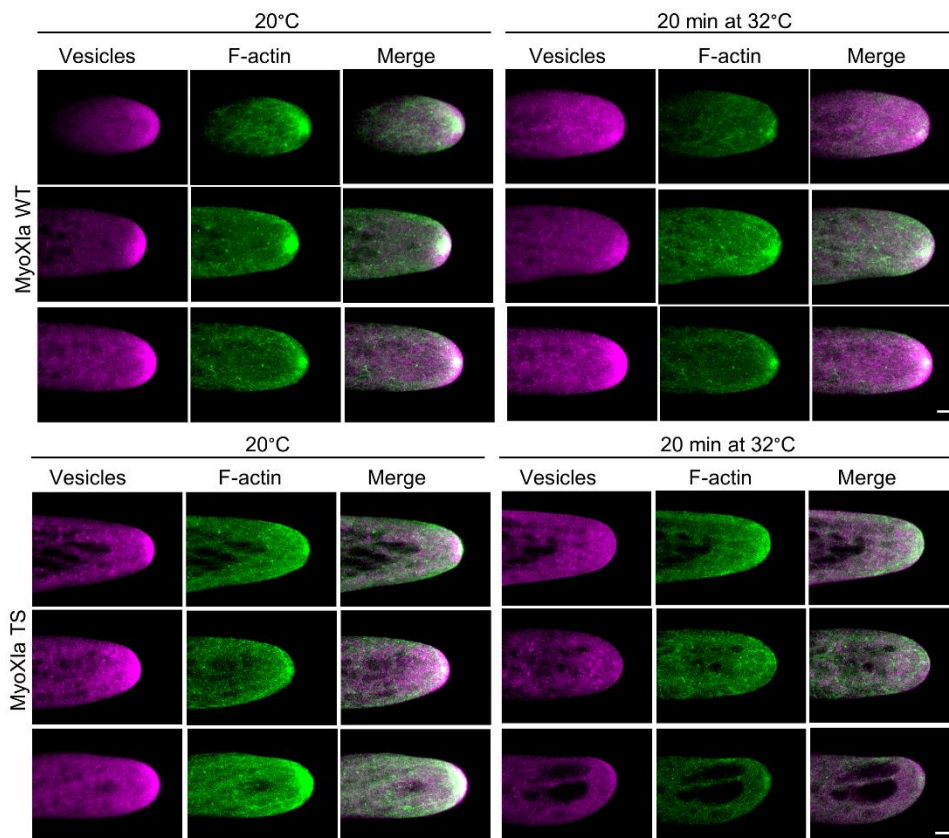


Figure 2.7 F-actin spot and tip oriented vesicle cluster dissipate upon 20 minutes exposure at 30°C **a**, myosin XIbKO 3xmCherry-VAMP71A1 and myosinXIa TS 3xmCherry-VAMP72A1 imaged while exposed at 20 °C and 32 °C. In the panel, green represents LifeAct-GFP labelled F-actin and magenta the 3xmCherry-VAMP72A1 secretory vesicles. MyoXIaTSbKO cells exposed at 32 °C for 20 minutes fail to exhibit vesicle clustering at cell tip and F-actin spot. For display purposes the images were enhanced by contrast normalization (0% saturation), gaussian blur (0.6%) and manual adjustment of brightness and contrast levels. Scale bar 5 µm.

2.3.7. Myosin XI is essential for the formation of latrunculin B-induced vesicle clusters

In previous work, Furt et al. observed that upon treatment with very low concentrations of latrunculin B, myosin XI clusters followed by F-actin polymerization arise in ectopic sites at the cell's shank, recapitulating myosin XI and F-actin correlation observed at the growing tip (Furt et al., 2013). Based on these published observations, and on our aforementioned fluorescent results (Figure 2.7), we hypothesize these ectopic clusters are the result of myosin XI's role in clustering vesicles and that this clustering results in F-actin local polymerization, and subsequent actin-polymerization dependent vesicle motility. To test our hypothesis, we used the myoXIaWT-VAMP and myoXIaTS-VAMP lines and attempted to reproduce the previously observed myosin XI and F-actin ectopic clusters upon latrunculin B treatment (Furt et al., 2013), both at the permissive and restrictive temperature. Importantly, the use of a myosin XI temperature-sensitive allele allowed us to test if myosin XI is necessary for the observed ectopic vesicle clustering.

When treating the myoXIaWT-VAMP and myoXIaTS-VAMP with latrunculin B (0.25 µM) at 20°C, we observed, in multiple locations in the cell, an enrichment of vesicle-clusters followed by F-actin polymerization (Figure 2.8). When F-actin is polymerized, the VAMP-labelled vesicles clusters become motile and propel in the cell, consistent with an F-actin polymerization dependent motility. When we treated myoXIaTS-VAMP cells with latrunculin B (0.25 µM) and exposed them at 32°C, the VAMP-labeled vesicle clusters fail to form. Importantly, the control

Figure 2.8 Latrunculin B induced motile secretory vesicles clusters followed by F-actin cables are myosin XI dependent. **a**, representative myosin XIbKO 3xmCherry-VAMP71A1 and myosin XIa TS 3xmCherry-VAMP72A1 cells treated with 0.25 μ M LatB and imaged while exposed at 20 °C and 32 °C. In the panel, green represents LifeAct-GFP labelled F-actin and magenta the 3xmCherry-VAMP72A1 secretory vesicles. MyoXIaTSbKO cells exposed at 32 °C fail to exhibit vesicle clustering. For display purposes the images were enhanced by γ -adjustment (1.3%), gaussian blur (0.5%) and manual adjustment of brightness and contrast levels. **b**, quantification of cells exhibiting or not exhibiting vesicle clusters followed by F-actin cables at 20 °C and 32 °C. Number of cells analyzed: control 20 °C, 14. Control 32 °C, 15. TS 20 °C, 15. TS 32 °C, 15. The difference in the numbers of observed vesicle clusters is not significant between the two cell lines at 20°C. The difference in numbers of observed vesicle clusters is highly significant between the two cell lines at 32°C (Fisher's exact test, two-tailed P value <0.0001). Scale bar 10 μ m.

2.4 Discussion

Here we have revealed essential functions of myosin XI in plant cells. We showed that myosin XI is critical for polarized growth via its vesicle clustering activity, which induces actin polymerization. We also showed that this myosin is important to maintain cell morphology, vacuole structure, and cell survival. These conclusions are supported by experimental evidence obtained using a temperature-sensitive allele of myosin XI that we generated. The conclusion that myosin XI participates in vesicle clustering, and that this clustering is important for actin polymerization, is consistent with the hypothesis that vesicle clustering plays an essential role in protonemal tip growth. It will be interesting to investigate if a similar vesicle-clustering function and vesicle-mediated actin polymerization process exist in other plant tip growing cells. The use of a myosin XI TS allele provided an exceptionally advantageous tool to overcome growth limitations resulting from transient RNAi (Vidali et al., 2010). Using this tool, we were able to analyze phenotypes of differentiated cells, specifically caulonemata, that do not develop in plants undergoing RNAi of myosin XI.

In line with the hypothesis, we showed myosin XI is essential for vesicle clustering and F-actin accumulation at the cell tip. This result provides new insight into the relationship between myosin XI, vesicles, and F-actin in maintaining persistent polarized growth in plants. Our data indicate that myosin XI is the driver of a long-range F-actin polymerization-driven vesicular transport system, in which myosin XI binds secretory vesicles that carry an F-actin nucleator, such as class II formins (Vidali et al., 2009c) or the ARP2/3 complex (Perroud and Quatrano, 2006) or both. Subsequent polymerization of F-actin serves as a binding route for more motors, in a myosin XI-driven feedback that locally increases F-actin. A similar vesicular transport has been described in mice oocytes (Schuh, 2011), and vesicle clustering and actin-based propulsion have been previously observed in other plants; for instance, in *A. thaliana* pollen tubes, vesicle clusters propelled by formin-generated F-actin is essential for germination (Liu et al., 2018). However, inhibition of myosin-F-actin interaction via BDM suggested the mechanism observed by Liu et al. is myosin XI-independent (Liu et al., 2018), indicating that a fundamental difference may exist in the vesicle clustering and transport between the moss *P. patens* protonemata and the pollen of the vascular plant *A. thaliana*. Our data fit with existing evidence in *P. patens*, in which motile structures propelled by F-actin originating from formin II clusters have been described (van Gisbergen et al., 2012; Wu and Bezanilla, 2018). In addition, in support of our model, formin II localizes at the apex of tip growing cells and it is essential for polarized growth (Vidali et al., 2009c).

Our study demonstrates a link between myosin XI function and polarized cell's growth-rate and morphology. Myosin XI depleted cells exhibit a highly reduced growth rate, consistent with diffusion-based growth (Bibeau et al., 2018), and a simultaneous increase in cell thickness. The reduced growth-rate could be due to a small amount of myosin XI retaining its function.

Furthermore, our results show that depletion of myosin XI results in pointier cells with higher tip curvature and F-actin depleted cells result in blunter cells with lower tip curvature values. These results directly relate a molecular motor and the cytoskeleton to cell shape and provide us with a powerful tool to further study the regulation of cell morphology. Mathematical modeling of tip growing cells identified scaling laws that connect cell wall geometry to internal parameters (Campàs and Mahadevan, 2009; Campas et al.). Specifically, Campas et al. described a scaling law that relates the cell radius and the apical radius of curvature to the size of the vesicle secretion area (Campas et al., 2012). According to Campas et al., in blunt cells, the cell radius is proportional to the radius of curvature at the tip, and this implies that the secretion area scales with cell size, hence, it increases with an increase of cell size. On the other hand, in pointy cells, the radius of tip curvature is constant and independent of the cell's radius, and this implies the secretion area is constant (Campas et al., 2012). Integrating this with our data, we speculate that in myosin XI TS cells, secretion is highly reduced, but confined to a constant area in the cell's apex (Bibeau et al., 2018), resulting in a highly reduced growth rate, very thin cell diameter and a high tip curvature. On the other hand, in F-actin depleted cells, vesicles are passively transported via diffusion. Untargeted vesicle diffusion results in docking in a broader area at the tip, causing growth arrest and lateral growth and increase of cell thickness.

Alongside with deepening our understanding of myosin XI function in cell growth, we showed myosin XI is important for vacuole structure and cell viability. Furthermore, our data indicate depolymerization of F-actin attenuates the myosin XI-dependent cytological aberrations, opening new lines of investigation for the myosin XI-F-actin system in tip growing plant cells. The evidence that the F-actin myosin system could regulate vacuole structure in *P. patens* is inconsistent with previous reports. In fact, Oda et al. showed that microtubules are responsible for

vacuole structure regulation in *P. patens* (Oda et al., 2009). However, the investigation of Oda et al. is limited to chloronemata and ryzhoid cells, while our focus is on caulonemata cells. Caulonemata exhibit a lower density of organelles, especially chloroplasts, and have a higher growth rate than chloronemata (Furt et al., 2012), and this could result in a different vacuolar regulation system. Despite differences with previous reports in *P. patens*, our observations are common to the flowering plants *A. thaliana* and *N. tabacum*, in which the F-actin cytoskeleton is responsible to regulate vacuolar structure (Higaki et al., 2006; Scheuring et al., 2016). Furthermore, an F-actin-myosin V system regulates vacuole inheritance in *S. cerevisiae* (Tang et al., 2003). Further experiments are needed to broaden our understanding of myosin XI-F-actin involvement in vacuole regulation in plants. Identification of myosin XI interactors on the tonoplast membrane could confirm myosin XI direct role in vacuole transport in the cell. The heavy misregulation of the vacuole after 24 hrs of myosin XI depletion could be one of the causes of loss of cell viability. The lack of myosin XI has been previously related to premature cell senescence and cell death in *A. thaliana* (Ojangu et al., 2018). In discordance with our results, previous studies link F-actin depolymerization with cell death. In fact, in *A. thaliana*, latrunculin B induced F-actin depolymerization causes programmed cell death in pollen tubes (Thomas et al., 2006). Furthermore, Ojangu et al. show disruption of F-actin via latrunculin B results in increased transcriptional levels of stress-related genes (Ojangu et al., 2018). In the yeast *S. cerevisiae*, decreased F-actin dynamics result in cell death while the increase in F-actin dynamics increases in lifespan by 65% (Gourlay et al., 2004). Further research is needed to clarify why the depolymerization of F-actin rescues cell viability in *P. patens*. This study demonstrates a novel role for myosin XI in vesicle clustering and finds an association between myosin XI function with the maintenance of vacuole structure and cell viability.

2.5 Material and Methods

2.5.1. Generation of a *P. patens* myosin XI temperature-sensitive allele and a myosin XIb KO line

To identify residues that render myosin XI temperature-sensitive, we first introduced single mutations in the hydrophobic core of the myosin XI motor domain via PCR site-directed mutagenesis (Vidali et al., 2009b). Three different hydrophobic residues (L79, V584, L616) were initially mutagenized and three different constructs were tested. The mutagenesis was performed on the entry clone pENT-MyoXIaCDS harboring the ORF of the myosinXIa cDNA (Vidali et al., 2010). Three PCR reactions were performed using a forward mutagenic primer and the reverse primer M13 in the three following primer combinations: MyoXIA-L616A-F and M13R, MyoXIA-V584A-F and M13R, MyoXIA-L79A-F, M13R (see Table 2.1). Three additional PCR reactions were performed using a reverse (non-mutagenic) primer and the forward primer M13 in the three following combinations: MyoXIA-L616A-R and M13F, MyoXIA-V584A-R and M13F, MyoXIA-L79A-R, M13F. The PCR fragments and pENT-MyoXIaCDS were digested with NotI and AscI and ligated together, generating three different constructs: pENTMyoXIaL79A, pENTMyoXIaV584A, pENTMyoXIaL616A. The ligated constructs were verified by sequencing. An LR Gateway reaction was used to transfer the pENTMyoXIaL79A, pENTMyoXIaV584A, and pENTMyoXIaL616A to the expression vector pTHUbiGate and generated three expression clones. The expression clones were co-transformed in moss with an RNAi construct targeting both myosin XIa and XIb from their 5'UTRs (Vidali et al., 2010) and their ability to complement at 20-25°C and plant temperature sensitivity at 32°C was tested.

The constructs harboring MyoXIaV584A and MyoXIaL616A complemented at 25°C and showed mild temperature sensitivity at 32°C. The pENTMyoXIaL79A construct did not show any temperature sensitivity and was not pursued any further. To obtain a stronger temperature

sensitivity, we generated a construct harboring both V584A and L616A. In order to do so, we used a cloning strategy taking advantage of the presence of a MfeI restriction site between the two sites that need to be mutated. We digested pENTMyoXIaV584A with KpnI and MfeI and kept the smaller fragment, which contained the V584A substitution; we cut pENTMyoXIaL616A with KpnI and MfeI and kept the large fragment, which contained the vector that also had the L616A mutation. The two fragments were ligated together (pENTMyoXIaV584AL616A). An LR Gateway reaction was used to transfer the construct from pENTMyoXIaV584AL616A to pTHUbiGate. The expression clone was tested via complementation assay and preliminary analyses showed complementation at 20°C and significant temperature sensitivity at 32°C.

To introduce the mutations in the myosin XIa locus, a knock-in construct was generated by separately cloning the ~1 kb regions 5' and 3' to the section to be mutagenized. These regions were then assembled with the sequences from the ORF clone pENTMyoXIaV584AL616A. For the 5' homologous arm, a forward primer (MyoXIAKI1F) hybridized on Intron 7 and generated a PCR product with a CACC TOPO-cloning site followed by a SmaI restriction site, a reverse primer (MyoXIAKI1R) hybridized on exon 15 introducing a SalI restriction site through the introduction of a silent mutation. This PCR product was cloned into a TOPO cloning vector (pENTR/D-TOPO) (myoXIa5'arm-TOPO). For the 3' homologous arm, the forward primer (MyoXIAKI2F) hybridized on exon 15 and generated a PCR product with a CACC TOPO-cloning site followed by a SalI restriction site, and the reverse primer (MyoXIAKI2R) hybridized on exon 22 and introduced a SmaI restriction site. This PCR product was cloned into a TOPO cloning vector (myoXIa3'arm-TOPO). The third construct was generated by performing PCR on pENTMyoXIaV584AL616A. The forward primer (MyoXIAKI2F) hybridized on exon 15 and generated a SalI restriction site, and the reverse primer (MyoXIAEX18R) hybridized on exon 18,

downstream an XhoI site. This PCR product was cloned into a TOPO cloning vector (V584AL616A-TOPO) and it contains the two mutations V584A and L616A (respectively on exon 16 and 17) and it does not contain introns 15, 16 and 17. The 3' arm-TOPO and V584AL616A-TOPO vectors were digested with Sall/XhoI; the small fragment of the myoXia3' arm-TOPO and the big fragment of the V584AL616A TOPO were ligated. The resulting plasmid and the myoXia5' arm-TOPO vector were digested with Sall/AscI. The smaller fragment of the first digestion was ligated with the bigger fragment of the myoXia5' arm-TOPO. The ligations generated the final temperature-sensitive knock-in construct (pTOPO-MyoXIA-TSKI). Since, in *P. patens*, myosin XIa and myosin XIb are functionally redundant (Vidali et al., 2010) together with pTOPO-MyoXIA-TSKI we co-transformed a myosin XIb knock-out construct (L1L2-MyoXIB-KO) (Sun et al., 2018), which, by homologous recombination, replaces the myosin XIb gene with a hygromycin cassette. Both constructs were linearized by SwaI digestion and transformed into protoplasts of a moss line expressing Lifeact-mEGFP (Vidali et al., 2009a), and afterward, plants were regenerated as previously described (Liu and Vidali, 2011a).

To select plants in which both the knock-in and knock-out homologous recombination reactions happened successfully, we used a PCR genotyping strategy. From single clones, we extracted the genomic DNA (Quick-DNA Plant/Seed Miniprep Kit, Zymoresearch) and performed PCR. To verify the presence of the myosinXIaTS allele, we used a forward primer (MyoXIAIntron6F) that hybridized on Intron 6, and the reverse primer (MyoXIAIntron18R) which hybridized on Intron 18. These primers amplify a 3.2 Kb band in plants with the myosin XIaTS allele and a 3.7 Kb band in the plants with the wild type allele. To simplify the discrimination between these two bands, we took advantage of the presence of a Sall site in the knock-in construct and digested the PCR product with Sall. After digestion, the 3.2Kb band was cut into two bands of 2.7 Kb and 0.5 Kb.

To verify the insertion of the hygromycin cassette in the myosin XIb gene, a forward primer (MyoXIbEXTGnmc5F) hybridized upstream to exon 1 and a reverse primer (NosLoxR) hybridized on the Lox site on the inserted construct (Sun et al.). These primers amplify a 1.9 Kb band only in plants in which the hygromycin cassette has been inserted in the myosin XIb gene. All reported moss lines are available upon request.

Table 2.1 Primers table. Primers used for cloning of myosin XI TS allele and myosin XI b KO allele

Primers
MyoXIA-L616A-F: ATTGGGAGCTGCAATGGAAAC
MyoXIA-L616A-R: TGTTGCTTGAAACGAGCGC
MyoXIA-V584A-F: TGCCCCTTCGCTGCAAGCCTC
MyoXIA-V584A-R: TCTAGAAGAACCCAACAATGACTGATGTTTCGGC
MyoXIA-L79A-F: GAGCCAGGAGTAGCTTATAATCTTGCT
MyoXIA-L79A-R: ATGCAAATAAGCCAACCTTCGTC
M13F: GTAAAACGACGGCCAG
M13R: CAGGAAACAGCTATGAC
MyoXIAKI1F: CACCATTAAATAATCTGATCTGTTTGTGAATG
MyoXIAKI1R: TTCGTTGCGAAAGTCTCATTGTGCGACTTGGGAAACATG
MyoXIAKI2F: CACCCATGTTTCCCAAGTCGACAAATGAGACTTTCGCAACGAA
MyoXIAKI2R: ATTTAAATGAACGAAAGAACACAGTACCCG
MyoXIAIntron6F: ATGTGGATGTCTTAAGCATATGACTTGTGG
MyoXIAIntron18R: GATACAACTACTGATGGTAGTGAGATGGGTGA
MyoXIbEXTGnmc5F: ACCCTCAATAGAGGAGCCCTTGCTC
NosLoxR: CAGGTCGAAACCCGATCTAGTAACA

2.5.2 Plant morphometric assay

P. patens protoplasts of the myoXIaWT and myoXIaTS lines were regenerated for four days at 25°C (permissive temperature) in PpNH₄ medium containing 10 mM CaCl₂ and 6% Mannitol. After regeneration, protoplasts were transferred to plates containing growing medium (PpNH₄) and placed in a 32°C chamber for three days. All growth chambers were set with a 16 hrs light 8 hrs dark cycle. Plants were stained with calcofluor-white (Fluorescent Brightener 28, Sigma) at a final concentration of 10 µg/ml, to mark their outline and imaged with an inverted epifluorescence microscope Axiovert 200 M (Zeiss) and a 10 X lens (0.25 NA). Imaging was performed with the AxioVision (Zeiss) software. The calcofluor-white signal was imaged with a DAPI filter. Plant area and solidity were measured with an ImageJ Morphology macro (Galotto et al., 2019).

2.5.3. Time-course fluorescent image acquisition

P. patens protoplasts of myoXIaWT and myoXIaTS lines were regenerated for three days at 25°C in PpNH₄ medium containing 10 mM CaCl₂ and 6% Mannitol covered with cellophane. The plants were then transferred on PpNH₄ moss medium at 20°C for 4 days, then transferred on PpNO₃ medium for additional 4 days at 20°C. This procedure allows for the homogenous development of single moss plants and the generation of tissue rich in caulonema cells. Plants were then transferred on control media, or on media containing latrunculin B (Sigma) at a final concentration of 20 µM. Plants were then exposed at 20°C or 32°C for 1.5 hrs, 3 hrs, 5 hrs, 8 hrs. At each time point, plants were transferred on a microscope slide and mounted on an agar pad for imaging. To image the outline of the plant, 30 µl of calcofluor-white (final concentration of 10 µg/ml) was pipetted on the plants. Plants were imaged with an inverted epifluorescence microscope Axiovert 200 M (Zeiss). The calcofluor-white signal was imaged with a DAPI filter. To detect a high-quality image

of the plants, we used an automated technique recently developed in our lab (Galotto et al., 2019). Briefly, we used the MosaiX AxioVision software in combination with an automatic stage that allowed us to save the position of different plants in the microscope slide. For each plant, we imaged a stack of 5 planes 20 μm apart. Images were then processed by an ImageJ macro we developed (available upon request). The macro stitches together the acquired tiles by using an imageJ plugin called “Grid/Collection stitching plugin” (https://imagej.net/Grid/Collection_Stitching_Plugin) (Preibisch et al., 2009) and performs the maximum projection of the plants.

2.5.4. Detection and analysis of cell tip curvature

In order to obtain a metric for quantification of the cell tip shape, we used the imageJ plugin “J Filament” (Smith et al., 2010). By using an in-house ImageJ macro to crop and rotate tips (available upon request), we first cropped single tip cells from the micrographs generated as described in the “Image acquisition” section. All the cells were rotated such that the very tip section of the cells point perpendicularly to the right. We inverted the color of the cropped images in ImageJ and used “Find Edges” command to highlight cell contours. We then proceeded to trace the contours using the JFilament plugin, which gives as an output the $\{x,y\}$ coordinates along the outline. The $\{x,y\}$ coordinates then underwent a linear interpolation using a custom MATLAB code to obtain coordinates with equal spacing of 1 pixel (0.489 μm).

To quantify the cell morphology, we developed a MATLAB code (available upon request), which takes the $\{x,y\}$ coordinates as input and measures the curvatures along the cell peripheries as a function of the distance from the tip. To avoid inherent noise from experiments, and noise introduced by image processing, instead of calculating curvature of each coordinate triplet from

the two bonds connecting the coordinates to its adjacent neighbor, we calculated the curvature using longer bonds. To achieve this, we first drew lines connecting all coordinates. We then drew a circle of radius Δs centered at each of these coordinates. Two new bonds were constructed for each coordinate by drawing lines from the coordinate point (center) to the points where the circle intersects with the contour lines. This process is illustrated in Fig. 2.9. We approximated curvature, $\kappa(s)$, as the angle change with respect to distance, given as

$$\kappa(s) = \Delta\theta / \Delta s ,$$

where $\Delta\theta$ is the change in angle between the two bonds. By doing a parameter scan, we decided that Δs of 4 μm are optimal for noise elimination while still retaining information from cell contours (Fig. 2.10). In addition, each cell was scanned perpendicularly along the x-axis up to contour length of 40 μm from the tip, to find the largest diameter (Fig 2.11).

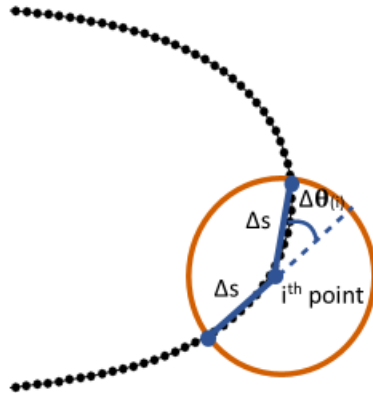


Figure 2.9 Illustration of the curvature calculation along the cell periphery. A circle of radius Δs is drawn around each coordinate, where two bonds are constructed from by drawing lines from the coordinate point (center) to the points where the circle intersects with the contour lines. Curvature is calculated as the change in angle between the two bonds over the new bond length, as described in the methods.

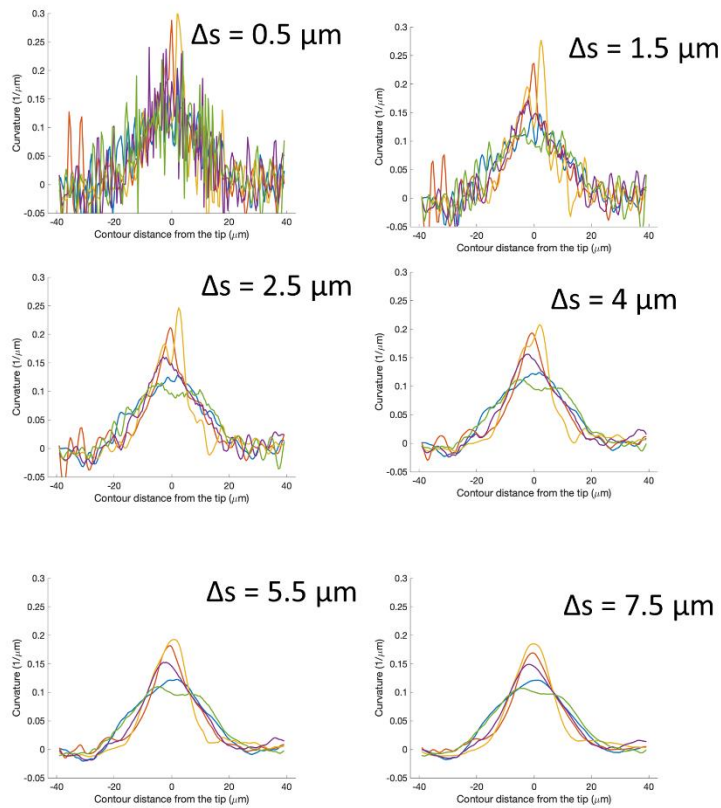


Figure 2.10 Illustration of the maximum width determination. For each cell, we performed horizontal scans from the tip at every $0.5 \mu\text{m}$ along the x-axis of the cell up to the contour length of $40 \mu\text{m}$. Red indicates the scan to the top contour of the cell, and blue indicates the scan to the bottom contour of the cell. The longest length from the top contour to the bottom contour (red bar + blue bar) is reported as the width of the cell.

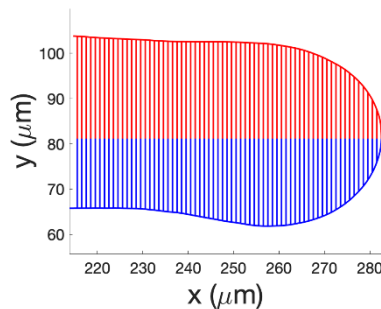


Figure 2.11 Determination of optimal bond spacing for curvature calculations. Curvatures as a function of contour distance from the tip for 5 sample cells are plotted for different bond spacings. The spacing of $4 \mu\text{m}$, which is optimal for noise elimination while still retaining information from cell contours, was selected for all curvature calculations presented in this work.

2.5.5. Bright-field time-lapse imaging of cells transferred to high temperature

One week old *myoXIaWT* and *myoXIaTS* plants, cultured at 20°C, were transferred to a 35 mm glass-bottom dish (Matsunami) suitable for imaging. The dish contains a thick outer layer of agar and a thin inner layer of agar on top of which the plant is positioned. After the plants are transferred, the chambers are placed in the 20°C incubator for 1 week to let the moss adapt, prior to imaging. To image tip growing cells while growing at 32°C, we built a microscope enclosure equipped with a heating system. Bright-field time laps were acquired via a Zeiss Axio Observer.A1, with a 20X objective lens (N.A. 0.3). Images are acquired with the software Micromanager (Edelstein et al., 2014), every 5 minutes for 5 hours. To measure cell growth we generated a kymograph for each cell with the imageJ “multi kymograph” plugin.

2.5.6. Confocal imaging

To observe F-actin and secretory vesicles in the TS background, the *myoXIaWT* and *myoXIaTS* protoplasts were transformed with the pTK-Ubi-3xmCherry-VAMP, which drives protein expression from a constitutive promoter and targets a redundant copy of the ARPC2 gene (Furt et al., 2013). To induce the formation of the ectopic F-actin vesicle clusters (Furt et al., 2013), single *myoXIaWT-VAMP72A1* and *myoXIaTS-VAMP72A1* plants were placed in a round 35 mm confocal dishes (VWR), on top of an agar pad containing latrunculin B (0.25 µM); 20 ul of liquid moss medium containing latrunculin B (0.25 µM) was pipetted on the plants and a small round coverslip secured with VALOP was used to close the preparation. Clusters were imaged with the Leica SP5 scanning confocal microscope. To image cells while exposed to 20°C, the petri dish was placed in a holder connected to a temperature control system (Warner Instruments CL-200) set to 20°C. To image cells while exposed at 32°C, the temperature control system was set to 32°C and a

lens heater (Warner Instruments) was placed on the oil immersion 63X lens (N.A. = 1.4) used for imaging. Prior to imaging, dishes were pre-exposed to 32°C for 15 minutes in an incubator. The temperature in the preparation was detected via a thermocouple placed in proximity to the plant. The 488 and 561 nm laser were used to excite mEGFP and mCherry respectively. The double dichroic 488/561 was used, with bidirectional X laser scanning and pinhole of 2. Z-stacks of 4 optical slices separated by ~6 µm were acquired at 3 sec intervals at 200 Hz laser scanning speed. To image F-actin and secretory vesicles at the cell tip, the same microscopy preparations and temperature control systems were used, with the only difference that 2 ml of mineral oil (VWR) were placed on top of the sealed prep to facilitate temperature detection with a thermocouple. Preparations were kept at 20°C until placed in the microscope stage and the same cell was imaged first at 20°C and then at 32°C. Z-stacks of 10 optical slices were acquired at 200 Hz laser speed, with a pinhole at 1 AU. After acquiring the Z-stack at 20°C, the temperature was switched to 32°C, the second Z-stack was acquired 20 minutes after the temperature in the chamber reached 32°C. Images were enhanced by contrast normalization (0% saturation), gaussian blur (0.6%) and manual adjustment of brightness and contrast levels in ImageJ for display purposes.

2.5.7. Vacuolar staining

The vacuole was stained using the marker MDY-64 (ThermoFisher). The stock solution was prepared in DMSO at 250 µM and diluted in liquid plant medium to a working concentration of 500 nM. *P. patens* plants were exposed at 20°C or 32°C for 2 hrs, then incubated for 15 minutes with the dye, which was subsequently removed by washing twice with liquid plant medium. The samples were imaged with a Leica SP5 Point Scanning Confocal Microscope. MDY-64 was

excited via the 488 nm argon laser, the cells imaged with a 63X lens (N.A. 1.4), and a double dichroic mirror 458/514. For display purposes, the images were γ -adjusted (0.8%) with ImageJ.

2.5.8. Cell death assay

To perform this experiment we used the same settings described in “Image acquisition” section, but prolonging exposure at the stated conditions to 24 hrs. Plants were stained with both calcofluor-white at a final concentration of 10 $\mu\text{g/ml}$, and propidium iodide (Thermo Fisher Scientific) at a final concentration of 20 $\mu\text{g/ml}$. The calcofluor-white and propidium iodide signals were detected with the DAPI and rhodamine filters, respectively. The number of dead cells per plant was estimated by counting of propidium iodide stained nuclei.

2.5.9. Statistical methods

For comparison of multiple treatments, the following statistical test were performed. A two way analysis of variance (morphometric assay), a tree way analysis of variance (cell death assay), t-test (bright-field time-lapse imaging of cells transferred to high temperature), and Fisher’s exact test (confocal imaging) were computed with the Software Graphpad Prism version 8.4.2 for Windows (GraphPad Software, La Jolla California USA, www.graphpad.com). A three way analysis of variance (cell tip curvature and diameter) was performed with R software (www.R-project.org). Comparison of means was done by the Tukey post hoc tests an adjusted P-value of 0.05 was used as significant. Specific information about the number of samples analyzed and the comparisons are specified in the figure legend.

Chapter 3 Chitin Triggers Calcium-mediated Immune Response in the Plant Model *Physcomitrella patens*

The work presented in this chapter has been accepted as a peer reviewed publication in Molecular Plant-Microbe Interactions.

Galotto, G., Abreu, I., Sherman, C., Liu, B., Gonzalez-Guerrero, M., & Vidali, L. (2020). Chitin Triggers Calcium-Mediated Immune Response in the Plant Model *Physcomitrella patens*. Molecular Plant-Microbe Interactions, MPMI-03.

The research that led to this publication was a collaborative effort between members of the Vidali lab at Worcester Polytechnic Institute and of the Gonzalez-Guerrero lab at Universidad Politécnica de Madrid. Luis Vidali, Giulia Galotto and Isidro Abreu conceived the study, as well as designed and supervised the research. Giulia Galotto, Luis Vidali, Isidro Abreu Sanchez and Boyuan Liu performed the experiments. Giulia Galotto, Catherine Sherman and Luis Vidali analyzed and interpreted the data. Giulia Galotto wrote the initial draft of the manuscript and Luis Vidali, Isidro Abreu Sanchez and Manuel Gonzalez-Guerrero edited the draft.

3.1 Abstract

A characteristic feature of a plant immune response is the increase of the cytosolic calcium (Ca^{2+}) concentration following infection, which results in the downstream activation of immune response regulators. The bryophyte *Physcomitrella patens* has been shown to mount an immune response when exposed to bacteria, fungi, or chitin elicitation, in a manner similar to the one observed in *Arabidopsis thaliana*. Nevertheless, whether *P. patens*' response to microorganisms exposure is Ca^{2+} mediated is currently unknown. Here we show *P. patens* plants treated with chitin oligosaccharides exhibit Ca^{2+} oscillations, and that a calcium ionophore can stimulate the

expression of defense-related genes. Chitin oligosaccharide treatment also results in an inhibition of growth, which can be explained by the depolymerization of the apical actin cytoskeleton of tip growing cells. These results suggest that chitin triggered calcium oscillations are conserved and were likely present in the common ancestor of bryophytes and vascular plants.

3.2 Introduction

In nature, both abiotic stresses (e.g., salinity, dehydration, high UV exposure) and biotic stress (pathogen attack) are a threat to plant growth and survival. When plants are attacked by a microbial pathogen, a defense response cascades from the recognition of the pathogen to the expression of defense-related genes. In plants, pattern recognition receptors (PRR) expressed on the plasma membrane, recognize pathogen-associated/microbe-associated molecular patterns (PAMPs and MAMPS respectively) (Albert et al., 2010a). This interaction induces PAMP-triggered immunity (PTI), or MTI (Boller and Felix, 2009; Peng et al., 2018). Commonly studied PRR are FLS2 and EFR1 (Kunze et al., 2004; Altenbach and Robatzek, 2007), which recognize bacterial proteins, and LYK5, which, together with LYK4, are the primary detectors of fungal chitin (Cao et al., 2014). LYK4/5, upon detection of chitin oligosaccharides, activates CERK1, a major co-receptor involved in chitin response (Miya et al., 2007). Upon PRR activation, cytoplasmic Ca²⁺ concentration increases, and a simultaneous MAPK phosphorylation cascade triggers a defense response that includes synthesis of defense hormones, defense gene activation, and in vascular plants, lignification of the cell wall (Ponce de Leon and Montesano, 2017).

Bryophytes, such as the plant model *Physcomitrella patens*, share characteristics with the common ancestor between bryophytes and vascular plants: this makes *P. patens* a great model to study the evolution of the plant immune response (Nishiyama et al., 2003; Lang et al., 2008; Alvarez et al.,

2016). Initially, *P. patens* was used as a model system to study plant immune response because of its sensitivity to both the bacterium *Erwinia carotovora* and the fungus *Botrytis cinerea* (Ponce de Leon et al., 2007). Such infections result in the manifestation of many disease symptoms in moss, including tissue maceration, cytoplasmic shrinkage, chloroplasts darkening, and expression of defense-related genes (Ponce de Leon et al., 2007). Further characterization of *P. patens* immune response triggered by fungi of the genus *Pythium* showed that moss activates a response common to flowering plants, including accumulation of phenolic compounds and callose in the cell wall, ROS production, cell death and accumulation of Jasmonic acid (JA) and its precursor 12-oxo-phytodienoic acid (OPDA) (Oliver et al., 2009). *Pythium* infection also results in the transcription of defense-related genes, such as PAL, CHS, LOX, and PR-1 (Oliver et al., 2009). In a recent study, Alvarez et al. performed an in-depth characterization of transcriptional activation in *P. patens* following *Pectobacterium carotovorum* infection (Alvarez et al., 2016). This study allowed for the identification of pathways involved in defense response against pathogens. Furthermore, in this study, several genes coding for cell wall reinforcement, such as dirigent-like proteins (DIR), were identified as overexpressed (Alvarez et al., 2016). DIR proteins participate in plant pathogen defense by mediating the production of the cell wall polymers (Davin and Lewis, 2000). To activate all these responses, plants express PRR on their plasma membrane as an initial line of defense (Albert et al., 2010b). Interestingly, it has been shown that *P. patens* expresses the PRR CERK chitin receptor (Bressendorff et al., 2016), while homologs of the *Arabidopsis thaliana* FLS2 and EFR have not been identified (Ponce de Leon and Montesano, 2017). CERK activation by fungal chitin stimulates a downstream response, which in *P. patens* has similarities to vascular plants, generating an oxidative burst (Lehtonen et al., 2012), and more recently demonstrated that

MAPK are rapidly activated via phosphorylation in response to chitin elicitation and fungal infection (Bressendorff et al., 2016).

A hallmark of plant immune response to biotic and abiotic stress is the increase of the cytosolic calcium (Ca^{2+}) concentration following infection (Seybold et al., 2014). *A. thaliana* exhibits an increase in Ca^{2+} in leaves, roots and guard cells in response to osmotic stress (Yuan et al., 2014; Cao et al., 2017). *A. thaliana* also responds to herbivore attack, in a glutamate-dependent mechanism that triggers a Ca^{2+} response (Toyota et al., 2018). Drought and salinity stressors in *P. patens* cause a burst of Ca^{2+} waves that originate at the base of the gametophore and propagate throughout the whole plant (Storti et al., 2018). Therefore, we hypothesize that in response to chitin oligosaccharides, similarly to vascular plants, cytosolic Ca^{2+} will increase and propagate periodically throughout the plant.

To address our hypothesis, we examined Ca^{2+} response to chitin oligosaccharides in *P. patens*. The small size and simple cytology of this plant allowed us to analyze the response at the plant level and at the cell level. To visualize cytosolic Ca^{2+} levels in response to chitin oligosaccharides, we used a *P. patens* line expressing the Ca^{2+} sensor GCaMP6f (Nakai et al., 2001; Chen et al., 2013). This line was also transformed with the fluorescent probe Lifeact-Ruby2 (Wu and Bezanilla, 2018), which allows simultaneous visualization of the actin cytoskeleton and Ca^{2+} . Our results show that following exposure to chitin oligosaccharides, Ca^{2+} oscillation propagates across the whole plant in a dose-dependent manner. At the cellular level, chitin oligosaccharides cause dissipation of the tip localized actin cytoskeleton essential for cell growth. Additionally, we showed that Ca^{2+} influx itself (mediated by ionomycin ionophore) is enough to trigger a pathogenesis-like response in *P. patens*.

3.3 Results

3.3.1 Chitin oligosaccharides affect plant growth and morphology in a dose-dependent manner

To investigate the effect of chitin oligosaccharides on plant growth and morphology, we performed a growth assay in the presence of increasing concentrations of chitin oligosaccharides. After regenerating *P. patens* protoplasts for 4 days, plants were transferred to growth media containing different concentrations of chitin oligosaccharides. After 3 days of exposure to the chitin oligosaccharides, plants were imaged. Our results show plant size and morphology are affected by chitin oligosaccharides in a dose-dependent manner (Figure 3.1A and 1B). Interestingly, plants exposed to chitin oligosaccharides have a non-uniform distribution of cellulose on their walls: the calcofluor-white fails to stain the entire plant cell wall. For this reason, for visualization and analysis purposes, we merged the calcofluor-white and chlorophyll auto-fluorescence channels (see methods). To quantify the observed morphological changes, we measured plant area and solidity as previously described (Vidali et al., 2007) (Figure 3.1B). Plant area and solidity were estimated from the merged calcofluor-white and chlorophyll signals (see above); plant solidity was calculated by computing the ratio of the area over the convex hull area (Vidali et al., 2007). Plant area progressively decreases when plants are exposed to increasing chitin oligosaccharides concentrations; curve fitting using a variable slope model (GraphPad software) produced an IC50 value of 266 ± 44 $\mu\text{g/ml}$ (SEM). Plant solidity, which is an indirect estimate of polarized cell

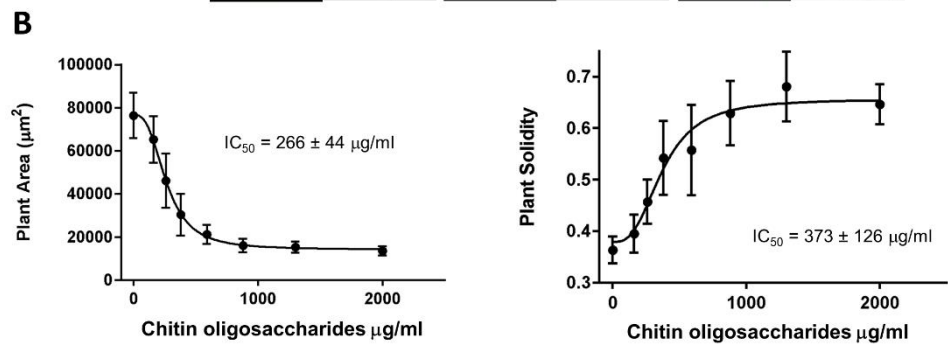
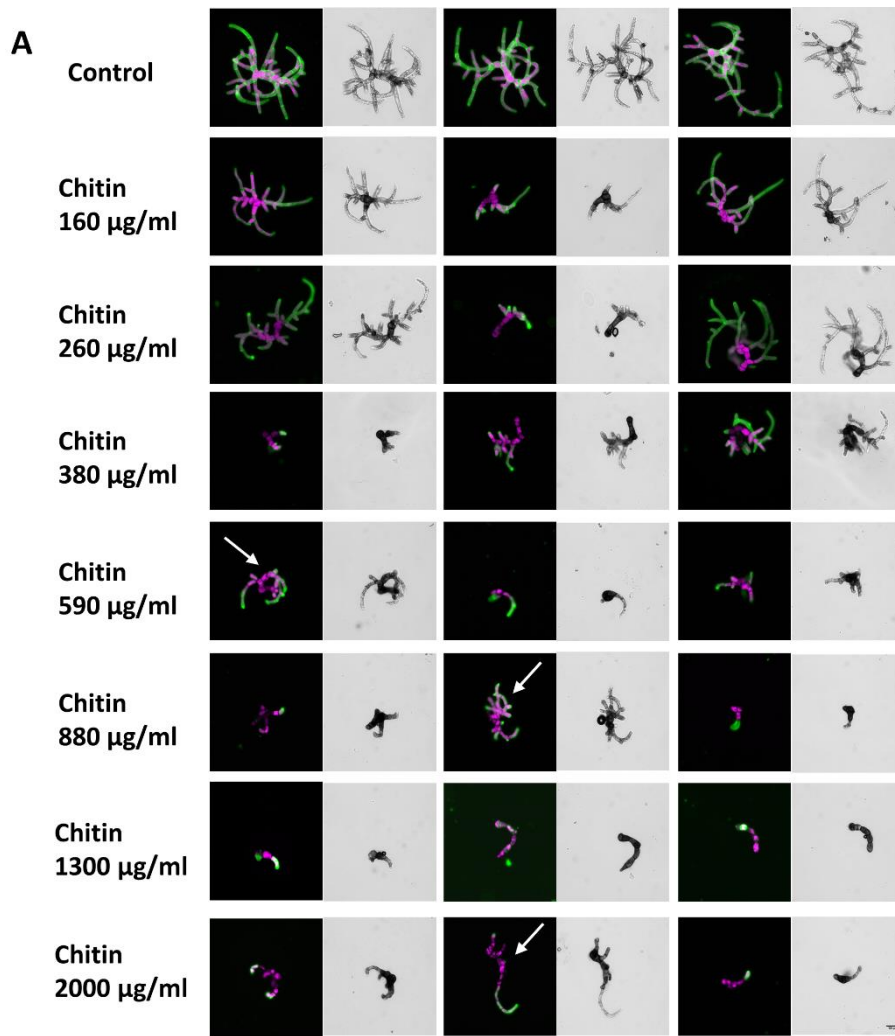


Figure 3.1 Exposure to chitin affects plant size and morphology in a dose-dependent manner **A**, Representative images of 1-week-old plants acquired via epifluorescence microscopy. In the panel, green represents calcofluor staining and magenta the chlorophyll autofluorescence. Arrows indicate examples of plants exhibiting a less severe phenotype in response to chitin oligosaccharides. **B**, Exposure to increasing concentration of chitin oligosaccharides results in a reduction of plant area and an increase in plant solidity. Quantification of plant area and solidity in plants exposed to increasing concentration of chitin oligosaccharides. Number of plants analyzed: control plants, 75; plants exposed at 160 $\mu\text{g/ml}$, 74; plants exposed at 260 $\mu\text{g/ml}$, 79; plants exposed at 380 $\mu\text{g/ml}$, 75; plants exposed at 590 $\mu\text{g/ml}$, 78; plants exposed at 880 $\mu\text{g/ml}$, 76; plants exposed at 1300 $\mu\text{g/ml}$, 78; plants exposed at 2000 $\mu\text{g/ml}$, 75. Three biological replicates were performed.

growth, progressively increases with higher concentrations of chitin oligosaccharides, assuming values closer to 1, typical of stunted and less branching plants. For plant solidity values, curve fitting using a variable slope model generated an IC_{50} value of $373 \pm 126 \mu\text{g/ml}$ (SEM). To our surprise, we observed *P. patens* plants show a non-homogenous response to chitin oligosaccharides. While the majority of plants share the same altered phenotype, some exhibit a less dramatic phenotype and appear to be less affected by chitin oligosaccharides, some examples of this are visible in figure 3.1A.

3.3.2 Ca^{2+} oscillations originate following elicitation with chitin oligosaccharides

To examine the effect of Ca^{2+} at the plant level, we used a *P. patens* line expressing the cytoplasmic Ca^{2+} sensor GCaMP6f (Chen et al., 2013). We generated single one-week-old plants, treated them with chitin oligosaccharides for 10 minutes and recorded changes in intracellular Ca^{2+} levels using the fluorescence microscope. Upon chitin oligosaccharides addition, Ca^{2+} oscillations propagate throughout the whole plant (Supplemental Figure S1). Because the chitin oligosaccharides used are a mixture of oligosaccharides with different numbers of N-acetyl-glucosamine units, we sought to investigate if a well-defined number of units is needed to trigger a response. Hence, we repeated the experiment by using chitohexaose and chitotriose (Figure 3.2). We found that chitohexaose triggers an equivalent global Ca^{2+} response to the chitin oligosaccharides. These results indicate that a critical number, higher than three N-acetyl-glucosamine units, is required to cause a response

in moss (Figure 3.2). Similarly to the chitin oligosaccharide treatment, upon chitohexaose application, Ca^{2+} oscillations propagate throughout the whole plant, with what sometimes appear to be waves traveling within and between cells (Figure 3.2A, compare Movies S1-S3). To quantify the magnitude of the Ca^{2+} response, we calculated the time-averaged of the mean gray values across the time series (30 min) for the different chitohexaose and chitotriose concentrations. Our results show the cytoplasmic Ca^{2+} increase is dose-dependent: as the chitohexaose concentration increases, the time-averaged mean gray values of Ca^{2+} fluorescence signal also increase (Figure 3.2B-left). A similar dose-response is observed with chitin oligosaccharides treatment (Supplemental Figure S1), while chitotriose only triggers a minimal response at the concentrations used (Figure 3.2B-left). Curve fitting using the Agonist concentration vs. response with three parameters model generated an $\text{EC}_{50} = 2.2 \pm 0.5 \mu\text{M}$ ($\pm\text{SEM}$) for the chitohexaose, and an $\text{EC}_{50} = 468.3 \pm 189.3 \mu\text{M}$ for the chitotriose. Similarly, the standard deviation of the time-averaged mean grey value increases in treated plants, with an $\text{EC}_{50} = 0.9 \pm 0.4 \mu\text{M}$ for the chitohexaose treatment, and an $\text{EC}_{50} = 101.1 \pm 31.6 \mu\text{M}$ for the chitotriose treatment. This increase in standard deviation indicates that there is a greater amplitude of the Ca^{2+} peaks when plants are treated with higher concentrations of chitohexaose and to a much lesser extent, chitotriose (Figure 3.2B-right).

The period of the Ca^{2+} oscillations appeared to be more frequent when the plants were exposed to the higher concentration of chitin oligosaccharides and chitohexaose (Supplemental Figure S1 and Figure 3.2A). To determine the changes in frequency, we used a peak detection algorithm (see methods). This algorithm analyzes the fluorescence intensity values across all the pixels in a plant over time (Figure 3.2C), and detects the Ca^{2+} peaks in a group of nine pixels across the time series (Figure 3.2D). The period of the oscillation in a plant is calculated from the average time elapsed between peaks (Figure 3.2D) for all the pixels, and the peak frequency is computed from the

period. When plants are exposed to an increasing concentration of chitin oligosaccharides or chitohexaose, the number of detected Ca^{2+} peaks increases (Figure 3.2E and Supplemental Figure S1). On the other hand, treatment with chitotriose does not significantly increase the number of peaks compared to the control (Figure 3.2E). Control plants or plants treated with a low concentration of chitohexaose have very few peaks (Figure 3.2E-left). As the chitohexaose concentration increases, the number of peaks that can be detected increases, with a peak frequency of $0.39 \pm 0.04 \text{ min}^{-1}$ ($\pm\text{SEM}$) for $100 \mu\text{M}$ chitohexose treatment (Figure 3.2E). This frequency corresponds to an average period between peaks of $2.6 \pm 0.3 \text{ min}$. The number of peaks and the peak frequency become significantly different from the control (adjusted P value below 0.001) at a concentration of $10 \mu\text{M}$ or above. Differently than chitohexaose, chitotriose treatment does not affect the number of peaks or the peak frequency (Figure 3.2E). A similar result is obtained when plants are treated with chitin oligosaccharides (Figure 3.3); when plants are treated with a concentration of 0.2 mg/ml or above, the number of peaks increases and the average period is approximately 2 min per peak (Figure 3.3E).

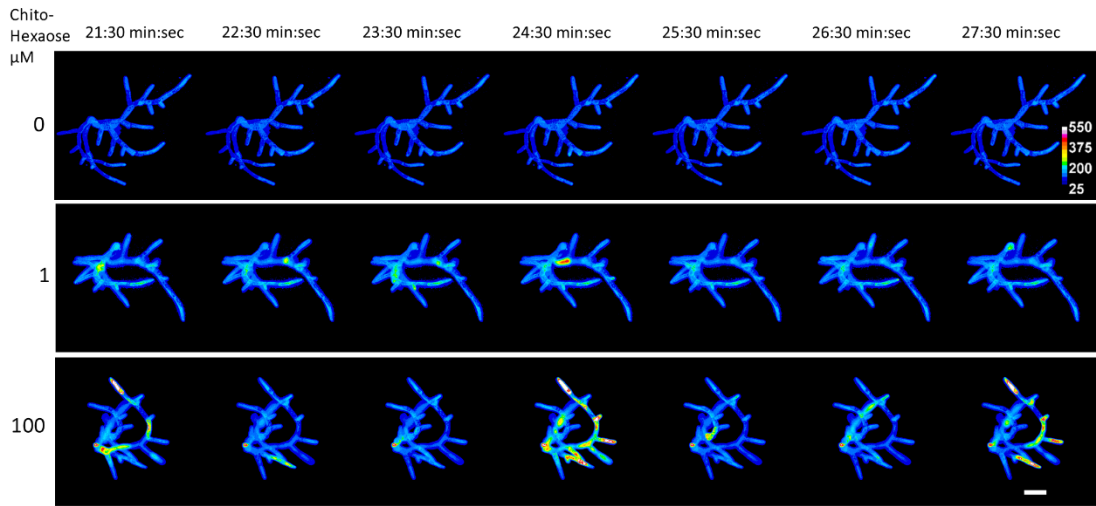
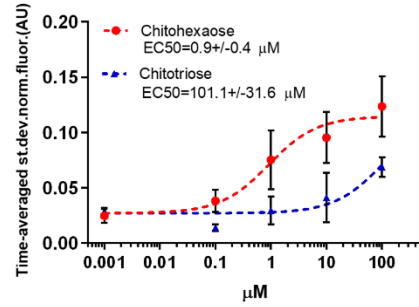
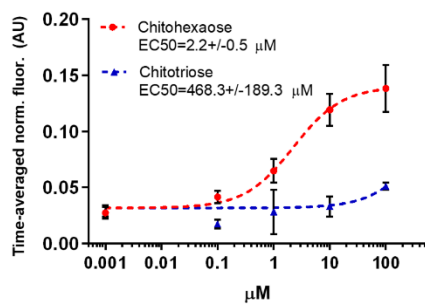
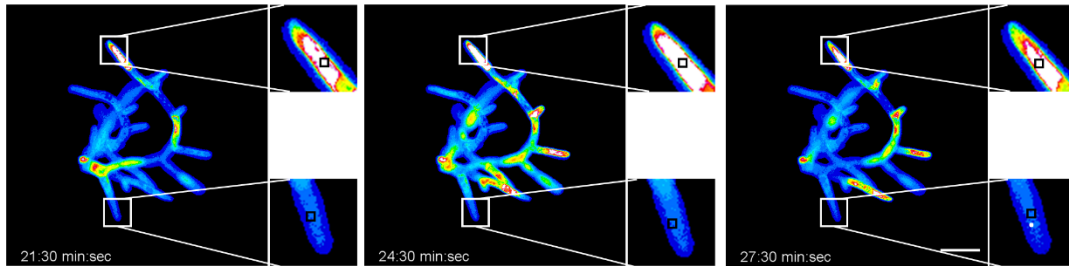
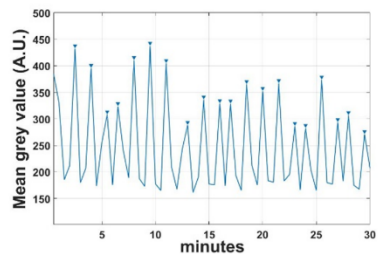
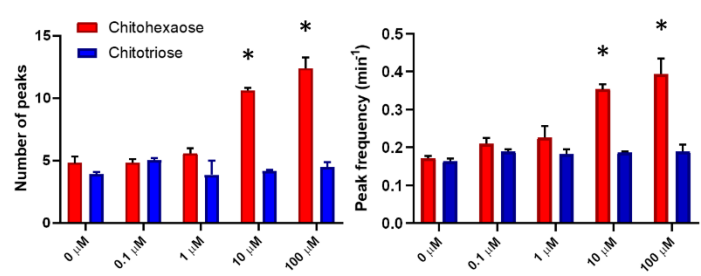
A**B****C****D****E**

Figure 3.2 Plants at concentrations 0, 1, 0.1, and 10 and 100 μM chitohexaose. **A**, Plants at concentrations 0, 1, 0.1, and 10 and 100 μM chitohexaose. Scale bar 50 μm . **B**, Time-averaged mean grey value (left panel) and the standard deviation (right panel) of the time-averaged mean grey value are normalized by $(F - F_0)/F_0$ for chitohexaose and chitotriose treated plants. Each point represents the average of at least 3 plants across 30 minutes of imaging, a total of three independent experiments were performed for each condition. **C**, Example of a plant treated with 100 μM chitohexaose, imaged for 30 minutes. Side images are examples of the image processing. Each window contains a 3 x 3 pixel grid, highlighted in black (not to scale in the picture). The mean grey value in each grid is measured across time. Each plant results in approximately 200,000 pixel grids. The period of each grid was extracted using a peak detection program in MATLAB. Scale bar 50 μm . **D**, Example of a peak graph for a plant treated with 100 μM chitohexaose, the detected peaks are indicated with arrows. **E**, Number of peaks per plant (left panel) and frequency of peaks in minutes^{-1} (right panel) in plants treated with chitohexaose and chitotriose. A total of 3 plants were analyzed per treatment per experiment, and 3 independent experiments were conducted (each treatment had 3 control plants—no chitin oligosaccharides added). For the chitohexaose treated plants, the number of peaks and the peak frequency become significantly different from the control at a concentration of 10 μM or above. Asterisks indicate a significant difference to the control (adjusted P value below 0.001) (Ordinary one-way ANOVA). For the chitotriose treated plants, there is no statistically significant difference.

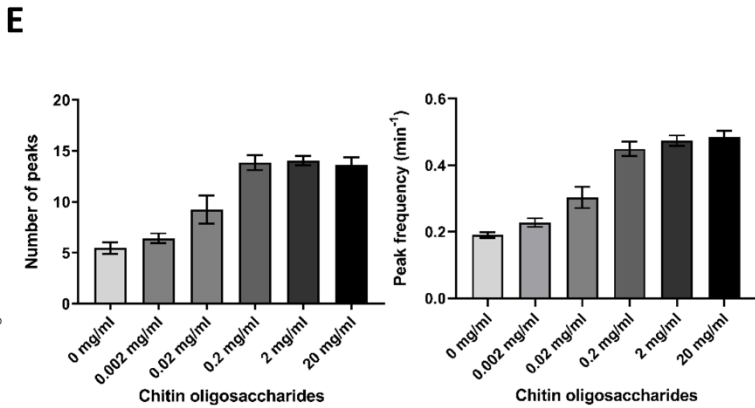
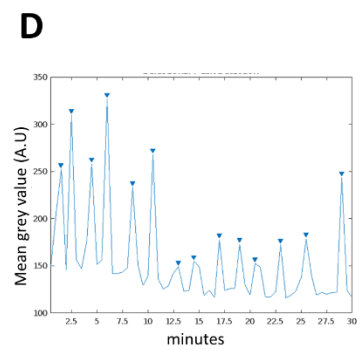
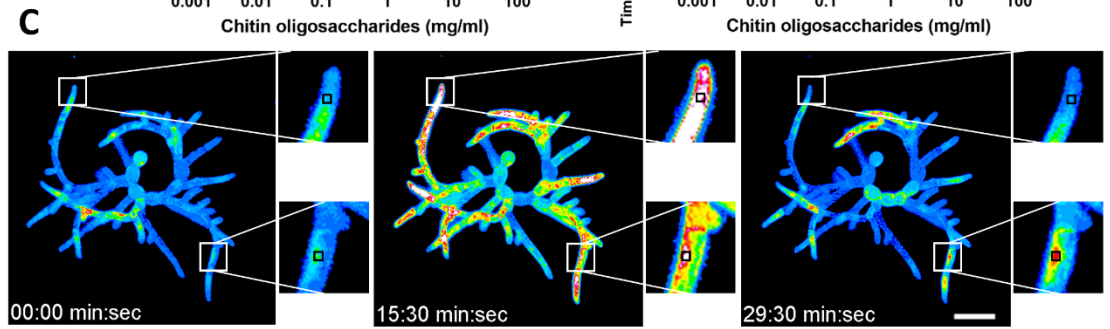
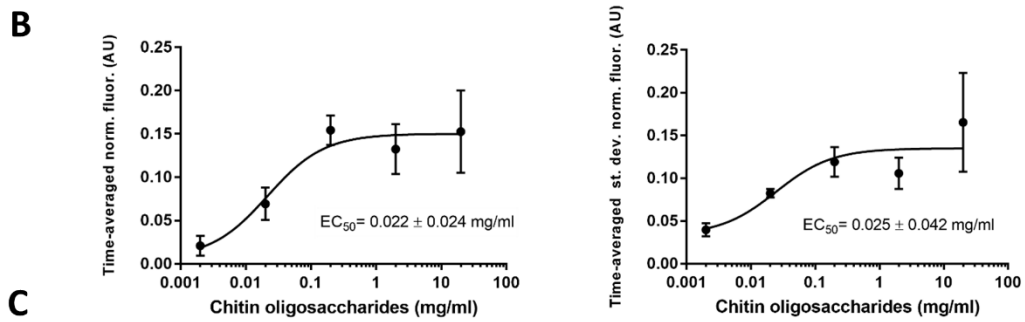
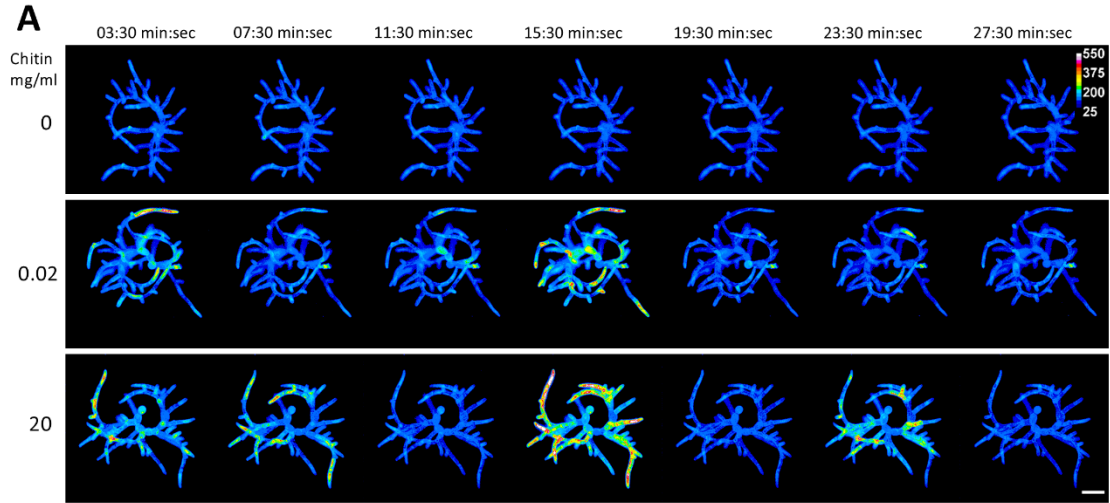


Figure 3.3 Chitin oligosaccharides affects cytosolic Ca²⁺ concentrations. A, Plants at concentrations 0, 0.02, and 20 mg/ml chitin oligosaccharides. Scale bar 100 μ m. B, Time-averaged mean grey value (left panel) and the standard deviation (right panel) of the time-averaged mean grey value are normalized by $(F - F_0)/F_0$. Each point represents the average of at least 3 plants across 30 minutes of imaging, a total of four independent experiments were performed for each condition. C, Example of a plant treated with 20 mg/m chitin oligosaccharides, imaged for 30 minutes. Side images are examples of the image processing. Each window contains a 3 x 3 pixel grid, highlighted in black (not to scale in the picture). The mean grey value in each grid is measured across time. Each plant results in approximately 200,000 pixel grids. The period of each grid was extracted using a peak detection program in MATLAB. Scale bar = 50 μ m. D, Example of a peak graph, the detected peaks are indicated with arrows. E, Number of peaks per plant (left panel) and period between peaks in minutes (right panel). A total of 3 plants were analyzed per treatment per experiment, and 4-6 independent experiments were conducted (each treatment had 3 control plants—no chitin added). The number of peaks and the peak period become significantly different from the control (adjusted P value below 0.01) at a concentration of 0.2 mg/ml or above (Kruskal-Wallis non-parametric test).

3.3.3 Chitin oligosaccharides dissipate F-actin at the tip of the cell

P. patens cells have a dynamic cortical actin cytoskeleton and a fluctuating apical accumulation of F-actin filaments focused at the tip of the cell (Vidali et al., 2009a; Furt et al., 2013). The latter is essential for growth, as demonstrated by growth inhibition caused by pharmacological inhibition of F-actin (Vidali et al., 2009a; Furt et al., 2013) and mathematical modeling (Bibeau et al., 2018). As exposure of *P. patens* plants to chitin oligosaccharides exhibit a reduced growth and altered solidity, we decided to investigate whether the observed growth phenotype is due to chitin oligosaccharides-induced defects in the F-actin cytoskeleton of filamentous tip growing cells. We generated a line that expresses the Lifeact-Ruby2 fluorescent probe in our cytoplasmic Ca²⁺ sensor GCaMP6f cell line, which allows visualization of the actin cytoskeleton. We imaged the actin cytoskeleton following treatment with 100 μ g/mg of chitin oligosaccharides. Interestingly, the F-actin enriched spot at the tip of the cell dissipates within seconds after chitin oligosaccharides exposure (Figure 3.3A and Movies S4 and S5), and the cell stops growing. This result shows that the F-actin cytoskeleton is affected by chitin oligosaccharides in a fast way. Furthermore, following the addition of chitin oligosaccharides the Ca²⁺ oscillation pattern at the tip region

appears altered. In untreated cells, the oscillations are periodic and restricted to the apical domain, exhibiting frequent peaks of variable amplitude. After application of chitin oligosaccharides, the Ca^{2+} signal is not only restricted to the apical domain, but throughout the whole cell, and fewer Ca^{2+} peaks were observed when analyzing the apical region of the tip cell (Figure 3B, compare top and bottom).

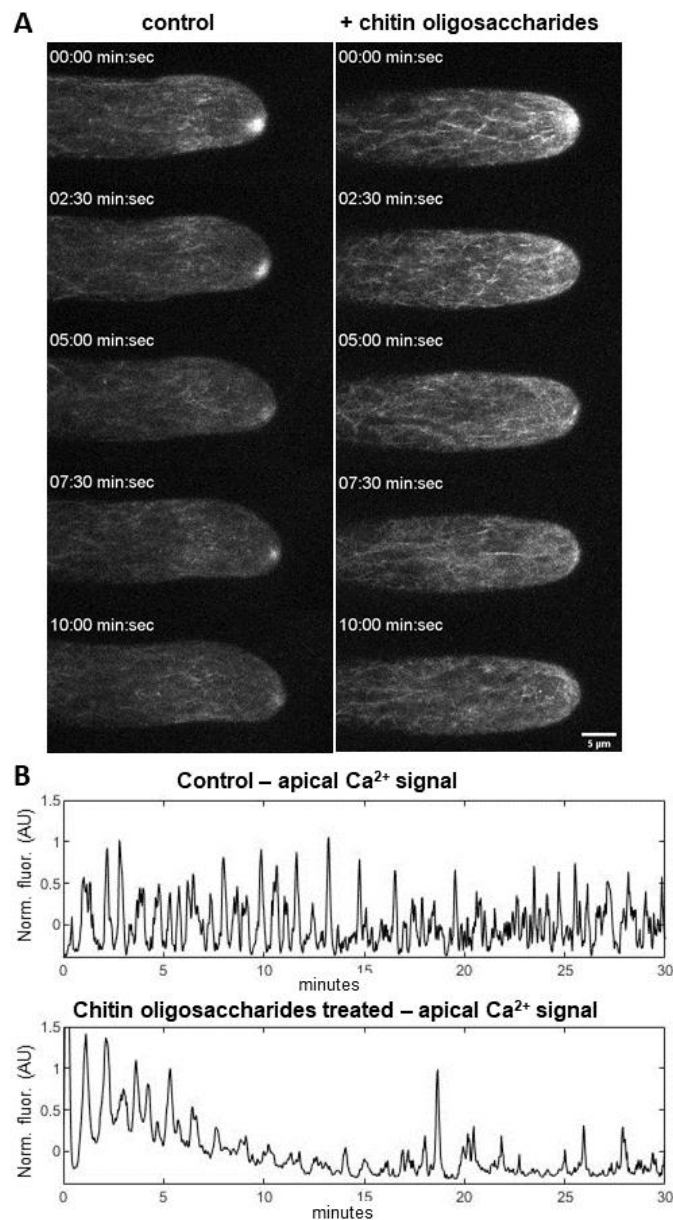


Figure 3.4 Chitin oligosaccharides treatment dissipates the apical F-actin focus and alters Ca^{2+} oscillations in tip cells. **A**, Chitin oligosaccharides (100 $\mu\text{g}/\text{ml}$) dissipate the actin spot at the tip of the cell. Z-projections of 5 optical slices acquired with confocal laser scanning microscopy. Actin is labeled with Lifeact-Ruby2. **B**, Chitin oligosaccharides oscillation at the tip is affected by chitin oligosaccharides. The graphs show representative traces for the Ca^{2+} concentration of control and chitin oligosaccharides treated cells. The Ca^{2+} fluorescence was analyzed using MATLAB program that analyzed pixel values above zero for every frame, the pixels' grey values were averaged and normalized by subtracting the average of the time-series, and dividing the result by the standard deviation of the time series. Number of plants analyzed: 5 control plants and 4 plants exposed at 100 $\mu\text{g}/\text{ml}$. Three independent experiments were performed.

3.3.4 Chitin oligosaccharides and the calcium-ionophore ionomycin induce expression of defense-related genes

To test whether Ca^{2+} influx have a biological significance in the pathogenesis response of *P. patens*, we analyzed the mRNA levels via RT-qPCR of the pathogenesis-responsive genes Phenylalanine Ammonia Lyase4 (PpPAL4), Chalcone Synthase (PpCHS) and PpCERK1 (homolog of the Chitin Elicitor Receptor Kinase1 from Arabidopsis) (Oliver et al., 2009; Bressendorff et al., 2016) in plants treated with chitin oligosaccharides or the Ca^{2+} ionophore ionomycin (Figure 3.4). As previously shown, chitin oligosaccharides induce expression of PpPAL4, PpCHS and PpCERK1 in a gradual manner, with the maximum expression observed at 60 minutes. Ionomycin treatment also induces the expression of pathogenesis-responsive genes, although there is no obvious gradual response, proving the gene expression is Ca^{2+} dependent. The intensity of the transcriptional response triggered by ionomycin is generally lower than with chitin oligosaccharides, except at short exposure times, when relative expressions of PpCHS and PpCERK1 were similar in both treatments.

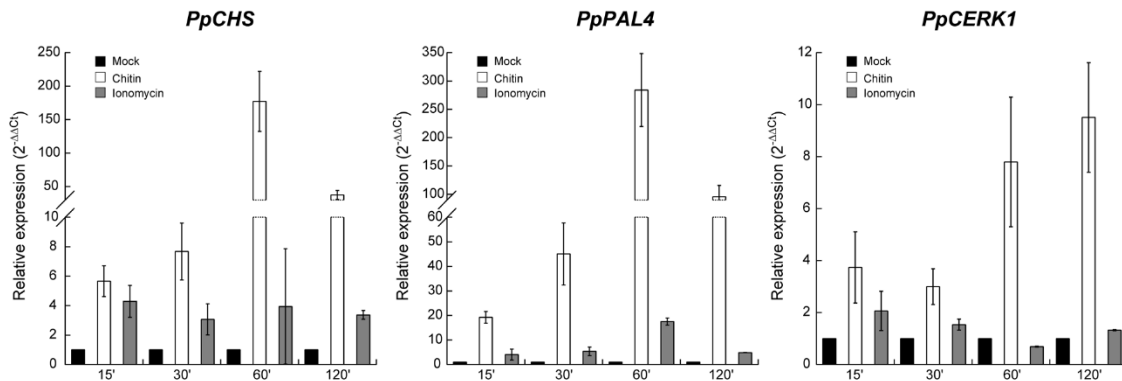


Figure 3.5 Expression of pathogenesis related genes in response to chitin oligosaccharides and ionomycin treatment RT-qPCR of CHS, PAL4 and CERK1 transcript levels as fold change relative to the wild type mock treatment at times specified after chitin oligosaccharides (100 $\mu\text{g}/\text{mL}$) or ionomycin (100 mM) treatment. Data points represent an average of two-four independent experiments each with two technical replicates for each PCR reaction. Error bar represent SEM.

3.4 Discussion

The main findings of this study are that *P. patens* treated with chitin oligosaccharides exhibits Ca^{2+} oscillations and that the Ca^{2+} oscillations affect plant growth via the depolymerization of the cytoskeleton at the cell tip. These conclusions are based on the following experimental evidence. First, we demonstrated that chitin oligosaccharides affect plant growth and morphology in a dose-dependent manner. Next, we observed and characterized the Ca^{2+} oscillations that originate following elicitation with chitin oligosaccharides. We then provided evidence that chitin oligosaccharides dissipate F-actin at the tip of the cell, important for cell growth. Finally, we reported that several defense-related genes that are expressed in chitin oligosaccharides treated plants can be induced by artificially increasing cytosolic Ca^{2+} . Together, these results strongly support the hypothesis that *P. patens* immune response triggered by chitin oligosaccharides is Ca^{2+} mediated.

The increase in cytosolic Ca^{2+} we observed in *P. patens* is common to the vascular plants' response to various biotic stresses. Application of chitin oligosaccharides (100 $\mu\text{g/ml}$) on leaves of 14 to 16 days-old seedlings results in oscillation of cytoplasmic Ca^{2+} that lasts about 20 minutes (Keinath et al., 2015). In the same study, it was reported that 100 nM bacterial derived peptide flagellin causes a systemic Ca^{2+} increase that lasts for 30 minutes (Keinath et al., 2015). Ma et al. also detected intracellular Ca^{2+} stimulation induced by flagellin as well as by the pathogen *P. syringae* (Ma et al., 2017). Interestingly, our dose-response results show an EC_{50} for the Ca^{2+} response to the chitohexaose of 0.9-2.2 μM , which is very similar to the binding affinity of the *A. thaliana*, chitin receptor AtLYK5 for chitooctaoase ($\text{Kd} = 1.72 \mu\text{M}$) (Cao et al., 2014), which suggest that a similar type of receptor may mediate the response in *P. patens*. Furthermore, we observed that six but not three N-acetyl-glucosamine units are required to trigger a Ca^{2+} response --differently than chitohexaose, chitotriose did not show a significant response. The precise minimum number of units required will need further investigation, but in *A. thaliana*, Cao et al. showed chitohexaose, but not chitopentaose, trigger an immune response via an increase in ROS (Cao et al., 2014). In our work, the transcript levels of three defense-related genes (PAL4, CHS, and CERK1) increased in chitin oligosaccharides treated plants and in plants treated with a Ca^{2+} ionophore. The same transcripts were found increased following pathogens attack in *P. patens* (Ponce de Leon et al., 2007; Oliver et al., 2009; Alvarez et al., 2016; Bressendorff et al., 2016), suggesting a link exists between Ca^{2+} signaling and the moss' response to pathogens.

The actin cytoskeleton is involved in pathogen response as a defense mechanism against microbe penetration (Hardham et al., 2007; Schmidt and Panstruga, 2007). In vascular plants, the actin cytoskeleton network thickens at the site of infection, and its pharmacological inhibition facilitates infections (Higaki et al., 2011). Henty-Rydilla et al., show that, in epidermal cotyledon cells,

treatment with 1 μM chitin increases actin filaments abundance (Henty-Ridilla et al., 2013). These results are in discordance with what we observed in apical cells. However, our study focused specifically on tip growing cells. Hence, it would be interesting to investigate whether the observed modulation in *A. thaliana* cytoskeleton by chitin is also observed in *A. thaliana* tip growing cells (root hairs and pollen tubes).

In *P. patens* plants subjected to abiotic stresses such as NaCl, sorbitol, mannitol, and upon osmotic changes, cytosolic Ca^{2+} concentration rises in a systemic way (Storti et al., 2018). Together with our results, Storti, et al.'s study provides evidence that different kinds of stresses, detected by different receptors, have a common pathway that converges in triggering a Ca^{2+} increase. However, how plants discriminate between different types of stresses is still unknown. Importantly, by identifying an additional Ca^{2+} dependent pathway, our study gets us closer to understanding the mechanisms behind the capacity of the plant to respond differently to different stresses.

A. thaliana guard cells and root hairs show a different Ca^{2+} response to flagellin and chitin oligosaccharides than epidermal cells, indicating the response is tissue-specific (Keinath et al., 2015). Interestingly, when the effect of osmotic stress was investigated in *P. patens* 1-2 month-old leafy gametophore, the response at the base of the gametophore was four times higher than in the phyllids (Storti et al., 2018). Hence, future studies will be needed to investigate how different *P. patens* cell types at different developmental stages respond to chitin oligosaccharides. We focused on the one week old *P. patens* plant because it can be imaged in the field of view of the microscope at low magnification, capturing the response of the organism in its entirety. Our investigation is limited to the protonemal tissue, which is mainly composed of chloronemata cells, and only of a limited amount of caulonemata cells. Future experiments should focus on studying the difference in response to chitin between caulonemata and chloronemata, which could be achieved with a

similar experimental setting to what we used here to analyze Ca^{2+} at the single-cell level (confocal microscopy).

Remarkably, we observed two different types of oscillatory behavior. Growing protonemata show an oscillatory tip-focused Ca^{2+} gradient (Bascom et al., 2018b), similar to the one observed in other plant tip growing cells (Pierson et al., 1996; Monshausen et al., 2008), while chitin oligosaccharide-induced oscillations are not tip-focused, and appear to behave in a wave-like fashion, sometimes encompassing the whole plant. Furthermore, the period of the tip-focused oscillations is faster, with only ~30 sec. between peaks, while the period of the chitin oligosaccharides-induced oscillations is slower, with ~2 min. elapsing between peaks. Future studies addressing the identity, location, and activity of Ca^{2+} transporters (channels and pumps) should help clarify how these two different oscillatory behaviors are generated and maintained.

Our study suggests chitin oligosaccharides-triggered immune response in moss is Ca^{2+} dependent. This response has been previously reported in vascular plants, suggesting the immune response among land plants could be conserved. Future research is needed to identify the chitin receptors in moss and to uncover the molecular mechanism between the Ca^{2+} and immune responses. Published evidence shows *P. patens* genome harbors four homologs of the *A. thaliana* chitin receptor AtCERK1 (Bressendorf et al., 2016). Furthermore, *P. patens* encodes at least two copies of the LysM receptor kinases (LYKs) (Zhang et al., 2009), which are essential for chitin recognition in *A. thaliana* (Cao et al., 2014), and at least three copies of genes encoding homologs of the LYP receptor-like proteins similar to OsCEBiP (Zhang et al., 2009). Identifying if the *P. patens* receptors mediate the observed Ca^{2+} response would show whether this response is conserved between mosses and vascular plants. Our study on land plant immune response sets the basis for future characterization of Ca^{2+} signaling of non-vascular land plant and microbe interactions.

3.5 Material and Methods

3.5.1. Biological material and growth conditions

All cell lines used in this study were derived from the moss *Physcomitrella patens* (Hedw.) Bruch & Schimp., Gransden strain. *P. patens* cell lines were cultured and transformed using established methods (Liu and Vidali, 2011b).

3.5.2. Morphometric analysis

P. patens protoplasts were regenerated for four days in medium containing 10 mM CaCl₂ and 6% Mannitol; after regeneration (4 days), protoplasts were transferred to growth medium containing increasing concentrations (160 µg/ml, 260 µg/ml, 380 µg/ml, 590 µg/ml, 880 µg/ml, 1300 µg/ml, 2000 µg/ml) of chitin oligosaccharides (Tokyo Chemical Industry-TCI). Three days after exposure to chitin oligosaccharides, plants were stained with a working concentration of 10 µg/ml calcofluor-white (dissolved in water) to mark the outline of the plants. Plants were imaged with an inverted epifluorescence microscope Axiovert 200 M (Zeiss). The calcofluor-white signal was imaged with a DAPI filter, and the chlorophyll auto fluorescence was detected by using the filter cube GFP-30-LP-B-zhe zero (Semrock brightline). Since the chitin oligosaccharides treated plants exhibit non-uniform calcofluor-white staining, for analysis purposes we merged the calcofluor-white and chlorophyll auto-fluorescence channel. Plant area and solidity were measured by using an ImageJ Morphology macro as previously described (Galotto et al., 2019).

3.5.3 Generation of a moss line expressing the Ca²⁺ sensor GCaMP6f and Lifeact-Ruby2

To construct the plasmid for expression of GCaMP6f in *P. patens* we amplified the GCaMP6f open reading frame from plasmid pGP-CMV-GCaMP6f (Chen et al., 2013) (AddGene) with

forward and reverse primers containing attB1 and attB2, respectively. The PCR fragment was Gateway-cloned into the pDONR207 vector via BP clonase (Thermo) and the product transferred via LR clonase (Thermo) to pTH-Ubi-Gate, a vector with the Gateway cloning site downstream of the maize ubiquitin promoter; this vector provides hygromycin resistance for selection of transformed moss plants (Vidali et al., 2007). Moss protoplasts were simultaneously transformed with the pTH-Ubi-GCaMP6f construct and a pTZ-Ubi-lifeact-Ruby2 (Vidali et al., 2009a; Wu and Bezanilla, 2018) construct to label the actin cytoskeleton. Stable transformants were identified by two rounds of selection of hygromycin (15 µg/ml) and zeocin (50 µg/ml).

3.5.4 Ca²⁺ imaging

P. pantens plants expressing GCaMP6f were imaged with a Zeiss Axio Observer.A1 equipped with a motorized microscope stage. The plants were imaged with a 10X objective lens (NA 0.25). The Ca²⁺ sensor was excited with a mercury lamp X-Cite series 120 PC EXFO. The microscope slides were prepared with agar pads as previously reported (Galotto et al., 2019). Two 75 mm x 25 mm microscope slides, one with chitin oligosaccharides treated plants, one with untreated plants, were mounted on a 50 mm x 76 mm slide. Plants were imaged 10 minutes after the application of chitin oligosaccharides solution. Plants were treated with increasing concentration of chitin oligosaccharides (Tokyo Chemical Industry-TCI) at 0 mg/ml, 0.002 mg/ml, 0.02 mg/ml, 0.2 mg/ml, 2 mg/ml, 20 mg/ml, and Hexa-N-acetylchitohexaose (chitohexaose) and N,N',N''-Triacetylchitotriose (chitotriose) (Cayman Chemical) at 0 µM, 0.1 µM, 1 µM, 10 µM, 100 µM. For imaging, the positions of single plants were saved as spatial coordinates by using the software Micro-Manager (Edelstein et al., 2014). Single plants were then imaged every 30 sec. for 30 min. To enhance sensitivity, a binning of 2 was applied to the CCD camera (Cool-SNAP Photometrics).

3.5.5 Ca²⁺ time-series image analysis

The time series of *P. patens* expressing the Ca²⁺ sensor GCaMP6f exposed to chitin oligosaccharides were analyzed with an ImageJ macro (available upon request). The macro applies, for each frame in the series, a thresholding function that masks the background signal; the masked images were used to analyze the Ca²⁺ peaks in chitin oligosaccharides and chitohexaose and chitotriose treated plants (see Calcium Peak Detection Analysis). In addition, the ImageJ macro records the mean gray value of each image. To analyze the chitin oligosaccharides-treated plants, the collected mean gray values were normalized with an R script (available upon request) as follows. The R program computes the average of the mean gray value for each control plant across the time series (control time-series mean), and averages this time-series mean for the three control plants in one data set (F0). The data for each treated plant in the experiment were then normalized in the following way. For each frame in the time series, F0 is subtracted from each mean grey value (F) and then divided by F0, resulting in: $(F - F0)/F0$. The resulting values are averaged over time (normalized time-series mean). For the chitohexaose and chitotriose normalization was done by finding the baseline for each individual time series (R package “baseline”, function “modpolyfit”) and subtracting the baseline from the complete time series and then dividing the resulting values by the baseline $(F-F0)/F0$, this approach has the advantage that the water treated controls can be used for the subsequent curve fitting analysis. For each experiment from all treatments, the $(F-F0)/F0$ value was averaged for the three observed plants. An increase in the above value is an indication of higher Ca²⁺ levels in the plant but does not provide information about fluctuations in the Ca²⁺ levels. To estimate this, we analyzed the standard deviation of the normalized time-series mean, which provides information about the

variance of the signal over time. This analysis was repeated for each chitin oligosaccharides concentration used.

3.5.6 Ca²⁺ peak detection analysis

The masked images produced by the ImageJ macro (see Ca²⁺ Time-Series Image Analysis) were analyzed using a MATLAB script (available upon request) to identify peaks in the signal that could constitute oscillatory behavior. The program uses a rolling 3x3 pixel grid to detect the position occupied by the plant throughout the video. For each frame, the grid scans through the image and records the pixel value of a 3x3 pixel area. Only the grids with positive values are considered as being part of a plant. When all the positive pixels are identified in one plant, the MATLAB script computes the mean of the pixels values at each time point. The script also calculates the standard deviation of the mean for the entire time series. The script then finds the Ca²⁺ peaks corresponding for each pixel in the complete time series. A signal is considered a peak when its intensity is greater than a fraction of the standard deviation (0.345 x standard deviation) from the mean gray value of the plant over the complete time series. Once the peak detection is completed, the number of peaks and the period between peaks was measured with a built-in MATLAB function (findpeaks). The results from all pixels were averaged to get a value per plant and the value from three plants was averaged by experiment.

3.5.7 Confocal imaging of actin and Ca²⁺

The *P. pantens* plants expressing the Ca²⁺ sensor GCaMP6f also express the fluorescent probe Lifeact-Ruby2 for simultaneous visualization of Ca²⁺ and actin cytoskeleton. Plants were cultured in 35 mm glass-bottom dishes in PpNO₃ medium as previously described (Furt et al., 2013). Such plants were imaged with a Leica SP5 scanning confocal microscope. The Ca²⁺ sensor was excited

via the 488 nm argon laser; the Lifeact-Ruby2 fluorophore was excited with the 561 nm laser. Before imaging, plants were treated with 200 μ l of liquid medium containing chitin oligosaccharides at a final concentration of 100 μ g/ml. Plants were imaged with 63X lens (N.A. 1.4), zoom = 5, five Z-planes separated by \sim 1.5 μ m, every 2 seconds, for 30 minutes. F-actin images were Z-projected using maximum intensity, contrast enhanced by normalizing to the stack's histogram, and filtered with a Gaussian blur filter set to a sigma = 0.5; all processing was done with ImageJ.

3.5.8 Ca²⁺ confocal image analysis

The *P. patens* plants expressing the Ca²⁺ sensor GCaMP6f were analyzed with an ImageJ macro (available upon request) to adjust for their growth during analysis. The input for the macro are the coordinates of the tip at the start and end of the time series and a freehand selection of the tip area. The macro creates a black mask around the cell boundary that moves at the growth rate of the cell. The output are masked images for the time series of the Ca²⁺ and F-actin channels. The output images from the previous macro were analyzed for changes in fluorescence intensity with a MATLAB script (available upon request). For every frame, the pixels with values above zero, which correspond to the Ca²⁺ signal, were averaged and normalized by subtracting the average of the time-series, and dividing the result by the standard deviation of the time series. The resulting value was then plotted over time.

3.5.9 RNA extraction and RT-qPCR

Effect of chitin oligosaccharides and ionomycin in gene expression was tested as follows. *P. patens* grew as indicated were transferred to Petri dishes (5 cm diameter) containing 2 mL of liquid media supplied with chitin oligosaccharides (100 μ g/mL)(Sigma) or ionomycin (100 μ M)(Invitrogen).

At the indicated times (15, 30, 60 and 120 minutes), excess media was removed and plants were immediately frozen in liquid nitrogen. RNA was obtained from *P. patens* using Tri-Reagent (Life Technologies), treated with DNase Turbo (Life Technologies) to remove DNA contamination, and cleaned with RNeasy Mini kit (Qiagen). RNA integrity was confirmed by electrophoresis, and possible DNA contamination tested by PCR using the RNA samples as templates. cDNA was synthesized from 500 ng of DNA-free RNA using PrimeScript RT reagent Kit (Takara), supplemented with RNase out (Life Technologies). Expression studies were carried out by real-time reverse transcription polymerase chain reaction (RT-qPCR) using the StepOne plus thermocycler (Applied Biosystems), with the Power SyBR Green master mix (Applied Biosystems). Primers for the pathogenesis-responsive genes Phenylalanine Ammonia Lyase4 (PpPAL4), Chalcone Synthase (PpCHS) and PpCERK1 (homolog of the Chitin Elicitor Receptor Kinase1 from Arabidopsis), and the reference gene PpTubulin1 were described elsewhere (Bressendorff et al., 2016). The threshold cycle (Ct) was determined in duplicates from independent experiments (n=2-4). The relative levels of expression were determined using the $2^{-\Delta \Delta Ct}$ method, using the mock treatment as the reference condition.

Chapter 4 Future directions and conclusions

4.1 Further testing of myosin XI as a driver of vesicle clustering for tip accumulations

As discussed in Chapter 2, our experiments using the myosin XI TS allele show myosin XI is essential for vesicle clustering and F-actin enrichment. In addition, our dual observation of F-actin and VAMP-labelled vesicles revealed the formation of myosin XI-dependent vesicle clusters propelled by F-actin polymerization. We concluded myosin XI-bound secretory vesicles carry F-actin nucleators, in a feedback loop driven by myosin XI. To directly test this hypothesis, it would be interesting to use pharmacological inhibitors to target the two main F-actin nucleators in *P. patens*, Formin II or Arp2/3 complex, and attempt to reproduce the motile clusters. Failure to form motile clusters will confirm our model. Two available inhibitors are CK 666 (Fisher Scientific), which targets the Arp2/3 complex, and SMIFH2 (Millipore), which target formin. The clusters we observed resemble the F-actin “comet tails” responsible for pathogens (such as *Listeria monocytogenes*) motility during mammalian cell infection (Gouin et al., 2005). CK 666 has been successfully used to inhibit Arp2/3 complex induced F-actin polymerization in *Listeria* F-actin comet tails (Nolen et al., 2009). A more challenging but very informative way to confirm the minimal component of the observed clusters, and further show their dependence on myosin XI is to perform *in vitro* reconstitution of the clusters using the purified proteins. This experiment will allow the identification of the minimal protein machinery necessary for F-actin nucleation from the vesicles and, importantly, *in vitro* reconstitution with and without different amounts of purified myosin XI will further show the effects of this motor on the vesicle clustering process. This approach has been successfully used to identify components required for actin-based motility and actin dynamics in the aforementioned *Listeria* comet tails (Loisel et al., 1999). Finally, modeling with stochastic simulators, such as cytosim can provide a further evidence of the dynamics between

myosin XI, F-actin, and secretory vesicles are biologically possible (Nedelec and Foethke, 2007). Using this tool it is possible to model the behaviour of a set of components (proteins, cytoskeleton) by defining their biochemical, mechanical and physical properties (e.g., association rates, speed of polymerization, bending elasticity, filament stiffness, binding forces). This type of modeling is a powerful tool to discriminate if cellular components, based on their intrinsic properties, can self-organize and behave as predicted.

4.2 Myosin XI role in the regulation of cytoplasmic organization, vacuole structure, and cell viability

As outlined in Chapter 2, our results link myosin XI to the maintenance of cytoplasmic homeostasis, specifically concerning vacuole structure and cell viability. Interestingly, the RNASeq and gene ontology (GO) enrichment analysis showed that a lack of functional myosin XI results in modulation of the microtubules cytoskeleton. Interestingly, it was reported microtubules regulate vacuole dynamics in chloronemal and rhizoid cells in *P. patens* (Oda et al., 2009). To study microtubules' involvement in caulonemal cells in relation to myosin XI, microtubules can be fluorescently tagged in the myosin XI TS line. This would allow us to observe if the distribution and dynamics of microtubules are affected by a decrease of functional myosin XI. Furthermore, to visualize if microtubules are colocalized with vacuoles in caulonema cells. In addition, investigating if microtubule depolymerization by oryzalin treatment also attenuates the observed vacuole phenotype would clarify vacuole regulation in caulonemal cells. Myosin XI could be directly responsible for vacuolar transport, a hypothesis that could be confirmed by identifying myosin XI interactors on the tonoplast membrane. A yeast two-hybrid screening using the myosin XI tail was performed in the lab and output potential myosin XI interactors. A localization study of the verified interactors via yeast two-hybrid could indicate protein localized to the vacuole,

followed by co-immunoprecipitation of the protein extracts. Some preliminary work was performed to this end and showed the myosin XI tail interactor Arl8 (a small GTPase) localizes to vacuoles in *P. patens*, but further experiments need to confirm its *in vivo* interaction with myosin XI (Foley, 2019).

The cell death induced by prolonged lack of myosin XI does not appear to be due to the activation of the programmed cell death pathway. In fact, our RNASeq experiment did not generate hits related to plant apoptosis. However, our experiment was performed two hours after incubation at 32°C, and transcriptome analysis at later time points could reveal if a cell death pathway takes place. Also, the unexpected result that F-actin depolymerization results in protection of vacuole aberrations and cell death could be further investigated by performing RNASeq of myosin XI TS plants treated with latrunculin B. The comparison of this condition with non-latrunculin B treated plants could shed light on the pathway/proteins involved in vacuole regulation and cell viability.

4.3 Characterizing the morphology of myosin XI TS cells via modeling and fluorescent markers

As presented in Chapter 2, our data link myosin XI to cell growth and morphology. Myosin XI-deprived cells exhibit drastically slow growth and apical swelling. Furthermore, our investigation shows myosin XI or/and F-actin loss-of-function affect morphology differently, and that myosin XI depleted cells have higher curvature values (pointier) than F-actin depleted cells (blunter). Mathematical modeling efforts have worked in parallel to experimental studies to shed light on mechanisms underlying tip growth (Campàs and Mahadevan, 2009; Rojas et al.; Campas et al., 2012). The more parameters are accurately measured to be input in a model, the more accurate the model will be. The curvature values we reported represent a metric description of the cell's shape

in the absence of functional myosin XI and F-actin or both. These values can be used in future modeling to guide our experiments toward our understanding of polarized growth.

One of the phenotypes observed in our TS experiment is swelling in the apical area of the cell. Upon myosin XI and F-actin loss of function, proper cell polarization is lost. To further characterize the mechanism behind the observed apical and lateral swelling, future experiments will benefit from the expression in the myosin XI TS line of a polarization marker. As previously discussed, Rho of plants (Rop) GTPases and its activators GEFs are crucial for plant cell polarization (Yalovsky et al., 2008). GEFs, which include ROPGEFs and spikes, are localized at the apex of tip growing cells in vascular plants and are essential for cell polarity (Gu et al., 2006; Kost, 2008). Fluorescently labeled ROPGEFs have been observed to localize to the tip of *P. patens* caulonema cells, suggesting its apical localization is essential for polarized expansion (Ito et al., 2014; Le Bail et al., 2019). Observing if the localization of RopGEFs in myosin XI TS exposed at the restrictive temperature is altered will provide insights into the participation of this motor in the regulation of RopGEFs localization in *P. patens*.

4.4 Further investigation of *P. patens* chitin perception

As outlined in chapter 3, *P. patens*' immune response to biotic stresses is Ca^{2+} -mediated. Our results show a minimal number of N-acetyl-glucosamine units (six but not three) are required to trigger a Ca^{2+} response. In *A. thaliana* the number of N-acetyl-glucosamine units has to be six or more to trigger a response (Cao et al., 2014). It would be interesting to verify if this minimal number is conserved, and if chitopentaose can trigger a Ca^{2+} response in *P. patens*.

Work in *A. thaliana* showed Lyk5 is the main chitin receptor and that chitin-binding to Lyk5 is necessary for Cerk1 heterodimerization, activation, and further MAP kinase signal transduction (Cao et al., 2014). Recently, our lab demonstrated a functional homology between the chitin receptors in *A. thaliana* and *P. patens* (Orr et al., 2020b). RNAi of the *P. patens* Lyk5 a/b/c, which exhibit sequence homology to *A. thaliana* Lyk 2/5/6, inhibit the chitin induced- Ca^{2+} (Orr et al., 2020b). This fascinating result shows land plants and vascular plants share the same chitin detection sensor. Similarly to *A. thaliana*, *P. patens* Cerk1 is involved in chitin detection (Bressendorff et al., 2016). It would be interesting to verify if *P. patens* Cerk1 activation is dependent on Lyk5 binding to chitin, as in *A. thaliana*. This would deepen our understanding of *P. patens* response to chitin.

In our work, the investigation of chitin was limited to protonemal cells in the juvenile stage of the organism. We specifically observed the effect of chitin on the apical F-actin in caulonemal cells. the effect of chitin in chloronema cell apical F-actin remains to be investigated. Caulonema and chloronema cells exhibit differences in organelles distribution (Furt et al., 2012), apex F-actin organization (Vidali et al., 2009a), and in growth rate (Rounds and Bezanilla, 2013). These differences could account for a different response to threats. Furthermore, To have a holistic understanding of the response, it would be interesting to investigate the response at the gametophore stage, to verify if a systemic response, and cell to cell communication are maintained in later developmental stages.

Our data show that, remarkably, the signal originating in each cell is synchronized at the plant level. Furthermore, we observed two distinct periods of the oscillation, at the tip of the cell (30 sec) and in the whole plant (2 min). Identifying Ca^{2+} transporters (channels and pumps) could shed light on the generation of these two apparently different oscillatory mechanisms. To this end, a

forward genetic screen that isolates mutants in Ca^{2+} signature could reveal genes that code for a Ca^{2+} transporter in *P. patens*.

4.5 Conclusions

In this work, we elucidated the role of myosin XI in tip growth in *P. patens* and linked myosin XI to the maintenance of cell tip shape and curvature, vacuole homeostasis, and cell viability. We found that the a primary function of myosin XI is to cluster VAMP-labelled vesicles in a mechanism that increases the concentration of vesicles and local F-actin. To date, the plant field only assumed the role of myosin XI to be related to vesicle transport, but an experimental confirmation of this function was lacking. By exploiting the use of a temperature-sensitive allele, we provided direct evidence myosin XI not only transports, but it clusters vesicle at the cell tip.

While the immune response to abiotic stress had been previously addressed in *P. patens*, knowledge about the response to biotic stress was still lacking. The detection of a cytosolic Ca^{2+} signature in *P. patens* shows the response to biotic stress has common features between bryophytes and vascular plants.

Chapter 5 References

- Abu-Abied, M., Belausov, E., Hagay, S., Peremyslov, V., Dolja, V., and Sadot, E.** (2018). Myosin XI-K is involved in root organogenesis, polar auxin transport, and cell division. *J Exp Bot* **69**, 2869-2881.
- Ahn, C.S., Han, J.A., and Pai, H.S.** (2013). Characterization of in vivo functions of *Nicotiana benthamiana* RabE1. *Planta* **237**, 161-172.
- Akerboom, J., Carreras Calderón, N., Tian, L., Wabnig, S., Prigge, M., Tolö, J., Gordus, A., Orger, M.B., Severi, K.E., and Macklin, J.J.** (2013). Genetically encoded calcium indicators for multi-color neural activity imaging and combination with optogenetics. *Frontiers in molecular neuroscience* **6**, 2.
- Albert, M., Jehle, A.K., Lipschis, M., Mueller, K., Zeng, Y., and Felix, G.** (2010a). Regulation of cell behaviour by plant receptor kinases: Pattern recognition receptors as prototypical models. *Eur J Cell Biol* **89**, 200-207.
- Albert, M., Jehle, A.K., Mueller, K., Eisele, C., Lipschis, M., and Felix, G.** (2010b). *Arabidopsis thaliana* pattern recognition receptors for bacterial elongation factor Tu and flagellin can be combined to form functional chimeric receptors. *Journal of Biological Chemistry* **285**, 19035-19042.
- Aldon, D., Mbengue, M., Mazars, C., and Galaud, J.-P.** (2018). Calcium signalling in plant biotic interactions. *International journal of molecular sciences* **19**, 665.
- Alonso, J.M., and Ecker, J.R.** (2006). Moving forward in reverse: genetic technologies to enable genome-wide phenomic screens in *Arabidopsis*. *Nat Rev Genet* **7**, 524-536.
- Alonso, J.M., Stepanova, A.N., Leisse, T.J., Kim, C.J., Chen, H., Shinn, P., Stevenson, D.K., Zimmerman, J., Barajas, P., and Cheuk, R.** (2003). Genome-wide insertional mutagenesis of *Arabidopsis thaliana*. *Science* **301**, 653-657.
- Altenbach, D., and Robatzek, S.** (2007). Pattern recognition receptors: from the cell surface to intracellular dynamics. *Mol Plant Microbe Interact* **20**, 1031-1039.
- Alvarez, A., Montesano, M., Schmelz, E., and Ponce de Leon, I.** (2016). Activation of shikimate, phenylpropanoid, oxylipins, and auxin pathways in *Pectobacterium carotovorum* elicitors-treated moss. *Front Plant Sci* **7**, 328.
- Alves, F., Michard, E., and Feijó, J.A.** (2009). The role of ion fluxes in polarized cell growth and morphogenesis: the pollen tube as an experimental paradigm. *International Journal of Developmental Biology* **53**, 1609-1622.
- Anderhag, P., Hepler, P.K., and Lazzaro, M.** (2000). Microtubules and microfilaments are both responsible for pollen tube elongation in the conifer *Picea abies* (Norway spruce). *Protoplasma* **214**, 141-157.
- Anders, S., Pyl, P.T., and Huber, W.** (2015). HTSeq—a Python framework to work with high-throughput sequencing data. *Bioinformatics* **31**, 166-169.
- Anderson, P.** (1995). Mutagenesis. In *Methods in cell biology* (Elsevier), pp. 31-58.
- Arioli, T., Peng, L., Betzner, A.S., Burn, J., Wittke, W., Herth, W., Camilleri, C., Hofte, H., Plazinski, J., Birch, R., Cork, A., Glover, J., Redmond, J., and Williamson, R.E.** (1998). Molecular analysis of cellulose biosynthesis in *Arabidopsis*. *Science* **279**, 717-720.
- Arrowsmith, C.H., Audia, J.E., Austin, C., Baell, J., Bennett, J., Blagg, J., Bountra, C., Brennan, P.E., Brown, P.J., and Bunnage, M.E.** (2015). The promise and peril of chemical probes. *Nature chemical biology* **11**, 536-541.
- Ashford, A.** (1998). Dynamic pleiomorphic vacuole systems: are they endosomes and transport compartments in fungal hyphae? *Advances in botanical research* **28**, 120-161.

- Augustine, R.C., Vidali, L., Kleinman, K.P., and Bezanilla, M.** (2008). Actin depolymerizing factor is essential for viability in plants, and its phosphoregulation is important for tip growth. *Plant Journal* **54**, 863-875.
- Augustine, R.C., Pattavina, K.A., Tüzel, E., Vidali, L., and Bezanilla, M.** (2011). Actin interacting protein1 and actin depolymerizing factor drive rapid actin dynamics in *Physcomitrella patens*. *Plant Cell* **23**, 3696-3710.
- Avisar, D., Abu-Abied, M., Belausov, E., and Sadot, E.** (2012). Myosin XIK is a major player in cytoplasm dynamics and is regulated by two amino acids in its tail. *J Exp Bot* **63**, 241-249.
- Balint-Kurti, P.** (2019). The plant hypersensitive response: concepts, control and consequences. *Molecular plant pathology* **20**, 1163-1178.
- Bannigan, A., Scheible, W.R., Lukowitz, W., Fagerstrom, C., Wadsworth, P., Somerville, C., and Baskin, T.I.** (2007). A conserved role for kinesin-5 in plant mitosis. *J Cell Sci* **120**, 2819-2827.
- Barnabas, B., and Fridvalszky, L.** (1984). Adhesion and Germination of Differently Treated Maize Pollen Grains on the Stigma. *Acta Botanica Hungarica* **30**, 329-332.
- Bascom, C., Jr., Burkart, G.M., Mallett, D.R., O'Sullivan, J.E., Tomaszewski, A.J., Walsh, K., and Bezanilla, M.** (2019). Systematic survey of the function of ROP regulators and effectors during tip growth in the moss *Physcomitrella patens*. *J Exp Bot* **70**, 447-457.
- Bascom, C.S., Jr., Hepler, P.K., and Bezanilla, M.** (2018a). Interplay between Ions, the Cytoskeleton, and Cell Wall Properties during Tip Growth. *Plant Physiol* **176**, 28-40.
- Bascom, C.S., Jr., Winship, L.J., and Bezanilla, M.** (2018b). Simultaneous imaging and functional studies reveal a tight correlation between calcium and actin networks. *Proc Natl Acad Sci U S A*.
- Baskin, T.I., Betzner, A.S., Hoggart, R., Cork, A., and Williamson, R.** (1992). Root morphology mutants in *Arabidopsis thaliana*. *Functional Plant Biology* **19**, 427-437.
- Ben-Aroya, S., Pan, X., Boeke, J.D., and Hieter, P.** (2010). Making temperature-sensitive mutants. In *Methods in enzymology* (Elsevier), pp. 181-204.
- Bezanilla, M., Pan, A., and Quatrano, R.S.** (2003). RNA interference in the moss *Physcomitrella patens*. *Plant Physiol* **133**, 470-474.
- Bezanilla, M., Perroud, P.F., Pan, A., Klueh, P., and Quatrano, R.S.** (2005). An RNAi system in *Physcomitrella patens* with an internal marker for silencing allows for rapid identification of loss of function phenotypes. *Plant Biol (Stuttg)* **7**, 251-257.
- Bhargava, A., and Srivastava, S.** (2019). *Participatory Plant Breeding: Concept and Applications*. (Springer).
- Bibeau, J.P., Kingsley, J.L., Furt, F., Tuzel, E., and Vidali, L.** (2018). F-Actin mediated focusing of vesicles at the cell tip is essential for polarized growth. *Plant Physiol* **176**, 352-363.
- Bibeau, J.P., Furt, F., Mousavi, S.I., Kingsley, J.L., Levine, M.F., Tuzel, E., and Vidali, L.** (2020). In vivo interactions between myosin XI, vesicles and filamentous actin are fast and transient in *Physcomitrella patens*. *J Cell Sci* **133**.
- Bibikova, T.N., Zhigilei, A., and Gilroy, S.** (1997). Root hair growth in *Arabidopsis thaliana* is directed by calcium and an endogenous polarity. *Planta* **203**, 495-505.
- Bibikova, T.N., Blancaflor, E.B., and Gilroy, S.** (1999). Microtubules regulate tip growth and orientation in root hairs of *Arabidopsis thaliana*. *Plant Journal* **17**, 657-665.
- Blum, M., De Robertis, E.M., Wallingford, J.B., and Niehrs, C.** (2015). Morpholinos: antisense and sensibility. *Developmental cell* **35**, 145-149.
- Bolger, A.M., Lohse, M., and Usadel, B.** (2014). Trimmomatic: a flexible trimmer for Illumina sequence data. *Bioinformatics* **30**, 2114-2120.
- Boller, T., and Felix, G.** (2009). A renaissance of elicitors: perception of microbe-associated molecular patterns and danger signals by pattern-recognition receptors. *Annu Rev Plant Biol* **60**, 379-406.

- Bourne, H.R., Sanders, D.A., and McCormick, F.** (1991). The GTPase superfamily: conserved structure and molecular mechanism. *Nature* **349**, 117-127.
- Boyd, L.A., Ridout, C., O'Sullivan, D.M., Leach, J.E., and Leung, H.** (2013). Plant–pathogen interactions: disease resistance in modern agriculture. *Trends in genetics* **29**, 233-240.
- Brand, A.H., and Perrimon, N.** (1993). Targeted gene expression as a means of altering cell fates and generating dominant phenotypes. *development* **118**, 401-415.
- Bressendorff, S., Azevedo, R., Kenchappa, C.S., Ponce de Leon, I., Olsen, J.V., Rasmussen, M.W., Erbs, G., Newman, M.A., Petersen, M., and Mundy, J.** (2016). An innate immunity pathway in the moss *Physcomitrella patens*. *Plant Cell* **28**, 1328-1342.
- Burgess, J., and Linstead, P.** (1981). Studies on the growth and development of protoplasts of the moss, *Physcomitrella patens*, and its control by light. *Planta* **151**, 331-338.
- Burkart, G.M., Baskin, T.I., and Bezanilla, M.** (2015). A family of ROP proteins that suppresses actin dynamics, and is essential for polarized growth and cell adhesion. *J Cell Sci* **128**, 2553-2564.
- Cai, C., Henty-Ridilla, J.L., Szymanski, D.B., and Staiger, C.J.** (2014). Arabidopsis myosin XI: a motor rules the tracks. *Plant Physiology* **166**, 1359-1370.
- Cai, G., and Cresti, M.** (2010). Microtubule motors and pollen tube growth—still an open question. *Protoplasma* **247**, 131-143.
- Campas, O., Rojas, E., Dumais, J., and Mahadevan, L.** (2012). Strategies for cell shape control in tip-growing cells. *Am J Bot* **99**, 1577-1582.
- Campàs, O., and Mahadevan, L.** (2009). Shape and dynamics of tip-growing cells. *Current Biology* **19**, 2102-2107.
- Cao, X.Q., Jiang, Z.H., Yi, Y.Y., Yang, Y., Ke, L.P., Pei, Z.M., and Zhu, S.** (2017). Biotic and abiotic stresses activate different Ca²⁺ permeable channels in *Arabidopsis*. *Front Plant Sci* **8**, 83.
- Cao, Y., Liang, Y., Tanaka, K., Nguyen, C.T., Jędrzejczak, R.P., Joachimiak, A., and Stacey, G.** (2014). The kinase LYK5 is a major chitin receptor in *Arabidopsis* and forms a chitin-induced complex with related kinase CERK1. *Elife* **3**.
- Cárdenas, L.** (2009). New findings in the mechanisms regulating polar growth in root hair cells. *Plant signaling & behavior* **4**, 4-8.
- Chakshusmathi, G., Mondal, K., Lakshmi, G.S., Singh, G., Roy, A., Ch, R.B., Madhusudhanan, S., and Varadarajan, R.** (2004). Design of temperature-sensitive mutants solely from amino acid sequence. *Proc Natl Acad Sci U S A* **101**, 7925-7930.
- Chang, F., Drubin, D., and Nurse, P.** (1997). cdc12p, a protein required for cytokinesis in fission yeast, is a component of the cell division ring and interacts with profilin. *J Cell Biol* **137**, 169-182.
- Chen, C.Y., Wong, E.I., Vidali, L., Estavillo, A., Hepler, P.K., Wu, H.M., and Cheung, A.Y.** (2002). The regulation of actin organization by actin-depolymerizing factor in elongating pollen tubes. *Plant Cell* **14**, 2175-2190.
- Chen, T.-W., Wardill, T.J., Sun, Y., Pulver, S.R., Renninger, S.L., Baohan, A., Schreiter, E.R., Kerr, R.A., Orger, M.B., Jayaraman, V., Looger, L.L., Svoboda, K., and Kim, D.S.** (2013). Ultrasensitive fluorescent proteins for imaging neuronal activity. *Nature* **499**, 295.
- Cheney, R.E., O'Shea, M.K., Heuser, J.E., Coelho, M.V., Wolenski, J.S., Espreafico, E.M., Forscher, P., Larson, R.E., and Mooseker, M.S.** (1993). Brain myosin-V is a two-headed unconventional myosin with motor activity. *Cell* **75**, 13-23.
- Cheung, A.Y., and Wu, H.M.** (2008). Structural and signaling networks for the polar cell growth machinery in pollen tubes. *Annual Review of Plant Biology* **59**, 547-572.
- Chiou, J.-g., Balasubramanian, M.K., and Lew, D.J.** (2017). Cell polarity in yeast. *Annual review of cell and developmental biology* **33**, 77-101.
- Chisholm, S.T., Coaker, G., Day, B., and Staskawicz, B.J.** (2006). Host-microbe interactions: shaping the evolution of the plant immune response. *Cell* **124**, 803-814.

- Cho, S.H., Chung, Y.S., Cho, S.K., Rim, Y.W., and Shin, J.S.** (1999). Particle bombardment mediated transformation and GFP expression in the moss *Physcomitrella patens*. *Mol Cells* **9**, 14-19.
- Cole, L., Orlovich, D.A., and Ashford, A.E.** (1998). Structure, function, and motility of vacuoles in filamentous fungi. *Fungal Genetics and Biology* **24**, 86-100.
- Collonnier, C., Guyon-Debast, A., Maclot, F., Mara, K., Charlot, F., and Nogue, F.** (2017). Towards mastering CRISPR-induced gene knock-in in plants: Survey of key features and focus on the model *Physcomitrella patens*. *Methods* **121-122**, 103-117.
- Corwin, J.A., and Kliebenstein, D.J.** (2017). Quantitative Resistance: More Than Just Perception of a Pathogen. *Plant Cell* **29**, 655-665.
- Cove, D.** (2005). The moss *Physcomitrella patens*. *Annu Rev Genet* **39**, 339-358.
- Cove, D.J., and Knight, C.D.** (1993). The Moss *Physcomitrella patens*, a Model System with Potential for the Study of Plant Reproduction. *Plant Cell* **5**, 1483-1488.
- Cove, D.J., Kammerer, W., Knight, C.D., Leech, M.J., Martin, C.R., and Wang, T.L.** (1991). Developmental genetic studies of the moss, *Physcomitrella patens*. *Symp Soc Exp Biol* **45**, 31-43.
- Cui, H., Tsuda, K., and Parker, J.E.** (2015). Effector-triggered immunity: from pathogen perception to robust defense. *Annual review of plant biology* **66**, 487-511.
- Cui, S., Suzaki, T., Tominaga-Wada, R., and Yoshida, S.** (2018). Regulation and functional diversification of root hairs. In *Seminars in cell & developmental biology* (Elsevier), pp. 115-122.
- Davin, L.B., and Lewis, N.G.** (2000). Dirigent proteins and dirigent sites explain the mystery of specificity of radical precursor coupling in lignan and lignin biosynthesis. *Plant Physiology* **123**, 453-462.
- Ding, X., Pervere, L.M., Bascom, C., Jr., Bibeau, J.P., Khurana, S., Butt, A.M., Orr, R.G., Flaherty, P.J., Bezanilla, M., and Vidali, L.** (2018). Conditional genetic screen in *Physcomitrella patens* reveals a novel microtubule depolymerizing-end-tracking protein. *PLoS Genet* **14**, e1007221.
- Diouf, J., and Sheeran, J.** (2010). The State of Food Insecurity in the World: Addressing food insecurity in protracted crises. World Food Program (WFP) and Food and Agriculture Organization of the United Nations (FAO) Joint Report.
- Donovan, K.W., and Bretscher, A.** (2012). Myosin-V Is Activated by Binding Secretory Cargo and Released in Coordination with Rab/Exocyst Function. *Developmental Cell* **23**, 769-781.
- Doonan, J.H., Cove, D.J., and Lloyd, C.W.** (1985). Immunofluorescence microscopy of microtubules in intact cell lineages of the moss, *Physcomitrella patens*. I. Normal and CIPC-treated tip cells. *J Cell Sci* **75**, 131-147.
- Doonan, J.H., Cove, D.J., and Lloyd, C.W.** (1988). Microtubules and microfilaments in tip growth: evidence that microtubules impose polarity on protonemal growth in *Physcomitrella patens*. *J Cell Sci* **89**, 533-540.
- Dos Remedios, C., Chhabra, D., Kekic, M., Dedova, I., Tsubakihara, M., Berry, D., and Nosworthy, N.** (2003). Actin binding proteins: regulation of cytoskeletal microfilaments. *Physiological reviews*.
- Dumais, J., Long, S.R., and Shaw, S.L.** (2004). The mechanics of surface expansion anisotropy in *Medicago truncatula* root hairs. *Plant Physiology* **136**, 3266-3275.
- Edel, K.H., Marchadier, E., Brownlee, C., Kudla, J., and Hetherington, A.M.** (2017). The evolution of calcium-based signalling in plants. *Current Biology* **27**, R667-R679.
- Edelstein, A.D., Tsuchida, M.A., Amodaj, N., Pinkard, H., Vale, R.D., and Stuurman, N.** (2014). Advanced methods of microscope control using μ Manager software. *J Biol Methods* **1**.
- Eklund, D.M., Svensson, E.M., and Kost, B.** (2010). *Physcomitrella patens*: a model to investigate the role of RAC/ROP GTPase signalling in tip growth. *J Exp Bot* **61**, 1917-1937.
- Elliott, L., Moore, I., and Kirchhelle, C.** (2020). Spatio-temporal control of post-Golgi exocytic trafficking in plants. *J Cell Sci* **133**.
- Finka, A., Schaefer, D.G., Saidi, Y., Goloubinoff, P., and Zryd, J.P.** (2007). *In vivo* visualization of F-actin structures during the development of the moss *Physcomitrella patens*. *New Phytol* **174**, 63-76.

- Foley, S.J.** (2019). Structural and Spatial Regulation of Arl8: myosinXI Interactions in *Physcomitrella patens* Polarized Tip Growth & Potential Diagnostic Markers Associated with Parkinson's Disease.
- Fu, Y., Wu, G., and Yang, Z.** (2001). Rop GTPase-dependent dynamics of tip-localized F-actin controls tip growth in pollen tubes. *J Cell Biol* **152**, 1019-1032.
- Furt, F., Lemoi, K., Tüzel, E., and Vidali, L.** (2012). Quantitative analysis of organelle distribution and dynamics in *Physcomitrella patens* protonemal cells. *BMC Plant Biology* **12**, 70.
- Furt, F., Liu, Y.C., Bibeau, J.P., Tüzel, E., and Vidali, L.** (2013). Apical myosin XI anticipates F-actin during polarized growth of *Physcomitrella patens* cells. *Plant J* **73**, 417-428.
- Galotto, G., Bibeau, J.P., and Vidali, L.** (2019). Automated image acquisition and morphological analysis of cell growth mutants in *Physcomitrella patens*. *Methods Mol Biol* **1992**, 307-322.
- Geitmann, A., and Nebenfuhr, A.** (2015). Navigating the plant cell: intracellular transport logistics in the green kingdom. *Mol Biol Cell* **26**, 3373-3378.
- Gibbon, B.C., Kovar, D.R., and Staiger, C.J.** (1999). Latrunculin B has different effects on pollen germination and tube growth. *Plant Cell* **11**, 2349-2363.
- Gilbert, L.A., Larson, M.H., Morsut, L., Liu, Z., Brar, G.A., Torres, S.E., Stern-Ginossar, N., Brandman, O., Whitehead, E.H., and Doudna, J.A.** (2013). CRISPR-mediated modular RNA-guided regulation of transcription in eukaryotes. *Cell* **154**, 442-451.
- Gomez-Gomez, L., and Boller, T.** (2000). FLS2: an LRR receptor-like kinase involved in the perception of the bacterial elicitor flagellin in *Arabidopsis*. *Mol Cell* **5**, 1003-1011.
- Gossen, M., Freundlieb, S., Bender, G., Muller, G., Hillen, W., and Bujard, H.** (1995). Transcriptional activation by tetracyclines in mammalian cells. *Science* **268**, 1766-1769.
- Gouin, E., Welch, M.D., and Cossart, P.** (2005). Actin-based motility of intracellular pathogens. *Curr Opin Microbiol* **8**, 35-45.
- Gourlay, C.W., Carpp, L.N., Timpson, P., Winder, S.J., and Ayscough, K.R.** (2004). A role for the actin cytoskeleton in cell death and aging in yeast. *The Journal of cell biology* **164**, 803-809.
- Grosshans, B.L., Ortiz, D., and Novick, P.** (2006). Rabs and their effectors: achieving specificity in membrane traffic. *Proc Natl Acad Sci U S A* **103**, 11821-11827.
- Gu, Y., Li, S., Lord, E.M., and Yang, Z.** (2006). Members of a novel class of *Arabidopsis* Rho guanine nucleotide exchange factors control Rho GTPase-dependent polar growth. *The Plant Cell* **18**, 366-381.
- Gu, Y., Fu, Y., Dowd, P., Li, S., Vernoud, V., Gilroy, S., and Yang, Z.** (2005). A Rho family GTPase controls actin dynamics and tip growth via two counteracting downstream pathways in pollen tubes. *J Cell Biol* **169**, 127-138.
- Gunsalus, K.C., and Piano, F.** (2005). RNAi as a tool to study cell biology: building the genome-phenome bridge. *Current opinion in cell biology* **17**, 3-8.
- Guo, H.S., Fei, J.F., Xie, Q., and Chua, N.H.** (2003). A chemical-regulated inducible RNAi system in plants. *The Plant Journal* **34**, 383-392.
- Hardham, A.R., Jones, D.A., and Takemoto, D.** (2007). Cytoskeleton and cell wall function in penetration resistance. *Curr Opin Plant Biol* **10**, 342-348.
- Harries, P.A., Pan, A., and Quatrano, R.S.** (2005). Actin-related protein2/3 complex component ARPC1 is required for proper cell morphogenesis and polarized cell growth in *Physcomitrella patens*. *Plant Cell* **17**, 2327-2339.
- Hartwell, L.H.** (1967). Macromolecule synthesis in temperature-sensitive mutants of yeast. *J Bacteriol* **93**, 1662-1670.
- Hashimoto, K., Igarashi, H., Mano, S., Nishimura, M., Shimmen, T., and Yokota, E.** (2005). Peroxisomal localization of a myosin XI isoform in *Arabidopsis thaliana*. *Plant and Cell Physiology* **46**, 782-789.
- Heasman, J., Kofron, M., and Wylie, C.** (2000). β Catenin signaling activity dissected in the early *Xenopus* embryo: a novel antisense approach. *Developmental biology* **222**, 124-134.

- Henty-Ridilla, J.L., Shimono, M., Li, J., Chang, J.H., Day, B., and Staiger, C.J.** (2013). The plant actin cytoskeleton responds to signals from microbe-associated molecular patterns. *PLoS Pathog* **9**, e1003290.
- Hepler, P.K.** (2005). Calcium: a central regulator of plant growth and development. *The Plant Cell* **17**, 2142-2155.
- Hepler, P.K.** (2016). The cytoskeleton and its regulation by calcium and protons. *Plant Physiology* **170**, 3-22.
- Hepler, P.K., Vidali, L., and Cheung, A.Y.** (2001). Polarized cell growth in higher plants. *Annual Review of Cell and Developmental Biology* **17**, 159-187.
- Heslop-Harrison, J., and Heslop-Harrison, Y.** (1982). The growth of the grass pollen tube: 1. Characteristics of the polysaccharide particles ("P-particles") associated with apical growth. *Protoplasma* **112**, 71-80.
- Higaki, T., Kurusu, T., Hasezawa, S., and Kuchitsu, K.** (2011). Dynamic intracellular reorganization of cytoskeletons and the vacuole in defense responses and hypersensitive cell death in plants. *J Plant Res* **124**, 315-324.
- Higaki, T., Kutsuna, N., Okubo, E., Sano, T., and Hasezawa, S.** (2006). Actin microfilaments regulate vacuolar structures and dynamics: dual observation of actin microfilaments and vacuolar membrane in living tobacco BY-2 cells. *Plant and Cell Physiology* **47**, 839-852.
- Hiwatashi, Y., Sato, Y., and Doonan, J.H.** (2014). Kinesins have a dual function in organizing microtubules during both tip growth and cytokinesis in *Physcomitrella patens*. *Plant Cell* **26**, 1256-1266.
- Horikawa, K., Yamada, Y., Matsuda, T., Kobayashi, K., Hashimoto, M., Matsu-ura, T., Miyawaki, A., Michikawa, T., Mikoshiba, K., and Nagai, T.** (2010). Spontaneous network activity visualized by ultrasensitive Ca(2+) indicators, yellow Cameleon-Nano. *Nat Methods* **7**, 729-732.
- Housden, B.E., Muhar, M., Gemberling, M., Gersbach, C.A., Stainier, D.Y., Seydoux, G., Mohr, S.E., Zuber, J., and Perrimon, N.** (2017). Loss-of-function genetic tools for animal models: cross-species and cross-platform differences. *Nature Reviews Genetics* **18**, 24-40.
- Huang, S., Blanchoin, L., Chaudhry, F., Franklin-Tong, V.E., and Staiger, C.J.** (2004). A gelsolin-like protein from *Papaver rhoeas* pollen (PrABP80) stimulates calcium-regulated severing and depolymerization of actin filaments. *Journal of Biological Chemistry* **279**, 23364-23375.
- Hutchison, H.T., Hartwell, L.H., and McLaughlin, C.S.** (1969). Temperature-sensitive yeast mutant defective in ribonucleic acid production. *Journal of Bacteriology* **99**, 807-814.
- Hwang, J.U., Gu, Y., Lee, Y.J., and Yang, Z.B.** (2005). Oscillatory ROP GTPase activation leads the oscillatory polarized growth of pollen tubes. *Molecular Biology of the Cell* **16**, 5385-5399.
- Idilli, A.I., Morandini, P., Onelli, E., Rodighiero, S., Caccianiga, M., and Moscatelli, A.** (2013). Microtubule depolymerization affects endocytosis and exocytosis in the tip and influences endosome movement in tobacco pollen tubes. *Molecular plant* **6**, 1109-1130.
- Ito, K., Ren, J., and Fujita, T.** (2014). Conserved function of Rho-related Rop/RAC GTPase signaling in regulation of cell polarity in *Physcomitrella patens*. *Gene* **544**, 241-247.
- Jásik, J., Mičičeta, K., Siao, W., Voigt, B., Stuchlík, S., Schmelzer, E., Turňa, J., and Baluška, F.** (2016). Actin3 promoter reveals undulating F-actin bundles at shanks and dynamic F-actin meshworks at tips of tip-growing pollen tubes. *Plant signaling & behavior* **11**, e1146845.
- Jin, Y., Sultana, A., Gandhi, P., Franklin, E., Hamamoto, S., Khan, A.R., Munson, M., Schekman, R., and Weisman, L.S.** (2011). Myosin V transports secretory vesicles via a Rab GTPase cascade and interaction with the exocyst complex. *Dev Cell* **21**, 1156-1170.
- Johnson, M.A., Harper, J.F., and Palanivelu, R.** (2019). A fruitful journey: pollen tube navigation from germination to fertilization. *Annual review of plant biology* **70**, 809-837.
- Jungk, A.** (2001). Root hairs and the acquisition of plant nutrients from soil. *Journal of Plant Nutrition and Soil Science-Zeitschrift Fur Pflanzenernahrung Und Bodenkunde* **164**, 121-129.

- Kaku, H., Nishizawa, Y., Ishii-Minami, N., Akimoto-Tomiya, C., Dohmae, N., Takio, K., Minami, E., and Shibuya, N.** (2006). Plant cells recognize chitin fragments for defense signaling through a plasma membrane receptor. *Proceedings of the National Academy of Sciences* **103**, 11086-11091.
- Keinath, N.F., Waadt, R., Brugman, R., Schroeder, J.I., Grossmann, G., Schumacher, K., and Krebs, M.** (2015). Live cell imaging with R-GECO1 sheds light on flg22- and chitin-induced transient $[Ca^{2+}]_{cyt}$ patterns in l. *Mol Plant* **8**, 1188-1200.
- Ketelaar, T.** (2013). The actin cytoskeleton in root hairs: all is fine at the tip. *Current Opinion in Plant Biology* **16**, 749-756.
- Ketelaar, T., de Ruijter, N.C.A., and Emons, A.M.C.** (2003). Unstable F-actin specifies the area and microtubule direction of cell expansion in *Arabidopsis* root hairs. *Plant Cell* **15**, 285-292.
- Kohno, T., and Shimmen, T.** (1988). Accelerated sliding of pollen tube organelles along Characeae actin bundles regulated by Ca^{2+} . *The Journal of cell biology* **106**, 1539-1543.
- Korasick, D.A., McMichael, C., Walker, K.A., Anderson, J.C., Bednarek, S.Y., and Heese, A.** (2010). Novel functions of Stomatal Cytokinesis-Defective 1 (SCD1) in innate immune responses against bacteria. *J Biol Chem* **285**, 23342-23350.
- Kost, B.** (2008). Spatial control of Rho (Rac-Rop) signaling in tip-growing plant cells. *Trends in cell biology* **18**, 119-127.
- Kost, B., Spielhofer, P., and Chua, N.H.** (1998). A GFP-mouse talin fusion protein labels plant actin filaments in vivo and visualizes the actin cytoskeleton in growing pollen tubes. *Plant J* **16**, 393-401.
- Kost, B., Lemichez, E., Spielhofer, P., Hong, Y., Tolia, K., Carpenter, C., and Chua, N.H.** (1999). Rac homologues and compartmentalized phosphatidylinositol 4,5-bisphosphate act in a common pathway to regulate polar pollen tube growth. *Journal of Cell Biology* **145**, 317-330.
- Kovar, D.R., Drobak, B.K., and Staiger, C.J.** (2000). Maize profilin isoforms are functionally distinct. *Plant Cell* **12**, 583-598.
- Kunze, G., Zipfel, C., Robatzek, S., Niehaus, K., Boller, T., and Felix, G.** (2004). The N terminus of bacterial elongation factor Tu elicits innate immunity in *Arabidopsis* plants. *Plant Cell* **16**, 3496-3507.
- Kutsuna, N., Kumagai, F., Sato, M.H., and Hasezawa, S.** (2003). Three-dimensional reconstruction of tubular structure of vacuolar membrane throughout mitosis in living tobacco cells. *Plant and cell physiology* **44**, 1045-1054.
- Kyte, J., and Doolittle, R.F.** (1982). A simple method for displaying the hydropathic character of a protein. *J Mol Biol* **157**, 105-132.
- Lane, D.R., Wiedemeier, A., Peng, L., Hofte, H., Vernhettes, S., Desprez, T., Hocart, C.H., Birch, R.J., Baskin, T.I., Burn, J.E., Arioli, T., Betzner, A.S., and Williamson, R.E.** (2001). Temperature-sensitive alleles of RSW2 link the KORRIGAN endo-1,4-beta-glucanase to cellulose synthesis and cytokinesis in *Arabidopsis*. *Plant Physiol* **126**, 278-288.
- Lang, D., Zimmer, A.D., Rensing, S.A., and Reski, R.** (2008). Exploring plant biodiversity: the *Physcomitrella* genome and beyond. *Trends Plant Sci* **13**, 542-549.
- Le Bail, A., Schulmeister, S., Perroud, P.F., Ntefidou, M., Rensing, S.A., and Kost, B.** (2019). Analysis of the Localization of Fluorescent PpROP1 and PpROP-GEF4 Fusion Proteins in Moss Protonemata Based on Genomic "Knock-In" and Estradiol-Titratable Expression. *Front Plant Sci* **10**, 456.
- Lee, Y.J., Szumlanski, A., Nielsen, E., and Yang, Z.B.** (2008). Rho-GTPase-dependent filamentous actin dynamics coordinate vesicle targeting and exocytosis during tip growth. *Journal of Cell Biology* **181**, 1155-1168.
- Lehtonen, M.T., Akita, M., Frank, W., Reski, R., and Valkonen, J.P.** (2012). Involvement of a class III peroxidase and the mitochondrial protein TSPO in oxidative burst upon treatment of moss plants with a fungal elicitor. *Mol Plant Microbe Interact* **25**, 363-371.

- Li, X.-d., Jung, H.S., Mabuchi, K., Craig, R., and Ikebe, M.** (2006). The globular tail domain of myosin Va functions as an inhibitor of the myosin Va motor. *Journal of Biological Chemistry* **281**, 21789-21798.
- Li, Z., Vizeacoumar, F.J., Bahr, S., Li, J., Warringer, J., Vizeacoumar, F.S., Min, R., VanderSluis, B., Bellay, J., and DeVit, M.** (2011). Systematic exploration of essential yeast gene function with temperature-sensitive mutants. *Nature biotechnology* **29**, 361-367.
- Lin, Y., Wang, Y., Zhu, J., and Yang, Z.** (1996). Localization of a Rho GTPase implies a role in tip growth and movement of the generative cell in pollen tubes. *The Plant Cell* **8**, 293-303.
- Lipatova, Z., Tokarev, A.A., Jin, Y., Mulholland, J., Weisman, L.S., and Segev, N.** (2008). Direct Interaction between a Myosin V Motor and the Rab GTPases Ypt31/32 Is Required for Polarized Secretion. *Molecular Biology of the Cell* **19**, 4177-4187.
- Liu, C., Zhang, Y., and Ren, H.** (2018). Actin polymerization mediated by AtFH5 directs the polarity establishment and vesicle trafficking for pollen germination in *Arabidopsis*. *Mol Plant* **11**, 1389-1399.
- Liu, Y.-C., and Vidali, L.** (2011a). Efficient Polyethylene Glycol (PEG) Mediated Transformation of the Moss *Physcomitrella patens*. *JoVE*, e2560.
- Liu, Y.C., and Vidali, L.** (2011b). Efficient polyethylene glycol (PEG) mediated transformation of the moss *Physcomitrella patens*. *J Vis Exp* **50**, e2560.
- Loisel, T.P., Boujemaa, R., Pantaloni, D., and Carlier, M.-F.** (1999). Reconstitution of actin-based motility of *Listeria* and *Shigella* using pure proteins. *Nature* **401**, 613-616.
- Love, M., Anders, S., and Huber, M.** (2014). Differential gene expression analysis based on the negative binomial distribution. *Genome Biol* **15**, 550.
- Lovy-Wheeler, A., Wilsen, K.L., Baskin, T.I., and Hepler, P.K.** (2005). Enhanced fixation reveals the apical cortical fringe of actin filaments as a consistent feature of the pollen tube. *Planta* **221**, 95-104.
- Lovy-Wheeler, A., Cardenas, L., Kunkel, J.G., and Hepler, P.K.** (2007). Differential organelle movement on the actin cytoskeleton in lily pollen tubes. *Cell Motil Cytoskeleton* **64**, 217-232.
- Ma, Y., Zhao, Y., and Berkowitz, G.A.** (2017). Intracellular Ca²⁺ is important for flagellin-triggered defense in *Arabidopsis* and involves inositol polyphosphate signaling. *Journal of Experimental Botany* **68**, 3617-3628.
- Macho, A.P., and Zipfel, C.** (2014). Plant PRRs and the activation of innate immune signaling. *Molecular cell* **54**, 263-272.
- Madison, S.L., Buchanan, M.L., Glass, J.D., McClain, T.F., Park, E., and Nebenfuhr, A.** (2015). Class XI myosins move specific organelles in pollen tubes and are required for normal fertility and pollen tube growth in *Arabidopsis*. *Plant Physiology* **169**, 1946-1960.
- Manghwar, H., Lindsey, K., Zhang, X., and Jin, S.** (2019). CRISPR/Cas system: recent advances and future prospects for genome editing. *Trends in plant science* **24**, 1102-1125.
- Mann, C., Buhler, J.M., Treich, I., and Sentenac, A.** (1987). RPC40, a unique gene for a subunit shared between yeast RNA polymerases A and C. *Cell* **48**, 627-637.
- Marty, F.** (1999). Plant vacuoles. *Plant Cell* **11**, 587-600.
- Masclaux, F., Charpentreau, M., Takahashi, T., Pont-Lezica, R., and Galaud, J.-P.** (2004). Gene silencing using a heat-inducible RNAi system in *Arabidopsis*. *Biochemical and biophysical research communications* **321**, 364-369.
- Mayers, J.R., Hu, T., Wang, C., Cardenas, J.J., Tan, Y., Pan, J., and Bednarek, S.Y.** (2017). SCD1 and SCD2 Form a Complex That Functions with the Exocyst and RabE1 in Exocytosis and Cytokinesis. *Plant Cell* **29**, 2610-2625.
- Meinke, D.W., Cherry, J.M., Dean, C., Rounsley, S.D., and Koornneef, M.** (1998). *Arabidopsis thaliana*: a model plant for genome analysis. *Science* **282**, 662-682.

- Messerli, M., and Robinson, K.R.** (1997). Tip localized Ca²⁺ pulses are coincident with peak pulsatile growth rates in pollen tubes of *Lilium longiflorum*. *Journal of Cell Science* **110**, 1269-1278.
- Messerli, M.A., Creton, R., Jaffe, L.F., and Robinson, K.R.** (2000). Periodic increases in elongation rate precede increases in cytosolic Ca²⁺ during pollen tube growth. *Developmental Biology* **222**, 84-98.
- Michard, E., Dias, P., and Feijó, J.A.** (2008). Tobacco pollen tubes as cellular models for ion dynamics: improved spatial and temporal resolution of extracellular flux and free cytosolic concentration of calcium and protons using pHluorin and YC3.1 CaMeleon. *Sexual Plant Reproduction* **21**, 169-181.
- Michard, E., Simon, A.A., Tavares, B., Wudick, M.M., and Feijó, J.A.** (2016). Signaling with ions: the keystone for apical cell growth and morphogenesis in pollen tubes. *Plant Physiology*.
- Miya, A., Albert, P., Shinya, T., Desaki, Y., Ichimura, K., Shirasu, K., Narusaka, Y., Kawakami, N., Kaku, H., and Shibuya, N.** (2007). CERK1, a LysM receptor kinase, is essential for chitin elicitor signaling in *Arabidopsis*. *Proceedings of the National Academy of Sciences* **104**, 19613-19618.
- Miyawaki, A., Llopis, J., Heim, R., McCaffery, J.M., Adams, J.A., Ikura, M., and Tsien, R.Y.** (1997). Fluorescent indicators for Ca²⁺ based on green fluorescent proteins and calmodulin. *Nature* **388**, 882-887.
- Molendijk, A.J., Ruperti, B., and Palme, K.** (2004). Small GTPases in vesicle trafficking. *Current opinion in plant biology* **7**, 694-700.
- Monshausen, G.B., Messerli, M.A., and Gilroy, S.** (2008). Imaging of the Yellow Cameleon 3.6 indicator reveals that elevations in cytosolic Ca²⁺ follow oscillating increases in growth in root hairs of *Arabidopsis*. *Plant Physiology* **147**, 1690-1698.
- Monshausen, G.B., Bibikova, T.N., Messerli, M.A., Shi, C., and Gilroy, S.** (2007). Oscillations in extracellular pH and reactive oxygen species modulate tip growth of *Arabidopsis* root hairs. *Proceedings of the National Academy of Sciences, USA* **104**, 20996-21001.
- Mooseker, M.S., and Cheney, R.E.** (1995). Unconventional myosins. *Annu Rev Cell Dev Biol* **11**, 633-675.
- Nagawa, S., Xu, T., and Yang, Z.** (2010). RHO GTPase in plants: Conservation and invention of regulators and effectors. *Small Gtpases* **1**, 78-88.
- Nakai, J., Ohkura, M., and Imoto, K.** (2001). A high signal-to-noise Ca²⁺ probe composed of a single green fluorescent protein. *Nat Biotechnol* **19**, 137-141.
- Nakaoka, Y., Miki, T., Fujioka, R., Uehara, R., Tomioka, A., Obuse, C., Kubo, M., Hiwatashi, Y., and Goshima, G.** (2012). An inducible RNA interference system in *Physcomitrella patens* reveals a dominant role of augmin in phragmoplast microtubule generation. *Plant Cell* **24**, 1478-1493.
- Nedelec, F., and Foethke, D.** (2007). Collective Langevin dynamics of flexible cytoskeletal fibers. *New Journal of Physics* **9**, 427.
- Nemudryi, A., Valetdinova, K., Medvedev, S., and Zakian, S.** (2014). TALEN and CRISPR/Cas genome editing systems: tools of discovery. *Acta Naturae (англоязычная версия)* **6**.
- Nishimura, K., Fukagawa, T., Takisawa, H., Kakimoto, T., and Kanemaki, M.** (2009). An auxin-based degron system for the rapid depletion of proteins in nonplant cells. *Nature methods* **6**, 917-922.
- Nishiyama, T., Fujita, T., Shin-I, T., Seki, M., Nishide, H., Uchiyama, I., Kamiya, A., Carninci, P., Hayashizaki, Y., Shinozaki, K., Kohara, Y., and Hasebe, M.** (2003). Comparative genomics of *Physcomitrella patens* gametophytic transcriptome and *Arabidopsis thaliana*: Implication for land plant evolution. *Proceedings of the National Academy of Sciences of the United States of America* **100**, 8007-8012.
- Nolen, B., Tomasevic, N., Russell, A., Pierce, D., Jia, Z., McCormick, C., Hartman, J., Sakowicz, R., and Pollard, T.** (2009). Characterization of two classes of small molecule inhibitors of Arp2/3 complex. *Nature* **460**, 1031-1034.
- Novick, P.** (2016). Regulation of membrane traffic by Rab GEF and GAP cascades. *Small GTPases* **7**, 252-256.

- Oda, Y., Hirata, A., Sano, T., Fujita, T., Hiwatashi, Y., Sato, Y., Kadota, A., Hasebe, M., and Hasezawa, S. (2009). Microtubules regulate dynamic organization of vacuoles in *Physcomitrella patens*. *Plant Cell Physiol* **50**, 855-868.
- Ojangu, E.-L., Ilau, B., Tanner, K., Talts, K., Ihoma, E., Dolja, V.V., Paves, H., and Truve, E. (2018). Class XI myosins contribute to auxin response and senescence-induced cell death in *Arabidopsis*. *Frontiers in plant science* **9**, 1570.
- Ojangu, E.L., Järve, K., Paves, H., and Truve, E. (2007). *Arabidopsis thaliana* myosin XIK is involved in root hair as well as trichome morphogenesis on stems and leaves. *Protoplasma* **230**, 193-202.
- Oliver, J.P., Castro, A., Gaggero, C., Cascon, T., Schmelz, E.A., Castresana, C., and de Leon, I.P. (2009). *Pythium* infection activates conserved plant defense responses in mosses. *Planta* **230**, 569-579.
- Orr, R.G., Cheng, X., Vidali, L., and Bezanilla, M. (2020a). Orchestrating cell morphology from the inside out - using polarized cell expansion in plants as a model. *Curr Opin Cell Biol* **62**, 46-53.
- Orr, R.G., Foley, S.J., Galotto, G., Liu, B., and Vidali, L. (2020b). Robust survival-based RNAi using in tandem silencing of adenine phosphoribosyltransferase. *bioRxiv*, 2020.2004.2009.034132.
- Orr, R.G., Furt, F., Warner, E.L., Agar, E.M., Garbarino, J.M., Cabral, S.E., Dubuke, M.L., Butt, A.M., Munson, M., and Vidali, L. (2019). Myosin XI interacting with a RabE GTPase is required for polarized growth. *bioRxiv*, 617167.
- Ovecka, M., Lang, I., Baluska, F., Ismail, A., Illes, P., and Lichtscheidl, I.K. (2005). Endocytosis and vesicle trafficking during tip growth of root hairs. *Protoplasma* **226**, 39-54.
- Park, E., and Nebenfuhr, A. (2013). Myosin XIK of *Arabidopsis thaliana* accumulates at the root hair tip and is required for fast root hair growth. *PLoS One* **8**, e76745.
- Park, H.-O., and Bi, E. (2007). Central roles of small GTPases in the development of cell polarity in yeast and beyond. *Microbiology and Molecular Biology Reviews* **71**, 48-96.
- Peng, Y., van Wersch, R., and Zhang, Y. (2018). Convergent and divergent signaling in PAMP-triggered immunity and effector-triggered immunity. *Mol Plant Microbe Interact* **31**, 403-409.
- Peremyslov, V.V., Prokhnevsky, A.I., and Dolja, V.V. (2010). Class XI myosins are required for development, cell expansion, and F-Actin organization in *Arabidopsis*. *Plant Cell* **22**, 1883-1897.
- Peremyslov, V.V., Prokhnevsky, A.I., Avisar, D., and Dolja, V.V. (2008). Two class XI myosins function in organelle trafficking and root hair development in *Arabidopsis*. *Plant Physiology* **146**, 1109-1116.
- Peremyslov, V.V., Klocko, A.L., Fowler, J.E., and Dolja, V.V. (2012). *Arabidopsis* myosin XI-K localizes to the motile endomembrane vesicles associated with F-actin. *Frontiers in Plant Science* **3**, 184.
- Peremyslov, V.V., Mockler, T.C., Filichkin, S.A., Fox, S.E., Jaiswal, P., Makarova, K.S., Koonin, E.V., and Dolja, V.V. (2011). Expression, splicing, and evolution of the myosin gene family in plants. *Plant Physiol* **155**, 1191-1204.
- Perroud, P.F., and Quatrano, R.S. (2006). The role of ARPC4 in tip growth and alignment of the polar axis in filaments of *Physcomitrella patens*. *Cell Motil Cytoskeleton* **63**, 162-171.
- Pertea, M., Kim, D., Pertea, G.M., Leek, J.T., and Salzberg, S.L. (2016). Transcript-level expression analysis of RNA-seq experiments with HISAT, StringTie and Ballgown. *Nature protocols* **11**, 1650.
- Peter K. Hepler, Luis Vidali, and Cheung, A.Y. (2001). Polarized Cell Growth in Higher Plants. *Annual Review of Cell and Developmental Biology* **17**, 159-187.
- Pfeffer, S.R. (2017). Rab GTPases: master regulators that establish the secretory and endocytic pathways. *Molecular biology of the cell* **28**, 712-715.
- Pierson, E.S., Miller, D.D., Callaham, D.A., vanAken, J., Hackett, G., and Hepler, P.K. (1996). Tip-localized calcium entry fluctuates during pollen tube growth. *Developmental Biology* **174**, 160-173.
- Pollard, T.D. (2016). Actin and actin-binding proteins. *Cold Spring Harbor perspectives in biology* **8**, a018226.
- Ponce de Leon, I., and Montesano, M. (2017). Adaptation mechanisms in the evolution of moss defenses to microbes. *Front Plant Sci* **8**, 366.

- Ponce de Leon, I., Oliver, J.P., Castro, A., Gaggero, C., Bentancor, M., and Vidal, S. (2007).** *Erwinia carotovora* elicitors and *Botrytis cinerea* activate defense responses in *Physcomitrella patens*. *BMC Plant Biol* **7**, 52.
- Preibisch, S., Saalfeld, S., and Tomancak, P. (2009).** Globally optimal stitching of tiled 3D microscopic image acquisitions. *Bioinformatics* **25**, 1463-1465.
- Prokhnevsky, A.I., Peremyslov, V.V., and Dolja, V.V. (2008).** Overlapping functions of the four class XI myosins in *Arabidopsis* growth, root hair elongation, and organelle motility. *Proceedings of the National Academy of Sciences, USA* **105**, 19744-19749.
- Qin, Y., and Yang, Z. (2011).** Rapid tip growth: insights from pollen tubes. In *Seminars in cell & developmental biology* (Elsevier), pp. 816-824.
- Rensing, S.A., Goffinet, B., Meyberg, R., Wu, S.-Z., and Bezanilla, M. (2020).** The Moss *Physcomitrium (Physcomitrella) patens*: A Model Organism for Non-Seed Plants. *The Plant Cell* **32**, 1361-1376.
- Rensing, S.A., Lang, D., Zimmer, A.D., Terry, A., Salamov, A., Shapiro, H., Nishiyama, T., Perroud, P.F., Lindquist, E.A., Kamisugi, Y., Tanahashi, T., Sakakibara, K., Fujita, T., Oishi, K., Shin, I.T., Kuroki, Y., Toyoda, A., Suzuki, Y., Hashimoto, S., Yamaguchi, K., Sugano, S., Kohara, Y., Fujiyama, A., Anterola, A., Aoki, S., Ashton, N., Barbazuk, W.B., Barker, E., Bennetzen, J.L., Blankenship, R., Cho, S.H., Dutcher, S.K., Estelle, M., Fawcett, J.A., Gundlach, H., Hanada, K., Heyl, A., Hicks, K.A., Hughes, J., Lohr, M., Mayer, K., Melkozernov, A., Murata, T., Nelson, D.R., Pils, B., Prigge, M., Reiss, B., Renner, T., Rombauts, S., Rushton, P.J., Sanderfoot, A., Schween, G., Shiu, S.H., Stueber, K., Theodoulou, F.L., Tu, H., Van de Peer, Y., Verrier, P.J., Waters, E., Wood, A., Yang, L., Cove, D., Cuming, A.C., Hasebe, M., Lucas, S., Mishler, B.D., Reski, R., Grigoriev, I.V., Quatrano, R.S., and Boore, J.L. (2008).** The *Physcomitrella* genome reveals evolutionary insights into the conquest of land by plants. *Science* **319**, 64-69.
- Reski, R. (2018).** Quantitative moss cell biology. *Curr Opin Plant Biol* **46**, 39-47.
- Riedl, J., Crevenna, A.H., Kessenbrock, K., Yu, J.H., Neukirchen, D., Bista, M., Bradke, F., Jenne, D., Holak, T.A., Werb, Z., Sixt, M., and Wedlich-Soldner, R. (2008).** Lifeact: a versatile marker to visualize F-actin. *Nat Methods* **5**, 605-607.
- Rojas, E.R., Hotton, S., and Dumais, J. (2011).** Chemically mediated mechanical expansion of the pollen tube cell wall. *Biophys J* **101**, 1844-1853.
- Rounds, C.M., and Bezanilla, M. (2013).** Growth mechanisms in tip-growing plant cells. *Annual Review of Plant Biology*, Vol 64 **64**, 243-265.
- Rounds, C.M., Hepler, P.K., and Winship, L.J. (2014).** The apical actin fringe contributes to localized cell wall deposition and polarized growth in the lily pollen tube. *Plant Physiology* **166**, 139-151.
- Rutherford, S., and Moore, I. (2002).** The Arabidopsis Rab GTPase family: another enigma variation. *Curr Opin Plant Biol* **5**, 518-528.
- Ryan, J.M., and Nebenfuhr, A. (2018).** Update on Myosin Motors: Molecular Mechanisms and Physiological Functions. *Plant Physiol* **176**, 119-127.
- Sakamoto, K.M., Kim, K.B., Kumagai, A., Mercurio, F., Crews, C.M., and Deshaies, R.J. (2001).** Protacs: Chimeric molecules that target proteins to the Skp1–Cullin–F box complex for ubiquitination and degradation. *Proceedings of the National Academy of Sciences* **98**, 8554-8559.
- Schaefer, D.G., and Zryd, J.P. (1997).** Efficient gene targeting in the moss *Physcomitrella patens*. *Plant Journal* **11**, 1195-1206.
- Scheible, N., and McCubbin, A. (2019).** Signaling in Pollen Tube Growth: Beyond the Tip of the Polarity Iceberg. *Plants* **8**, 156.
- Scheuring, D., Schöller, M., Kleine-Vehn, J., and Löffke, C. (2015).** Vacuolar staining methods in plant cells. In *Plant cell expansion* (Springer), pp. 83-92.

- Scheuring, D., Lofke, C., Kruger, F., Kittelmann, M., Eisa, A., Hughes, L., Smith, R.S., Hawes, C., Schumacher, K., and Kleine-Vehn, J.** (2016). Actin-dependent vacuolar occupancy of the cell determines auxin-induced growth repression. *Proc Natl Acad Sci U S A* **113**, 452-457.
- Schindele, A., Dorn, A., and Puchta, H.** (2020). CRISPR/Cas brings plant biology and breeding into the fast lane. *Current opinion in biotechnology* **61**, 7-14.
- Schmidt, S.M., and Panstruga, R.** (2007). Cytoskeleton functions in plant–microbe interactions. *Physiological and Molecular Plant Pathology* **71**, 135-148.
- Schott, D., Ho, J., Pruynne, D., and Bretscher, A.** (1999). The COOH-terminal domain of Myo2p, a yeast myosin V, has a direct role in secretory vesicle targeting. *Journal of Cell Biology* **147**, 791-807.
- Schuh, M.** (2011). An actin-dependent mechanism for long-range vesicle transport. *Nat Cell Biol* **13**, 1431-1436.
- Seybold, H., Trempel, F., Ranf, S., Scheel, D., Romeis, T., and Lee, J.** (2014). Ca²⁺ signalling in plant immune response: from pattern recognition receptors to Ca²⁺ decoding mechanisms. *New Phytol* **204**, 782-790.
- Shaw, S.L., Dumais, J., and Long, S.R.** (2000). Cell surface expansion in polarly growing root hairs of *Medicago truncatula*. *Plant Physiology* **124**, 959-969.
- Sheahan, M.B., Staiger, C.J., Rose, R.J., and McCurdy, D.W.** (2004). A green fluorescent protein fusion to actin-binding domain 2 of *Arabidopsis* fimbrin highlights new features of a dynamic actin cytoskeleton in live plant cells. *Plant Physiol* **136**, 3968-3978.
- Shortle, D., and Botstein, D.** (1983). [31] Directed mutagenesis with sodium bisulfite. In *Methods in enzymology* (Elsevier), pp. 457-468.
- Shortle, D., Novick, P., and Botstein, D.** (1984). Construction and genetic characterization of temperature-sensitive mutant alleles of the yeast actin gene. *Proc Natl Acad Sci U S A* **81**, 4889-4893.
- Sieberer, B.J., Ketelaar, T., Esseling, J.J., and Emons, A.M.C.** (2005). Microtubules guide root hair tip growth. *New Phytologist* **167**, 711-719.
- Smertenko, A.P., Deeks, M.J., and Hussey, P.J.** (2010). Strategies of actin reorganisation in plant cells. *J Cell Sci* **123**, 3019-3028.
- Smith, L.G., and Oppenheimer, D.G.** (2005). Spatial control of cell expansion by the plant cytoskeleton. *Annual Review of Cell and Developmental Biology* **21**, 271-295.
- Smith, M.B., Li, H., Shen, T., Huang, X., Yusuf, E., and Vavylonis, D.** (2010). Segmentation and tracking of cytoskeletal filaments using open active contours. *Cytoskeleton* **67**, 693-705.
- Speth, E.B., Imboden, L., Hauck, P., and He, S.Y.** (2009). Subcellular localization and functional analysis of the *Arabidopsis* GTPase RabE. *Plant Physiol* **149**, 1824-1837.
- Staiger, C.J., Sheahan, M.B., Khurana, P., Wang, X., McCurdy, D.W., and Blanchoin, L.** (2009). Actin filament dynamics are dominated by rapid growth and severing activity in the *Arabidopsis* cortical array. *Journal of Cell Biology* **184**, 269-280.
- Storti, M., Costa, A., Golin, S., Zottini, M., Morosinotto, T., and Alboresi, A.** (2018). Systemic Calcium Wave Propagation in *Physcomitrella patens*. *Plant Cell Physiol*.
- Sun, H., Furt, F., and Vidali, L.** (2018). Myosin XI localizes at the mitotic spindle and along the cell plate during plant cell division in *Physcomitrella patens*. *Biochem Biophys Res Commun* **506**, 409-421.
- Suzuki, D.T., Piternick, L.K., Hayashi, S., Tarasoff, M., Baillie, D., and Erasmus, U.** (1967). Temperature-sensitive mutations in *Drosophila melanogaster*. I. Relative frequencies among gamma-ray and chemically induced sex-linked recessive lethals and semilethals. *Proc Natl Acad Sci U S A* **57**, 907-912.
- Syrovatkina, V., Alegre, K.O., Dey, R., and Huang, X.-Y.** (2016). Regulation, signaling, and physiological functions of G-proteins. *Journal of molecular biology* **428**, 3850-3868.
- Takagi, S., and Nagai, R.** (1986). Intracellular Ca²⁺ concentration and cytoplasmic streaming in *Vallisneria* mesophyll cells. *Plant and cell physiology* **27**, 953-959.

- Tang, F., Kauffman, E.J., Novak, J.L., Nau, J.J., Catlett, N.L., and Weisman, L.S.** (2003). Regulated degradation of a class V myosin receptor directs movement of the yeast vacuole. *Nature* **422**, 87-92.
- Thomas, S.G., Huang, S., Li, S., Staiger, C.J., and Franklin-Tong, V.E.** (2006). Actin depolymerization is sufficient to induce programmed cell death in self-incompatible pollen. *The Journal of cell biology* **174**, 221-229.
- Thor, K., Jiang, S., Michard, E., George, J., Scherzer, S., Huang, S., Dindas, J., Derbyshire, P., Leitão, N., and DeFalco, T.A.** (2020). The calcium-permeable channel OSCA1.3 regulates plant stomatal immunity. *Nature*, 1-8.
- Tominaga, M., Yokota, E., Vidali, L., Sonobe, S., Hepler, P.K., and Shimmen, T.** (2000). The role of plant villin in the organization of the actin cytoskeleton, cytoplasmic streaming and the architecture of the transvacuolar strand in root hair cells of *Hydrocharis*. *Planta* **210**, 836-843.
- Tominaga, M., Kojima, H., Yokota, E., Nakamori, R., Anson, M., Shimmen, T., and Oiwa, K.** (2012). Calcium-induced mechanical change in the neck domain alters the activity of plant myosin XI. *Journal of Biological Chemistry* **287**, 30711-30718.
- Tominaga, M., Kimura, A., Yokota, E., Haraguchi, T., Shimmen, T., Yamamoto, K., Nakano, A., and Ito, K.** (2013). Cytoplasmic streaming velocity as a plant size determinant. *Dev Cell* **27**, 345-352.
- Tominaga, M., Kojima, H., Yokota, E., Orii, H., Nakamori, R., Katayama, E., Anson, M., Shimmen, T., and Oiwa, K.** (2003). Higher plant myosin XI moves processively on actin with 35 nm steps at high velocity. *Embo J* **22**, 1263-1272.
- Toyota, M., Spencer, D., Sawai-Toyota, S., Jiaqi, W., Zhang, T., Koo, A.J., Howe, G.A., and Gilroy, S.** (2018). Glutamate triggers long-distance, calcium-based plant defense signaling. *Science* **361**, 1112-1115.
- Trybus, K.M.** (2008). Myosin V from head to tail. *Cell Mol Life Sci* **65**, 1378-1389.
- Ueda, H., Yokota, E., Kutsuna, N., Shimada, T., Tamura, K., Shimmen, T., Hasezawa, S., Dolja, V.V., and Hara-Nishimura, I.** (2010). Myosin-dependent endoplasmic reticulum motility and F-actin organization in plant cells. *Proc Natl Acad Sci U S A* **107**, 6894-6899.
- van Gisbergen, P.A., Li, M., Wu, S.Z., and Bezanilla, M.** (2012). Class II formin targeting to the cell cortex by binding PI(3,5)P(2) is essential for polarized growth. *J Cell Biol* **198**, 235-250.
- Varadarajan, R., Nagarajaram, H.A., and Ramakrishnan, C.** (1996). A procedure for the prediction of temperature-sensitive mutants of a globular protein based solely on the amino acid sequence. *Proc Natl Acad Sci U S A* **93**, 13908-13913.
- Verchot-Lubicz, J., and Goldstein, R.E.** (2010). Cytoplasmic streaming enables the distribution of molecules and vesicles in large plant cells. *Protoplasma* **240**, 99-107.
- Vidali, L., and Bezanilla, M.** (2012). *Physcomitrella patens*: a model for tip cell growth and differentiation. *Curr Opin Plant Biol* **15**, 625-631.
- Vidali, L., McKenna, S.T., and Hepler, P.K.** (2001). Actin polymerization is essential for pollen tube growth. *Molecular Biology of the Cell* **12**, 2534-2545.
- Vidali, L., Augustine, R.C., Kleinman, K.P., and Bezanilla, M.** (2007). Profilin is essential for tip growth in the moss *Physcomitrella patens*. *Plant Cell* **19**, 3705-3722.
- Vidali, L., Rounds, C.M., Hepler, P.K., and Bezanilla, M.** (2009a). Lifeact-mEGFP reveals a dynamic apical F-actin network in tip growing plant cells. *Plos One* **4**, e5744.
- Vidali, L., Augustine, R.C., Fay, S.N., Franco, P., Pattavina, K.A., and Bezanilla, M.** (2009b). Rapid screening for temperature-sensitive alleles in plants. *Plant Physiology* **151**, 506-514.
- Vidali, L., Burkart, G.M., Augustine, R.C., Kerdavid, E., Tüzel, E., and Bezanilla, M.** (2010). Myosin XI is essential for tip growth in *Physcomitrella patens*. *Plant Cell* **22**, 1868-1882.

- Vidali, L., van Gisbergen, P.A.C., Guerin, C., Franco, P., Li, M., Burkart, G.M., Augustine, R.C., Blanchoin, L., and Bezanilla, M. (2009c). Rapid formin-mediated actin-filament elongation is essential for polarized plant cell growth. *Proc Natl Acad Sci U S A* **106**, 13341-13346.
- Wang, Y.-F., Fan, L.-M., Zhang, W.-Z., Zhang, W., and Wu, W.-H. (2004). Ca²⁺-permeable channels in the plasma membrane of Arabidopsis pollen are regulated by actin microfilaments. *Plant Physiology* **136**, 3892-3904.
- Whittington, A.T., Vugrek, O., Wei, K.J., Hasenbein, N.G., Sugimoto, K., Rashbrooke, M.C., and Wasteneys, G.O. (2001). MOR1 is essential for organizing cortical microtubules in plants. *Nature* **411**, 610-613.
- Wiedemeier, A.M., Judy-March, J.E., Hocart, C.H., Wasteneys, G.O., Williamson, R.E., and Baskin, T.I. (2002). Mutant alleles of *Arabidopsis* RADIALLY SWOLLEN 4 and 7 reduce growth anisotropy without altering the transverse orientation of cortical microtubules or cellulose microfibrils. *Development* **129**, 4821-4830.
- Wu, G., Gu, Y., Li, S., and Yang, Z. (2001). A genome-wide analysis of Arabidopsis Rop-interactive CRIB motif-containing proteins that act as Rop GTPase targets. *The Plant Cell* **13**, 2841-2856.
- Wu, S., Scheible, W.R., Schindelasch, D., Van Den Daele, H., De Veylder, L., and Baskin, T.I. (2010). A conditional mutation in Arabidopsis thaliana separase induces chromosome non-disjunction, aberrant morphogenesis and cyclin B1;1 stability. *Development* **137**, 953-961.
- Wu, S.Z., and Bezanilla, M. (2018). Actin and microtubule cross talk mediates persistent polarized growth. *J Cell Biol* **217**, 3531-3544.
- Wymer, C.L., Bibikova, T.N., and Gilroy, S. (1997). Cytoplasmic free calcium distributions during the development of root hairs of Arabidopsis thaliana. *The Plant Journal* **12**, 427-439.
- Yalovsky, S., Bloch, D., Sorek, N., and Kost, B. (2008). Regulation of membrane trafficking, cytoskeleton dynamics, and cell polarity by ROP/RAC GTPases. *Plant Physiology* **147**, 1527-1543.
- Yang, G., Gao, P., Zhang, H., Huang, S., and Zheng, Z.-L. (2007). A mutation in MRH2 kinesin enhances the root hair tip growth defect caused by constitutively activated ROP2 small GTPase in Arabidopsis. *PLoS One* **2**, e1074.
- Yang, Z. (2002). Small GTPases: versatile signaling switches in plants. *The Plant Cell* **14**, S375-S388.
- Yokota, E., Muto, S., and Shimmen, T. (1999). Inhibitory regulation of higher-plant myosin by Ca²⁺ ions. *Plant Physiology* **119**, 231-240.
- Yokota, E., McDonald, A.R., Liu, B., Shimmen, T., and Palevitz, B.A. (1995). Localization of a 170kda Myosin Heavy-Chain in Plant-Cells. *Protoplasma* **185**, 178-187.
- Yokota, E., Ueda, S., Tamura, K., Orii, H., Uchi, S., Sonobe, S., Hara-Nishimura, I., and Shimmen, T. (2009). An isoform of myosin XI is responsible for the translocation of endoplasmic reticulum in tobacco cultured BY-2 cells. *Journal of Experimental Botany* **60**, 197-212.
- Young, M.D., Wakefield, M.J., Smyth, G.K., and Oshlack, A. (2010). Gene ontology analysis for RNA-seq: accounting for selection bias. *Genome Biol* **11**, R14.
- Yuan, F., Yang, H., Xue, Y., Kong, D., Ye, R., Li, C., Zhang, J., Theprungsirikul, L., Shrift, T., Krichilsky, B., Johnson, D.M., Swift, G.B., He, Y., Siedow, J.N., and Pei, Z.M. (2014). OSCA1 mediates osmotic-stress-evoked Ca²⁺ increases vital for osmosensing in Arabidopsis. *Nature* **514**, 367-371.
- Zerial, M., and McBride, H. (2001). Rab proteins as membrane organizers. *Nature Reviews Molecular Cell Biology* **2**, 107-117.
- Zhang, X.-H., Tee, L.Y., Wang, X.-G., Huang, Q.-S., and Yang, S.-H. (2015). Off-target effects in CRISPR/Cas9-mediated genome engineering. *Molecular Therapy-Nucleic Acids* **4**, e264.
- Zhang, X.C., Cannon, S.B., and Stacey, G. (2009). Evolutionary genomics of LysM genes in land plants. *BMC Evol Biol* **9**, 183.
- Zheng, Z.-L., and Yang, Z. (2000). The Rop GTPase: an emerging signaling switch in plants. *Plant molecular biology* **44**, 1-9.

- Zhu, L., Zhang, Y., Kang, E., Xu, Q., Wang, M., Rui, Y., Liu, B., Yuan, M., and Fu, Y.** (2013). MAP18 regulates the direction of pollen tube growth in Arabidopsis by modulating F-actin organization. *The Plant Cell* **25**, 851-867.
- Zipfel, C.** (2014). Plant pattern-recognition receptors. *Trends Immunol* **35**, 345-351.
- Zipfel, C., Kunze, G., Chinchilla, D., Caniard, A., Jones, J.D., Boller, T., and Felix, G.** (2006). Perception of the bacterial PAMP EF-Tu by the receptor EFR restricts *Agrobacterium*-mediated transformation. *Cell* **125**, 749-760.

Chapter 6 Appendix

Gene ontology (GO) enrichment analysis of RNASeq data uncover biological processes affected by myosin XI TS allele

To get insights into what molecular pathways are affected by the lack of functional myosin XI, we performed RNASeq on control and myoXIaTS plants exposed at 32°C for 2 hours (See Methods). Our attention focused on genes differentially expressed in the myoXIaTS plants exposed to 32°C versus the myoXIaTS plants kept at 20°C. A high number of differentially expressed transcript (DETs) were observed in the myoXIaTS exposed at 32°C compared to 20°C. To identify a potential functional profile among the detected DETs, we performed a Gene Ontology (GO) enrichment analysis. In a GO enrichment analysis, first genes with DETs are categorized and assigned to a GO term (biological process, molecular function, and cellular component). Then, a statistical analysis identifies which GO terms are enriched, with the goal of identifying the underlying biological changes. The GO enrichment analysis for the myoXIaTS exposed at 32°C reported, among the biological function, mainly transcripts related to the cytoskeleton (microtubules, GO:0005874; structural constituent of the cytoskeleton, GO:0005200), cell wall (e.g. cell wall, GO:0005618; cellular glucan metabolic process, GO:0006073; xyloglucan:xyloglucosyl transferase activity, GO:0016762), small GTPases (Ran GTPase binding, GO:0008636). For a more comprehensive list, see Table 6.1. These results suggest that the initial response to the loss of myosin XI function, at the transcription level, is to modulate the microtubule cytoskeleton and the cell wall architecture.

RNA Seq and Gene Ontology methods

P. patens protoplasts of a control and myoXIaTS line were regenerated for three days at 25°C in medium containing 10 mM CaCl₂ and 6% Mannitol. After regeneration, protoplasts were transferred in plates containing a growing medium and placed in a 20°C chamber for four days. Protoplasts were then transferred in a medium that stimulates caulonemata differentiation (PpNO3) and incubated at 20°C for four additional days. Regenerated plants were then incubated for 2 hours at 20°C and 32°C, then collected and flash-frozen in liquid N₂. This experiment was performed in triplicates. Total RNA was extracted via RNeasy Plant Mini Kit (Qiagen) and sequenced by the GENEWIZ facility. At GENEWIZ, libraries prepared with the NEBNext Ultra RNA Library Prep Kit (NEB) were sequenced on a HiSeq4000 sequencer. The sequencing generated 27-39 M read per sample. The fastq sequence quality was assessed with FastQC version 0.11.8 (<https://www.bioinformatics.babraham.ac.uk/projects/fastqc/>) and visualized using MultiQC version 1.9 (PMID: 27312411). The Illumina adapters and low-quality sequences were removed with Trimmomatic (Bolger et al., 2014), and subsequently the data were aligned to the *P. patens* genome V3.3 using HISAT2 (Pertea et al., 2016) with parameters: --max-intronlen 10000 --min-intronlen 100 -k 5 --no-discordant. The resulting SAM files were analyzed with htseq-count (PMID: 25260700) with parameters: -r name -t gene -m union --stranded=no, which provided read counts for each gene in each sample (Anders et al., 2015). The read counts were then analyzed with the R package DeSeq2 for differential gene expression analysis, pairwise samples being analyzed with three biological replicates each (Love et al., 2014). To identify GO terms overrepresented in each set of differentially expressed genes we applied the R package GoSeq version 1.40.0 (Young et al., 2010).

Table 6.1 List of GO terms enriched in the comparisons indicated. Only the GO terms with raw P value <0.012 were considered as significant.

Myosin X1a WT 20°C vs Myosin X1a WT 32°C

Biological process

photosynthesis	GO:0015979
oxidation-reduction process	GO:0055114
protein folding	GO:0006457
glycolytic process	GO:0006096
tetrapyrrole biosynthetic process	GO:0033014

Cellular component

photosystem II	GO:0009523
photosystem I	GO:0009522

Myosin X1a WT 32°C vs Myosin X1a TS 32°C

Biological process

cellular glucan metabolic process	GO:0006073
carbohydrate metabolic process	GO:0005975
glutamine metabolic process	GO:0006541
mitotic cell cycle	GO:0007067

Molecular function

catalytic activity	GO:0003824
hydrolase activity, hydrolyzing O-glycosyl compounds	GO:0004553
xyloglucan:xyloglucosyl transferase activity	GO:0016762
structural constituent of cytoskeleton	GO:0005200
Ran GTPase binding	GO:0008536

Cellular component

microtubule	GO:0005874
spindle	GO:0005819
cell wall	GO:0005618
apoplast	GO:0048046

Myosin XIa TS 20°C vs Myosin XIa TS 32°C**Biological process**

protein folding	GO:0006457
microtubule-based movement	GO:0007018

Molecular function

chaperone binding	GO:0051087
microtubule motor activity	GO:0003777
microtubule binding	GO:0008017
oxidoreductase activity, acting on paired donors, with oxidation of a pair of donors resulting in the reduction of molecular oxygen to two molecules of water	GO:0016717

Cellular component

COPI vesicle coat	GO:0030126
-------------------	------------

Myosin XIa WT 20°C vs Myosin XIa TS 20°C**Cellular component**

extracellular region	GO:0005576
----------------------	------------